Deep learning architectures for automatic detection of viable myocardiac segments

Khawla Brahim

THÈSE DE DOCTORAT EN CO-TUTELLE

DE L'ÉTABLISSEMENT UNIVERSITÉ BOURGOGNE FRANCHE-COMTÉ

PRÉPARÉE À L'UNIVERSITÉ DE BOURGOGNE

ET DE L'ÉTABLISSEMENT ÈCOLE NATIONALE D'INGÉNIEURS DE SOUSSE

École doctorale n°37

Sciences Pour l'Ingénieur et Microtechniques

Doctorat d'Instrumentation et informatique de l'image (UBFC) et en Génie Electrique (ENISO)

par

KHAWLA BRAHIM

Deep learning architectures for automatic detection of viable myocardiac segments

Thèse présentée et soutenue à Sousse, le 14 décembre 2021

Composition du Jury :

DOUIK ALI	Professeur à Univ. de Sousse	Président
KHLIFA NAWRES	Professeur à Univ. de Tunis El Manar	Rapporteur
GARREAU MIREILLE	Professeur à Univ. de Rennes 1	Rapporteur
AINOUZ SAMIA	Professeur à l'INSA Rouen Normandie	Examinateur
SAKLY ANIS	Professeur à Univ. de Monastir	Co-directeur de thèse
MERIAUDEAU FABRICE	Professeur à Univ. de Bourgogne Franche-Comté	Co-directeur de thèse
BOUCHER ARNAUD	Maître de Conférences à Univ. de Bourgogne Franche-Comté	Encadrant de thèse

N° | X | X | X |

ACKNOWLEDGEMENTS

"No man is an island entire of itself; every man is a piece of the continent, a part of the main."

—John Donne

Foremost, I owe sincere gratitude to my supervisors Dr. Arnaud Boucher, Prof. Anis Sakly, and Prof. Fabrice Meriaudeau, for their motivation, continuous support, and immense knowledge of my thesis. Their guidance, constant encouragement, and enthusiastic nature enriched this dissertation as it is today. I am profoundly grateful to Prof. Fabrice Meriaudeau for his insightful comments, deep vision, and countless hours spent critiquing and reviewing this project. Thank you very much.

A special thanks to Dr. Alain Lalande for his mentorship and help regarding various medical facets and to Dr. Ibrahima Faye for his expertise and valuable suggestions in all our discussions throughout my time at the UTP university in Malaysia.

My faithful appreciation goes to my thesis jury members Prof. Ali Douik, Prof. Nawres Khlifa, Prof. Mireille Garreau, and Prof. Samia Ainouz to spend their precious time reading and providing feedback on my thesis. It has been a magnificent honor for me to have such an excellent committee.

I would also like to thank Abdul Qayyum, who provided constructive remarks that greatly assisted the thesis, and all my labmates for their fond memories and kind supports.

Last but not least, I am very thankful to my beloved family for their everlasting emotional encouragement, confidence, as well as occasional inspirational thoughts: my mother, father's soul, sister, brother, and husband. Thank you all for always believing in me. This thesis is dedicated to the soul of my father.

Le Creusot, 01 July 2021 Khawla BRAHIM

Contents

I

Context and Problems

1

INTRODUCTION

This chapter explains the clinical motivation and thesis objectives for automatically segmenting the myocardial muscle, including Acute Myocardial Infarction (AMI), to help diagnosis and therapy planning. Also, it introduces the thesis outline and the significant publications ensuring from the thesis as a clue of its scientific quality.

1.1/ CLINICAL BACKGROUND

Cardiovascular Diseases (CVDs) are the leading causes of mortality worldwide, with an estimated 17.9 million deaths in 2019, mainly due to myocardial infarction (MI), commonly known as heart attack and stroke[1]. Radiologically diagnosing MI in its early phases plays a crucial role in treating and improving clinical outcomes. In recent decades, significant research works have been developed to improve the prognosis of cardiac diseases and therefore reduce CVDs deaths.

MI is a medical condition preventing blood supply to the cardiac muscle, caused by the blocking of coronary arteries (see Figure 1.1). The size of infarcted myocardial tissue is impacted by the time taken until treatment is performed. Acute complications may progress towards Heart Failure (HF) if the affected heart cannot pump blood sufficiently to the circulatory system's lungs and body [27].

MI occurs as a result of atherosclerosis, in which plaque builds up inside the artery walls. This build-up makes the arteries progressively narrower and slows blood flow, causing angina. Finally, an area of cholesterol plaque can tear inside of a coronary artery. This rupture results in a blood clot forming on the plaque's surface, which can then completely block blood flow through arteries. If the blockage isn't remedied fast, the heart muscle begins to die. The healthy heart area is substituted with the infarct area.

Medical studies have shown that in AMI, the infarct tissue mainly contains heterogeneous

[1] Source: https://www.who.int/news-room/fact-sheets/detail/cardiovascular-diseases-(cvds)
[2] Source: http://simple.wikipedia.org/wiki/Myocardial_infarction

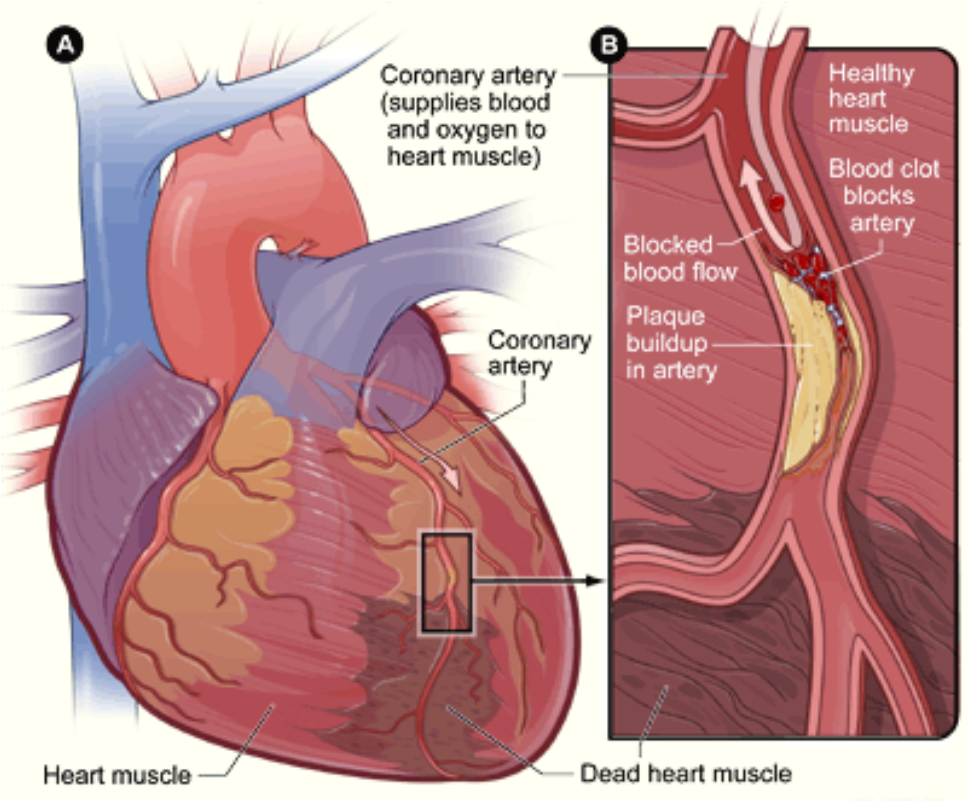

Figure 1.1: Illustration of how a blocked coronary artery leads to MI. The artery inhibits blood flow to the muscle, causing damage to the muscle tissue.[2]

regions. The chronic setting develops immediately after MI, and the aim of treatment is the fast recovery of blood flow. There is a lack of a viable myocardium (MYO) with the increased extracellular area. In chronic myocardial infarctions, capillaries in myocardial tissue continue to be impeded after the reperfusion, and a gray zone called peri-infarct exhibits decreased contractile activity. The permanent absence of tissue perfusion is known as microvascular obstruction (MVO), also called the no-reflow phenomenon [30]. Subjects sustaining MVO zones have higher proportions of MI and raised mortality [25]. There is a potent correlation between the peri-infarct region, ventricular arrhythmias, and unexpected death [45, 19]. Coronary revascularization for curing AMI is related with MVO in the scar core and peri-infarct area at the border of infarcts.

Late gadolinium enhancement (LGE) magnetic resonance imaging (MRI) is the reference standard for detecting MI [7, 11]. Myocardial LGE-MRI studies are achieved approximately 10 minutes following injection of the gadolinium-based contrast agent. With this method, healthy and infarct tissues are distinguished by their altered wash-in and wash-out contrast agent. By the automatic extraction of the geometry of the MYO, cardiologists can conclude the functionality of the damaged muscle, which supplies guidance on further treatment of the patient. As shown in Figure 1.2, the MVO area is defined as the hypointense region within the core of the MI on LGE-MRI sequences achieved at 3 min-

utes or 10 minutes following gadolinium injection.

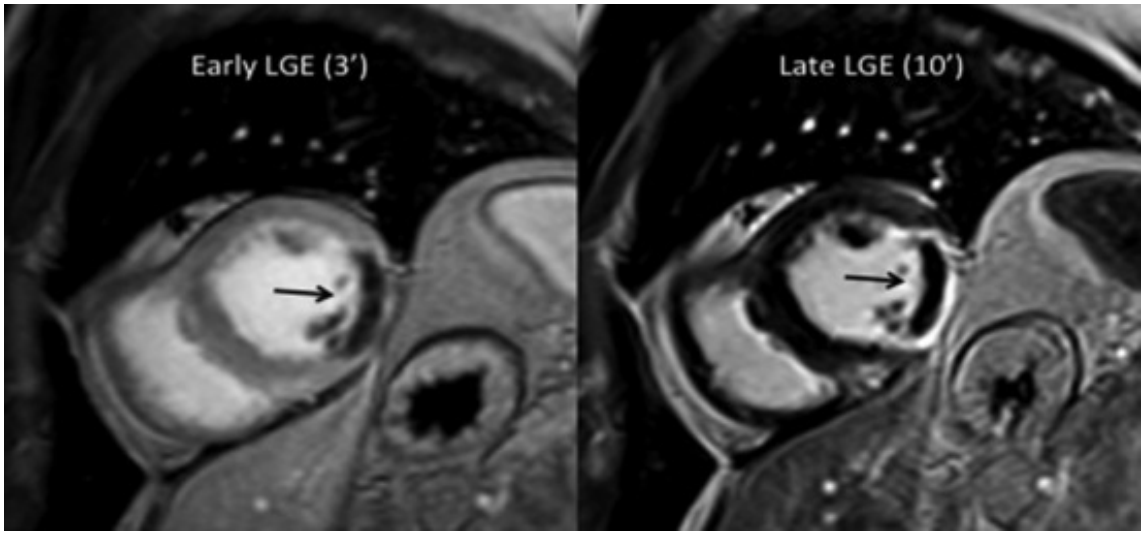

Figure 1.2: Short-axis view of early and late cardiac LGE-MRI in a subject with AMI. The MI occurs hyperintense on the late LGE image, with a subendocardial region (black arrow) corresponding to MVO. On the early LGE sequence, the MYO is still saturated with gadolinium, although the MVO already occurs hypointense (black arrow) [56].

Today, the accurate segmentation of the MYO is of high relevance in clinical practice. Clinicians achieve manual contouring of the MYO as an essential first step in analyzing cardiac images. An example of a delineation of a patient's slice can be seen in Figure 1.3. Nevertheless, as the workflow that clinicians face, manual segmentation is usually time-consuming, depends on expert experience, and suffers from expert variability. Consequently, there is an increasing need for automated segmentation methods. This requirement was primarily justified through the success rate performed by these methods [71].

1.2/ GOALS AND ORIGINAL CONTRIBUTIONS

Cardiac MR (CMR) imaging is of the greatest interest for morphological evaluation and diagnosis of different CVDs. Deep learning (DL) networks have significantly boosted state-of-the-art segmentation performance in Cardiac MRI (CMRI). Nevertheless, previous techniques have mainly applied various pre-processing stages to segment low-resolutions images. This thesis aims to develop a DL model using prior constraints performing automatic segmentation of the MYO of patients affected by diseased myocardial tissue (MI, MVO). Specifically, we proposed three end-to-end models (SegU-Net, SPIU-Net, ICPIU-Net) for myocardial segmentation in CMRI. Research on cardiac segmentation has been extensively promoted through benchmarking datasets, notably those associated with MICCAI challenges. We evaluated these approaches' performance on the EMIDEC

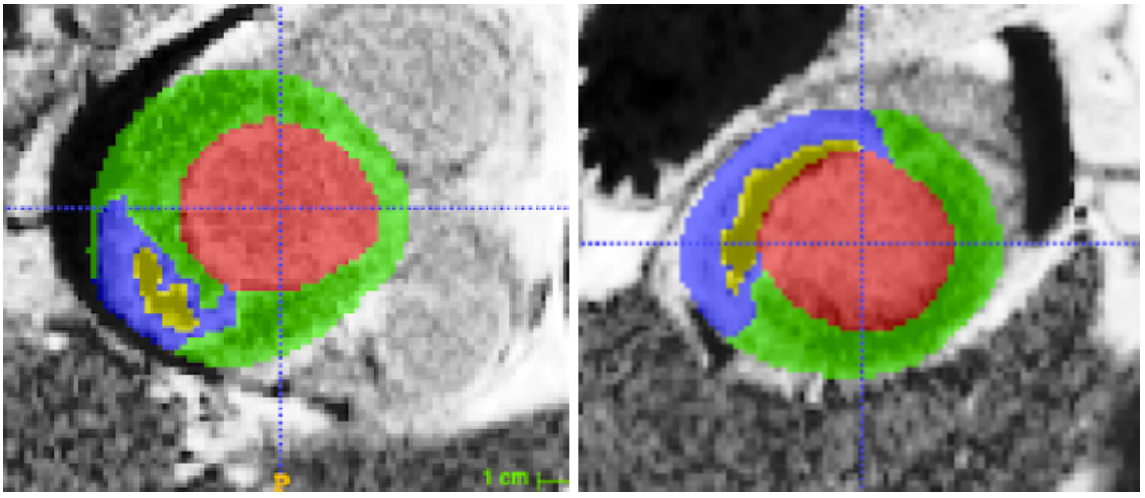

Figure 1.3: Short-axis LGE-MR images show left ventricular cavity (red), healthy MYO (green), myocardial scarring (blue), and MVO (yellow). The slices were extracted and cropped from the EMIDEC dataset (see section 4.4.5).

dataset to conclude which is well adapted to this task. Therefore, the goal is to build an automated system that produces a delineation of the myocardial regions shown as drawn boundaries over the LGE-MRI, presented in Figure 1.3. Different metrics evaluate the model's performance for finding the best-performing model by comparing the predicted results with the manual delineations. Experimental results highlight the efficiency of the proposed models compared to ground truth and state-of-the-art segmentation algorithms. Resources on the NVIDIA Tesla V100 with four embedded GPUs were available to fulfill the computational demands.

1.3/ Thesis Organization

In response to the HF problem described above, this thesis is composed of seven chapters. In the second one, we give an overview of the clinical context, where we present the anatomy and the functioning of the heart. Chapter 3 describes some fundamental concepts within the field of DL. In Chapter 4, we comprehensively provide a brief review of existing methods dedicated to medical segmentation tasks. We then describe the data material given by the EMIDEC challenge. Chapter 5 details the three general frameworks underlying the prior constraints based on inclusion and classification coupled with regularization penalty terms and the fusion of SegNet and U-Net architectures to segment all myocardial diseases in LGE-MR images. According to several metrics, Chapter 6 focuses on evaluating the performance of proposed algorithms (slice-by-slice 2.5D, a 3D-to-3D, and constrained with inclusion and classification 3D-to-3D). Chapter 7 summarizes the work and outlines some future directions for further improvement in the field.

1.4/ Publications Ensuing from the Thesis

The Ph.D. research led to 3 journal papers (1 accepted, 1 subject to major revisions, and 1 submitted), 2 conference papers, and 1 workshop paper.

1.4.1/ Journal Articles

- **Brahim, K.**, Qayyum, A., Lalande, A., Boucher, A., Sakly, A., and Meriaudeau, F.: A 3D Network Based Shape Prior for Automatic Myocardial Disease Segmentation in Delayed-Enhancement MRI. IRBM. (2021) [211]. - **1st Author**.

- Lalande, A. et al.: Deep learning methods for automatic segmentation of delayed enhancement-MRI. The results of the EMIDEC challenge. Medical Image Analysis. - **Contributing**.

- **Brahim, K.**, Arega T.W, Boucher, A., Bricq, S., Sakly, A., and Meriaudeau, F.: An Improved 3D Deep Learning-Based Segmentation of Left Ventricular Myocardial Diseases from Delayed-Enhancement MRI with Inclusion and Classification Priors Information U-Net (ICPIU-Net). Computer Methods and Programs in Biomedicine. - **1st Author**.

1.4.2/ Conference Proceedings

- **Brahim, K.**, Qayyum, A., Lalande, A., Boucher, A., Sakly, A., and Meriaudeau, F.: A 3D deep learning approach based on Shape Prior for automatic segmentation of myocardial diseases. In 2020 Tenth International Conference on Image Processing Theory, Tools and Applications (IPTA) (pp. 1–6). IEEE. (2020, November) [191]. - **1st Author**.

- **Brahim, K.**, Qayyum, A., Lalande, A., Boucher, A., Sakly, A., and Meriaudeau, F.: A deep learning approach for the segmentation of myocardial diseases. In 2020 25th International Conference on Pattern Recognition (ICPR) (pp. 4544–4551). IEEE. (2021, January) [212]. - **1st Author**.

1.4.3/ International Workshops

- **Brahim, K.**, Qayyum, A., Lalande, A., Boucher, A., Sakly, A., and Meriaudeau, F.: Efficient 3D deep learning for myocardial diseases segmentation. In International Workshop on Statistical Atlases and Computational Models of the Heart (pp. 359–368). Springer, Cham. (2020, October) [192]. - **1st Author**.

1.5/ CONCLUSION

Medical imaging is currently a research field in active expansion. Many studies are used nowadays to put in evidence infarction tissues and lesions attributed to other diseases such as hypertrophic cardiomyopathy. This thesis contributes to enhancing the diagnosis and monitoring of MI on LGE data, leading to better prevention and higher survival opportunities for the patient. Over the past few decades, DL is rapidly growing in image analysis, particularly CMRI segmentation. Designing a deep neuronal network is exciting guidance for our research. The primary objective is to develop new DL tools to assess risk, quantify and predict myocardial tissues' presence on a set of contrast-enhanced acquisitions.

2

Clinical Context

The cardiovascular system plays a significant role in the functioning of living organisms. In this chapter, we briefly describe the heart anatomy and its function. Then, we outline the most used imaging modalities for diagnosing and monitoring different cardiac conditions. In particular, MI can be identified at early phases by radiologists from CMRI. However, infarct region segmentations depend on intra- and inter-observer variability, which is critical to determining suitable therapy. Consequently, a computer-aided method should be carried out to detect scars, affording clinicians more consistency.

2.1/ Healthy Cardiac Structure and Function

2.1.1/ Cardiac Structure

A detailed review of the cardiac structure is provided in [15]. The heart is a muscular organ responsible for pumping oxygen-rich blood throughout the body. It is geometrically located at the chest's center between the right and left lungs.

The heart comprises two sides, split into two parts: two atria (upper chambers) and two ventricles (lower chambers), as illustrated in Figure 2.1. The atria are connected to veins and proceed as reservoirs for venous blood transits, with a pumping function for assisting ventricular filling. The ventricles are connected to arteries and primary pumping chambers that distribute blood to the systemic circulatory (left ventricle (LV)) and pulmonary circulations (right ventricle (RV)). The septum separates the two sides of the heart.

The heart wall consists of three layers: the epicardium, the MYO, whose thickness values vary between 6 and 16 mm, and the endocardium. The epicardium is the outer layer that helps lubricate and preserve the outside of the heart. The MYO is the muscular layer of the heart and comprises cardiac muscle tissue responsible for the blood pumping through the organism. The endocardium is the innermost layer that protects the blood from sticking inside the heart.

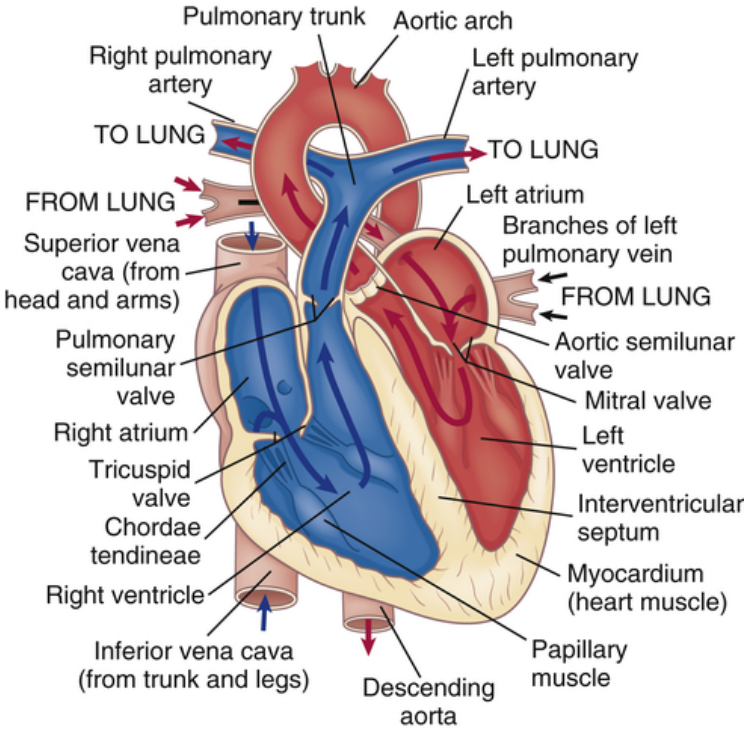

Figure 2.1: Anatomy of the heart.[1]

2.1.2/ Cardiac Cycle

The heart is a muscular pumping organ, reiterating the same cardiac cycle. Its frequency is usually expressed in beats per minute. Each cardiac cycle is split into two primary periods: diastole (relaxation), when the heart fills with blood, and systole (contraction), when the heart pumps the blood. These two periods depict a sequence of all the events that occur with every heartbeat. An electrocardiogram (ECG) detects the electrical impulses in the heart using electrodes attached to the skin. The graph of electrical activity through the heart includes three main waves: P, which represents depolarization of the atria; QRS complex, which represents depolarization of the ventricles; and T, which represents repolarization of the ventricles [60]. ECG is a standard test used to diagnose heart rhythms and electrical activity. Modifications in the typical ECG graph appear in several cardiac abnormalities, such as insufficient coronary arteries blood flow and cardiac rhythm troubles. Figure 2.2 shows the relationship between the cardiac cycle and ECG.

A great physician's interest has been dedicated to computing the LV mass and volume at the most significant contraction's time (end-systole) and the utmost filling's time (end-diastole) (see Figure 2.3).

[1] Source: https://basicmedicalkey.com/structure-and-function-of-the-cardiovascular-and-lymphatic-systems
[2] Source: https://www.reddit.com/r/Mcat/comments/i2r06k/the_cardiac_cycle_ecg_and_all

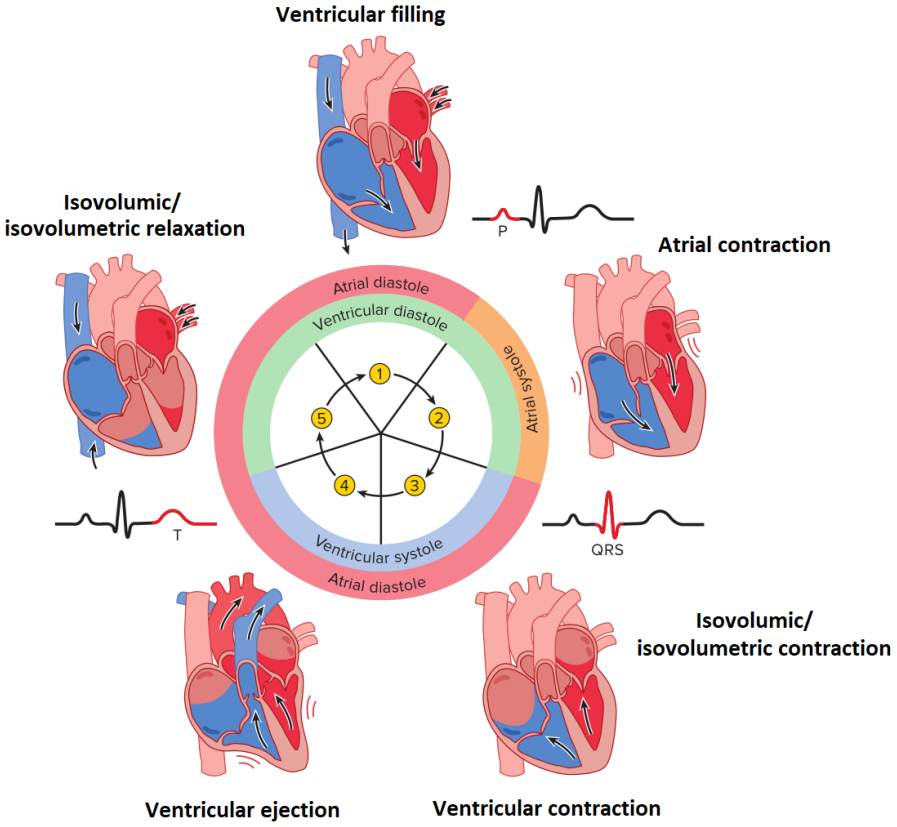

Figure 2.2: Overview of the cardiac cycle showing all phases and relative mechanical changes. Relationship to the ECG is revealed as color red in black segments.[2]

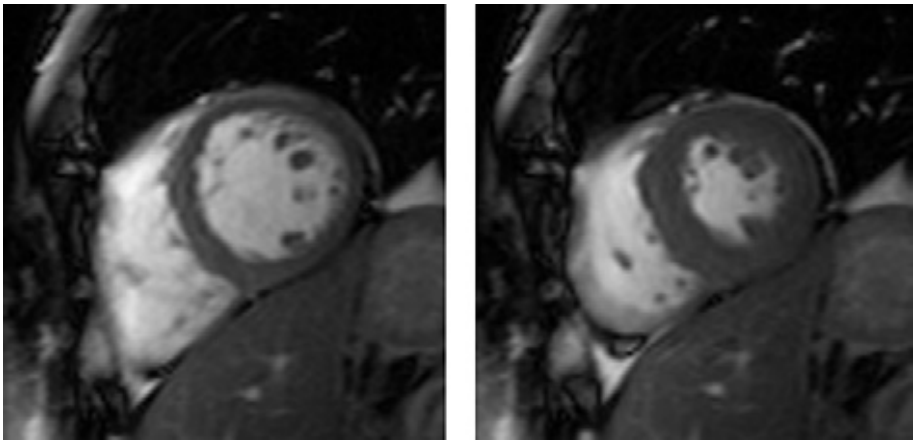

Figure 2.3: CMRI at end-diastole (left) and end-systole (right) [38].

2.1.2.1/ DIASTOLE

During diastole, the atria contract and propel the blood into the relaxed ventricles through the open atrioventricular valves. More specifically, the diastole comprises three sub-phases:

1. **Isovolumic relaxation**: The ventricles relax, with a rapid decrease in ventricular pressure. Both the aortic and the semilunar valves are closed over this sub-phase.
2. **Passive ventricular filling**: When left ventricular pressure drops below atrial pressure, the atrioventricular valves are open, and the semilunar valves keep closed. This sub-phase accounts for most of the ventricular filling with blood.
3. **Ventricular diastole or atrial systole**: The atria contract and then complete the ventricular filling.

2.1.2.2/ Systole

The Systole period pushes the blood from the ventricles to the pulmonary and systemic circulations. This period is divided into two stages:

1. **Isovolumic contraction**: As the ventricle starts to contract, the pressure surpasses that of the respective atrium, causing the atrioventricular valves to shut. Again, all the valves are closed, preventing blood from being ejected.
2. **Ventricular ejection**: When ventricular pressure overtakes that of the aorta and pulmonary arteries, the semilunar valves open. The LV and RV eject the blood to the aorta and pulmonary arteries, whereas the atrioventricular valves remain closed. And the cycle keeps repeating until the individual is dead.

2.2/ Cardiac Imaging Modalities

In terms of follow-up, treatment monitoring, and diagnosis purposes, several non-invasive imaging modalities have been made to provide clinicians a vision of the patient's medical condition. We introduce the three common imaging modalities utilized in cardiology, concentrating on MRI, the primary modality used in this thesis [32, 204]. Every technique is based on various image acquisition principles.

2.2.1/ Magnetic Resonance Imaging

Magnetic resonance imaging (MRI) is a comparatively recent imaging modality developed in the '70s. This technology is based on spin's physical quantum mechanical property. MRI is the favored modality for the guidance of cardiac interventions thanks to its multiple advantages, including high-quality, soft tissue contrast, and non-invasive aspects. Its use in cardiology is of greater focus through the last decades for disease segmentation and

treatment planning, and therefore the requirement for fast and accurate segmentation methods for identifying the diseased region is critical.

This technique depends on powerful magnetic fields, field gradients, and radio waves to acquire images into the body. Indeed, a uniform magnetic field (most of the utilized clinics' scanners perform at 1.5 or 3 Teslas) aligns the hydrogen atoms's spin. Then, a further magnetic field is superimposed to re-orient the aligned spins. The time that the spins takes to realign with the magnetic field relies on the environment and the molecules' chemical nature, which permits the scanner to reconstruct an image presenting various contrasts on the biological structures.

Through CMR imaging, it is possible to characterize myocardial tissues. T1 and T2 mapping sequences techniques have been progressively incorporated into CMR imaging settings, yielding accurate tissue characterization. Standardized cardiac T1 mapping is an MRI technique performed using balanced Steady-State Free Precession (bSSFP) sequences to compute a definite tissue's T1 (spin-lattice or longitudinal relaxation) time and visualize them voxel-vice on a parametric T1 map. It is a highly reproducible index that offers necessary measurements reflecting main myocardial properties [104]. T2 mapping mainly provides visualization and reliable quantification of myocardial edema and is thus a focus of several research tasks [29, 51]. It is more advantageous than other modalities in subjects with reduced LV function [104]. Similarly, T2 maps are acquired from a signal intensity versus time curve based on several spin-spin (transverse) relaxation times. Native T1, T2, and ExtraCellular Volume fraction (ECV) values, predictive parameters for diagnosis and treatment monitoring of cardiovascular diseases, are shown in Figure 2.4. Recently, several approaches used deep neural networks for CMRI segmentation (see section 4.3).

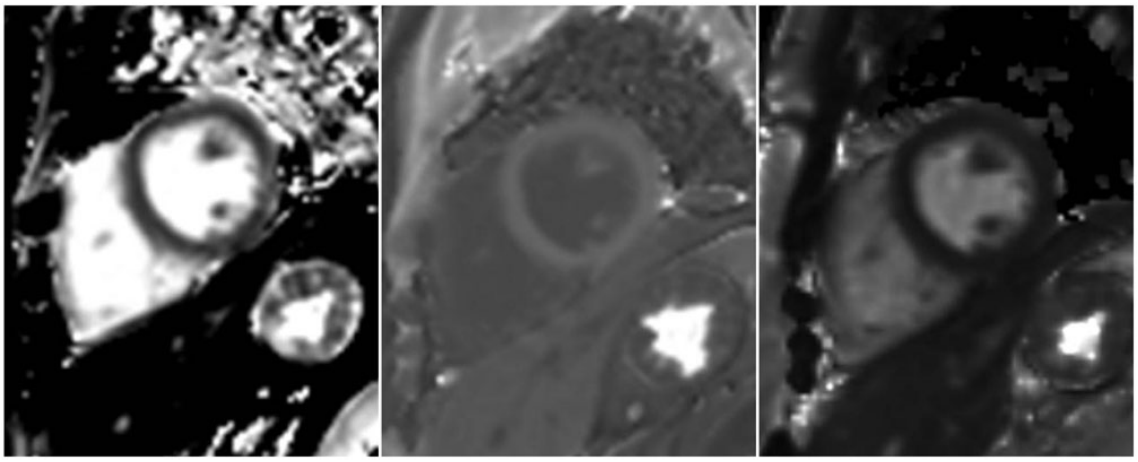

Figure 2.4: Short-axis images of native T1 (T1 time computed in the absence of a contrast agent), T2, and ECV maps of control subject [100].

2.2.1.1/ Cardiac Imaging Planes

Cardiac planes are typical views to visualize the heart on different cardiac imaging modalities such as MRI. These planes are oriented according to the long axis of the LV, the line that transects the LV apex, and the center of the mitral valve. Typical imaging axes pertinent to cardiac imaging are shown in Figure 2.5. In the following, we outline commonly used cardiac imaging planes which are not generally utilized for diagnostic goals other than for calibration goals:

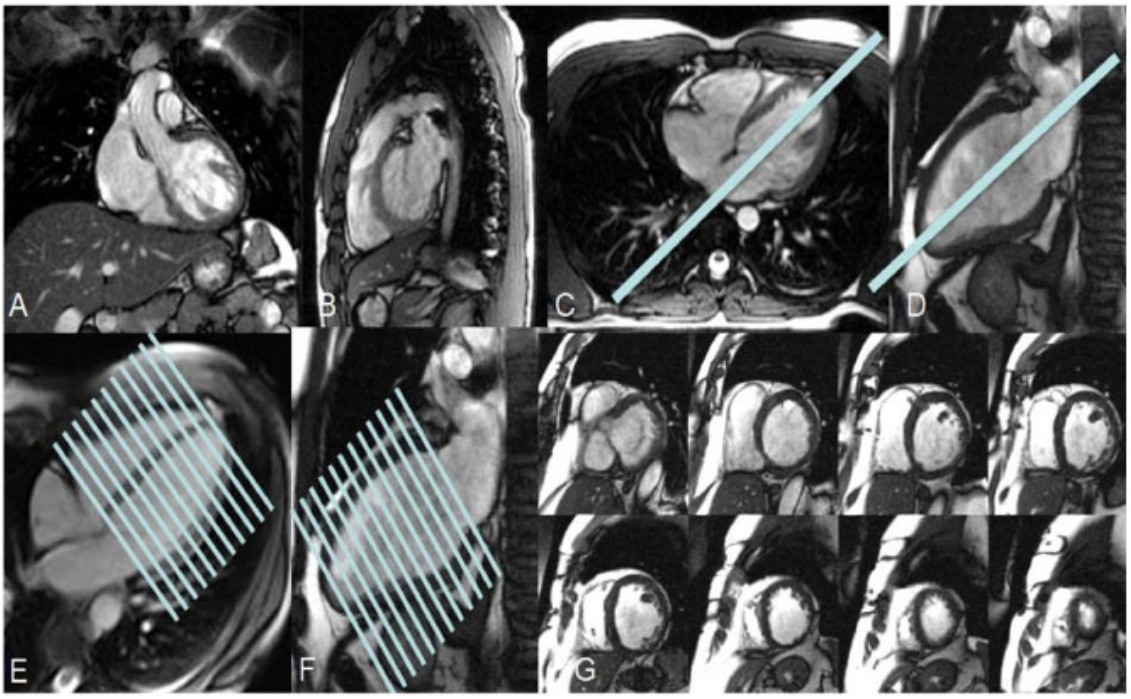

Figure 2.5: Cardiac axis imaging planes, depending on thorax planes, (A) Coronal, (B), Sagital, and (C) Axial. (D) Vertical long axis (VLA) localizer and Horizontal long axis planning (HLA). (E) HLA localizer and short-axis planning (SA). (F) VLA localizer and SA planning. (G) SA plane is prescribed perpendicular to both the VLA and HLA [34].

1. **Vertical long axis (two-chamber view (VLA))**

   The two-chamber view is aligned from the axial plane and passes through the center of the mitral valve and the LV apex. This view provides an overview of the LV and left atrium (LA).

2. **Horizontal long axis (four-chamber view (HLA))**

   Horizontal long axis aligned orthogonal to the VLA, passing through the center of the mitral valve and LA and continuing through the long axis of the LV. This view displays all four chambers of the heart, the left and right atria, and ventricles (LA, RA, LV, RV).

3. **Short axis (SA)**

   The short axis view yields excellent cross-sections of the LV and RV. This view is defined such that a series of slices are perpendicular to the two long axes (VLA, HLA) and often is utilized for viability analysis in MI.

2.2.1.2/ CARDIAC CINE IMAGING

An accurate evaluation of cardiac morphology and function is crucial for diagnosing cardiac diseases [10]. Dynamic image sequences (cine) are essential in obtaining complete heart function information throughout the cardiac cycle [63]. Indeed, cine CMRI is the fundamental method for quantifying the heart's global and regional contractile function [10, 9, 103]. As such, cine imaging is of primary significance to both clinical and research applications of CMRI. In typical cine scans, several 2D slices covering the whole volume of the heart are acquired (see Figure 2.6).

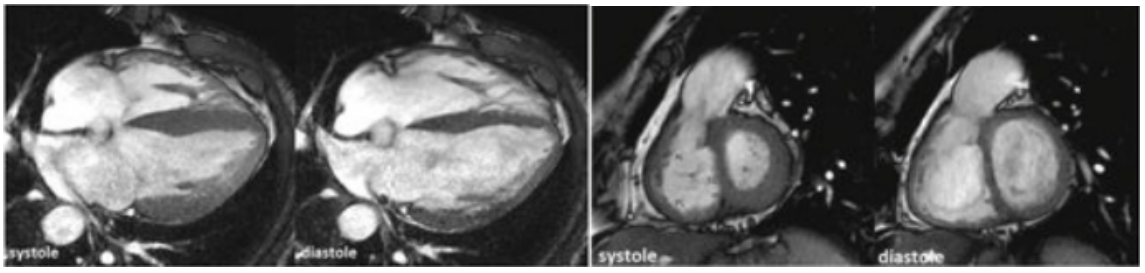

(a) (b)

Figure 2.6: CMRI. a) Cine MRI HLA. b) Cine MRI SA [73].

2.2.1.3/ MULTIPLE PROCEDURES OF LGE ACQUISITION

MRI technique is one of the best to visualize cardiac issues via several methods, such as Cine-CMR and, in particular, LGE acquisitions. LGE-MRI is usually performed after 10 minutes of gadolinium injection. Primarily, these acquisitions are an effective tool for image-guided prognosis and treatment planning. Its goal is to characterize myocardial infarct [18], which is the context for the thesis aiming to perform automatic segmentation of abnormal tissues within the LV, healthy MYO, and cavity. Image acquisition for LGE-MRI is often achieved with a T1 gradient echo and either Magnitude Inversion Recovery (MIR) or a Phase-Sensitive Inversion-Recovery (PSIR) (see Figure 2.7).

The constitution of a database is usually achieved using a single acquisition recovery technique. Indeed, while being effective at a given task, DL networks tend to depend on

[3]Source:http://mriquestions.com/ps-phase-sensitive-ir.html

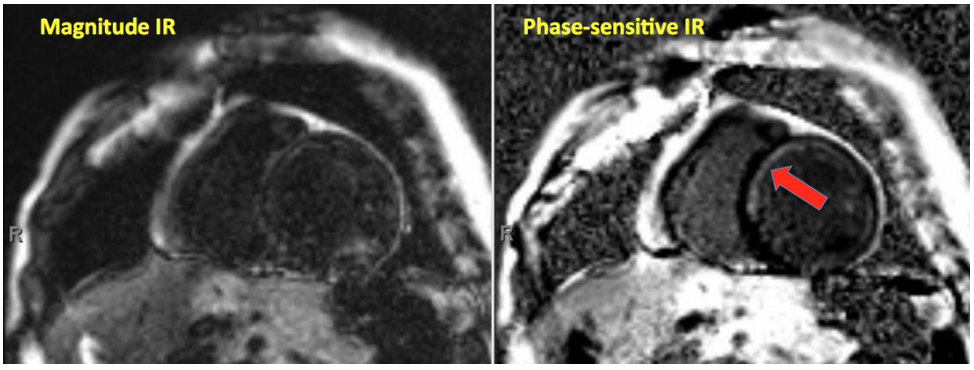

Figure 2.7: Example of an LGE-T1 slice in a patient with septal ischemia (arrow) using magnitude IR (left) against a second one using Phase-Sensitive IR (right).[3]

the provided data and fail because of differences among images when switching from one acquisition technique to another.

1. **Magnitude Inversion Recovery (MIR)**

   IR sequences usually use magnitude reconstruction for the translation of the MR signal to pixel intensity. In this approach, pixel intensity depends just on the magnitude of the longitudinal magnetization of a tissue. The performance of such a technique when employing magnitude reconstructed images is very sensitive to the inversion recovery time chosen.

2. **Phase Sensitive Inversion Recovery (PSIR)**

   Phase-Sensitive IR can eliminate the background phase while retaining the intended magnetization sign during IR [1, 3]. In PSIR, scar tissue has a higher signal than healthy MYO. Contrary to MIR, the PSIR method yields good results on a comparatively extensive range of inversion recovery time. The differences of signal among healthy and infarcted tissues may last longer.

2.2.2/ ECHOCARDIOGRAPHY

Echocardiography is nowadays extensively used for diagnostic tools in cardiology [2]. An echocardiogram (see Figure 2.8) is based on ultrasound in biological tissues. The main advantages of the Echo are its ease of use, low cost, safety (as it does not use ionizing radiation), and rapidity [4]. Due to the variance in the sound reflection, relying on the tissue, the ultrasound image can distinguish inner body structures from internal organs. During, echo acquisitions the clinician places the ultrasound probe utilizing a gel to promote the waves' transmission across the skin. In addition, ECG electrodes can be applied to gate the acquisition with the cardiac rhythm. Thus, several 2D temporal acquisitions are made in various positions, each taking from 10 to 30 minutes. A more recent method

enables real-time three-dimensional echocardiography where 3D acquisitions are made in one heartbeat. This method is of great significance in clinical practice to detect structural abnormalities [24, 26]. Several studies evaluated the potency of Myocardial Contrast Echocardiography (MCE) for myocardial viability assessment [12, 22, 28].

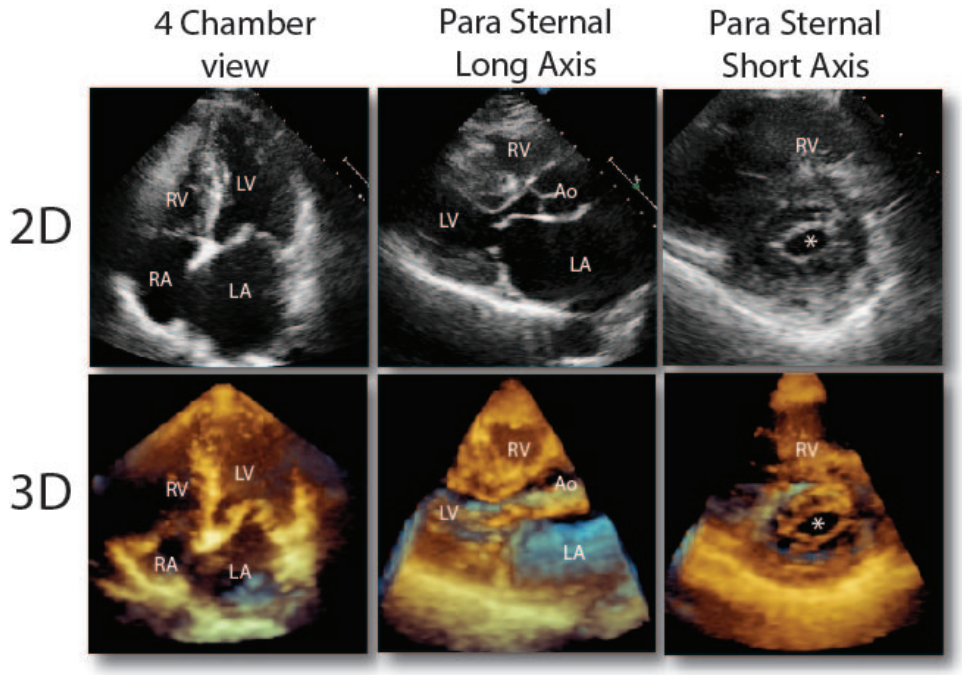

Figure 2.8: 2D and 3D echocardiography of the heart with the 3 most useful views [43].

For radiologists, echocardiography has been recognized as an efficient visualizing and diagnostic tool of LV due to its availability and low cost. However, echocardiography images suffer from specific artifacts (e.g., edge dropout, attenuation, and shadowing), preventing expert interpretation and automated computer analysis [42]. Therefore, automated LV segmentation of echocardiographic images has been a challenging task. Many advanced methods to echocardiographic segmentation data have been developed [174, 119, 105].

2.2.3/ Computed Tomography

As compared with MRI, Cardiac Computed Tomography (also called as CT scan, see Figure 2.9) does involve X-rays to acquire many images of the heart, and its acquisition takes less time. Furthermore, patients with medical implants may not be capable of incurring an MRI examination. Similar to cardiac motion from the MRI sequence, several temporal acquisitions of CT scans are obtained and ECG gated to reconstruct all the sequences.

The CT scan's principle is based on detecting the X-rays intensity, which passe across the anatomy to estimate the "material density" and thus acquire the image of the anatomy. Electrons are diffused onto a tinny surface, leading to the radiation's emission.

Several X-rays images are fused to generate cross-sectional views of the body. Before acquisitions, the patient can be injected with a contrast medium, a chemical substance that discloses internally in the body's tissues [14, 13].

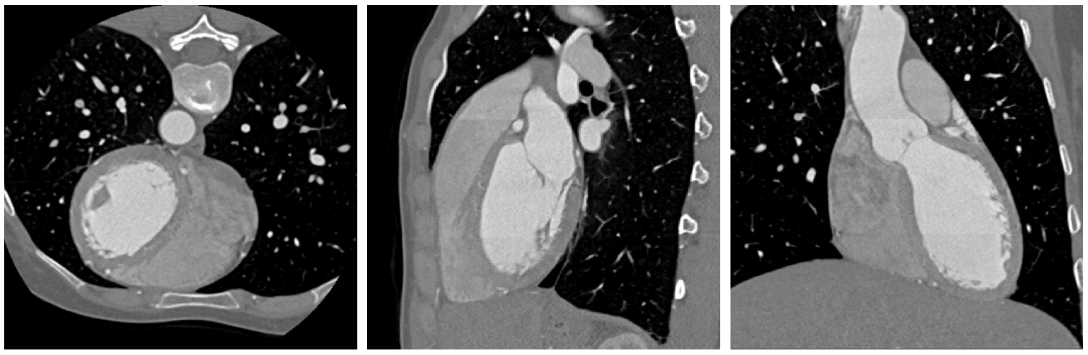

Figure 2.9: Three different views acquired using 3D CT image [109].

3D CT images are significant imaging modalities that provide detailed tissue information to assist diagnosis and planning treatment [21]. Nevertheless, anatomical segmentation based on CT images on a broad human body tissue is still challenging due to similarities of image appearance between several structures. Thus, many approaches focused on medical image segmentation from 3D CT images [89, 124, 112, 136, 185].

2.3/ CONCLUSION

According to the cardiac activity to visualize, several imaging modalities can be utilized to image the heart. For instance, infarcted tissues can be observed using MRI and gadolinium-contrast agents to help therapy planning. In the clinical diagnostic process, segmentation of the heart is essential to yielding quantitative measurements. Nevertheless, heart segmentation is a tedious and time-consuming task if drawn manually. DL-based networks are widely used due to their promising performance in diverse cardiac image segmentation challenges.

3

Background on DL

Deep learning is a subset of machine learning that iteratively updates to extract relevant features from data. These models were born out of deep artificial neural networks with several successive layers: input, output, and hidden layers, to imitate the functioning of the human brain. DL is highly advantageous to data scientists to process data and make decisions quickly. Recently, it has reached promising performance on different computer vision applications. Current advances in DL motivate us to develop deep-based approaches for myocardial disease segmentation. This chapter introduces the background knowledge of DL networks and the model training techniques. Finally, to quantitatively evaluate automated segmentation algorithms' performance, different evaluation metrics are presented.

3.1/ Medical Image Segmentation Based on DL

This section presents fundamental neural networks and building blocks that are often used to improve the potential of the network architectures in learning features that are helpful for image segmentation, being the thesis subject.

3.1.1/ Convolutional Neural Networks (CNNs)

Convolutional neural networks (CNNs) are well-known deep-based neural networks used for image analysis. They have reached great hits in the field and ancillary diagnosis. A typical CNN contains an input layer, a stack of functional layers, which usually include convolutional layers, pooling layers, and fully connected layers, and an output layer (see Figure 3.1). Mainly, each convolution applies a $n \times n$ kernel (case of 2D input) or $n \times n \times n$ kernel (case of 3D input). This operation is especially helpful in getting local patterns, i.e., visual elements in images. The convolved outputs are then passed per a batch normalization (BN) [58] followed by a nonlinear activation function to perform feature maps

extractions, which are later downsampled by pooling layers to capture an increasingly significant field of vision. Fully connected layers are then used to decrease features' dimensions and achieve high-level reasoning [40, 53, 58]. The final output is a fix-dimension vector which each element's form depends on the specific task (object localization, image classification, regression, patch-based segmentation, etc.). Through increasing depth (stacking many hidden layers), accuracy might be improved to a great extent or might not, depending on the complexity of the task.

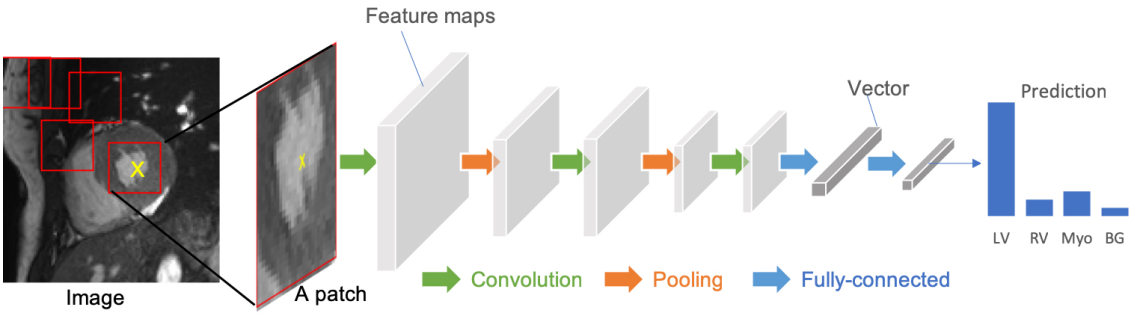

Figure 3.1: Architecture of a CNN. The network's input is a CMR image containing three building blocks: convolutional, pooling, and fully connected layers [195].

CNNs can be used for image segmentation tasks [89, 48, 79]. Nevertheless, this task needs to split every input image into patches and, after that, train a CNN to predict the class label of each patch's center pixel. A pixel-wise segmentation map is finally obtained for the entire image through forwarding patches at various positions into the CNN for classification. For reliable pixel-wise segmentation, a fully convolutional neural network (FCN) is more often employed.

3.1.2/ Fully Convolutional Neural Networks (FCNs)

FCNs are variants of CNNs that Long et al. [61] proposed for image segmentation. They are the pioneering networks of the most leading DL techniques for volumetric medical image segmentation [89, 95, 65]. For instance, Zhou et al. [89] segmented anatomical structures in 3D CT images by majority voting the segmentations of multiple 2D slices from an FCN, reaching promising results against experts annotations. FCNs have an encoder-decoder architecture. The encoder maps the input image into a high-level feature representation. Then, the decoder interprets these feature maps and retrieves spatial information for pixel-wise prediction. Compared with a patch-based CNN for segmentation, FCN is trained on the whole images, without patch choice's requirement. An example of FCN architecture for cardiac image segmentation is shown in Figure 3.2.

Many variants of FCNs have been introduced to enhance the segmentation accuracy. The U-Net [64], which will be discussed in the upcoming chapter, is the most widespread

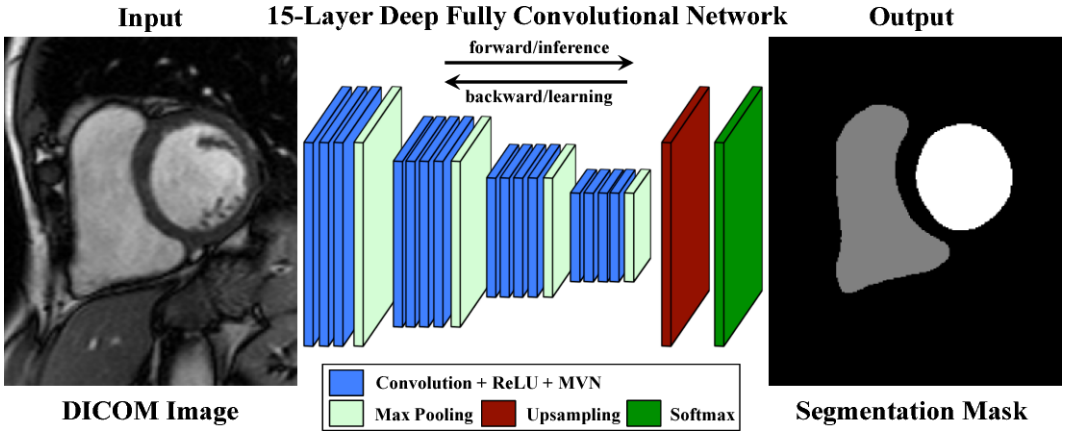

Figure 3.2: Architecture of fully convolutional neural networks (FCN) for image segmentation. Acronyms: ReLU – Rectified Linear Unit; MVN – Mean-Variance Normalization [86]

variant of FCNs for biomedical image segmentation. It uses skip connections amongst the up-sampling path and the down-sampling path to retrieve the spatial context loss, achieving accurate segmentation (see Figure 3.3).

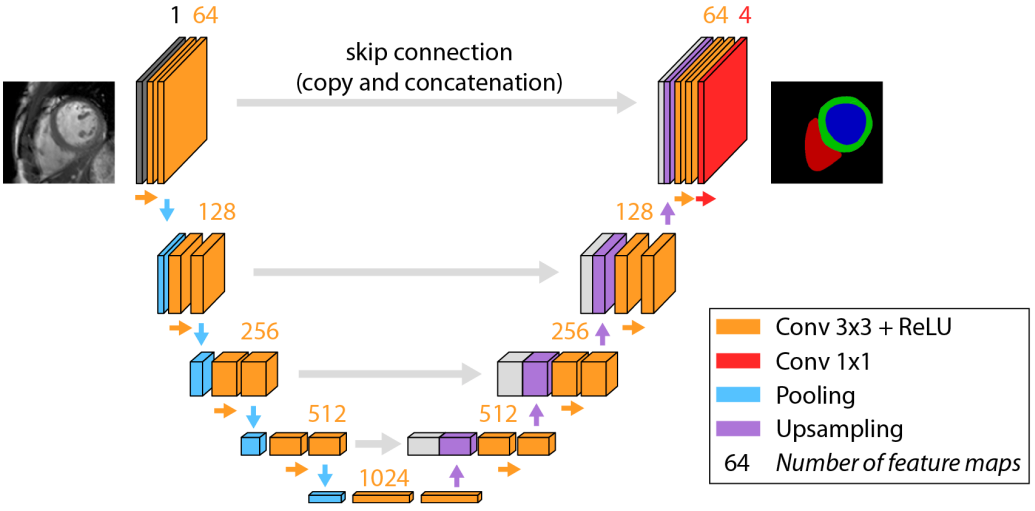

Figure 3.3: Overview of the U-Net network structure. The LV cavity is displayed in blue, the MYO in green, and the RV in red.[1]

The advance of U-Net has become a research hotspot in medical image segmentation. Various cardiac image segmentation works in the literature were based on the U-Net and its 3D variants (the 3D U-Net [70] and the 3D V-Net [78]), yielding outstanding segmentation accuracy for different cardiac segmentation applications [97, 146, 182]. Based on FCNs, Badrinarayanan et al. [90] proposed an encoder-decoder architecture, called

[1] Source: https://www.escardio.org/Education/Digital-Health-and-Cardiology/Virtual-Journal/how-to-read-this-cardiac-segmentation-with-ai

SegNet for image segmentation. Whereas SegNet passes max-pooling indices to the upsampling layers, FCN learns deconvolution filters to upsample (i.e., appending the relative feature map from the encoder phase) (see Figure 3.4). As detailed in chapter 5, the current work is based on 3D U-Net (SPIU-Net, ICPIU-Net) and a hybrid architecture of U-Net and SegNet, which takes the best of both models (SegU-Net).

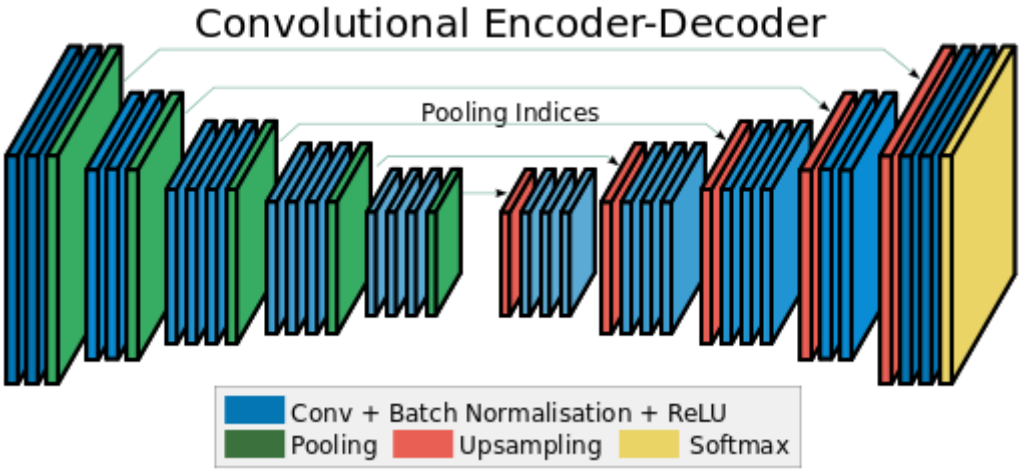

Figure 3.4: Overview of the SegNet architecture [90].

3.1.3/ Recurrent Neural Networks (RNNs)

Recurrent neural networks (RNNs) are artificial neural networks used for sequential data, such as ultrasound image sequences and cine MRI [183]. As shown in Figure 3.5 RNNs retain previous outputs and use their internal state to decide when processing the next inputs. The fusion of RNN and 2D FCN is widely used in cardiac segmentation to refine the inter-slice coherence of generated segmentation [83].

3.1.4/ Autoencoders (AEs)

Autoencoders (AEs) are unsupervised neural networks that aim to learn compact latent representations from input data. A classic autoencoder's architecture contains two main networks: an encoder network that compresses the input and produces the code and a decoder network to reconstruct the data back to the input dimension using this code (see Figure 3.6). As the learned representations include usually helpful information in the data, several researchers have used autoencoders to extract common semantic features and shape information from original data for cardiac image segmentation guidance [80, 142, 186]. Oktay et al. [80] developed a residual convolutional network-based model to reconstruct 3D volumes from the full stack of 2D images for better image analysis.

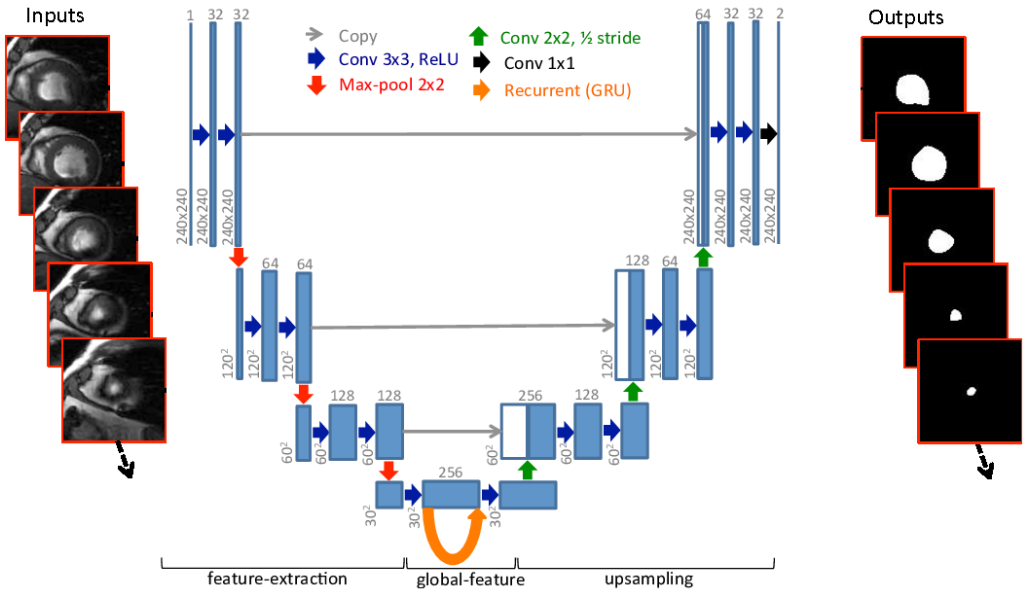

Figure 3.5: Overview of the RFCN network for cardiac image segmentation. The orange arrow represents a recurrent connection to manage inter-slice dependencies learned via GRU. The network aims to segment cardiac ventricles from 2D CMRI [83].

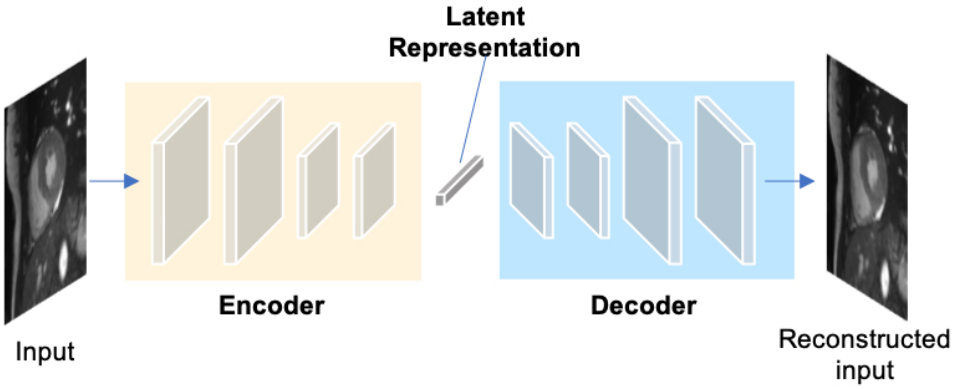

Figure 3.6: A typical structure of an autoencoder. An autoencoder uses an encoder-decoder framework, where the encoder maps the input into a lower-dimensional latent-space representation and then the decoder interprets this code to reconstruct the original data [195].

3.1.5/ GENERATIVE ADVERSARIAL NETWORKS (GANS)

Generative adversarial networks (GANs) are generative-based models proposed by Goodfellow et al. [46] to create new, synthetic images. GANs learn to generate from a training process through two adversarial networks contesting with each other: a generator network and a discriminator network (see Figure 3.7a). The generator aims to artificially create fake images across a random noise that it received, while the discriminator is used to determine whether an image is “real”. GANs are successfully applied to

segmentation tasks (see Figure 3.7b). A segmentation network substitutes the generator. The discriminator is needed to identify the generated segmentation maps from the gold standard ones [77, 141]. Lau et al. [139] proposed ScarGAN network to simulate scar region on healthy MYO and artificially augment the training sets using chained GAN. Training a U-Net with supplementary simulated scar tissue scans demonstrated more accurate segmentation on test images ("80.5%" vs. "75.9%").

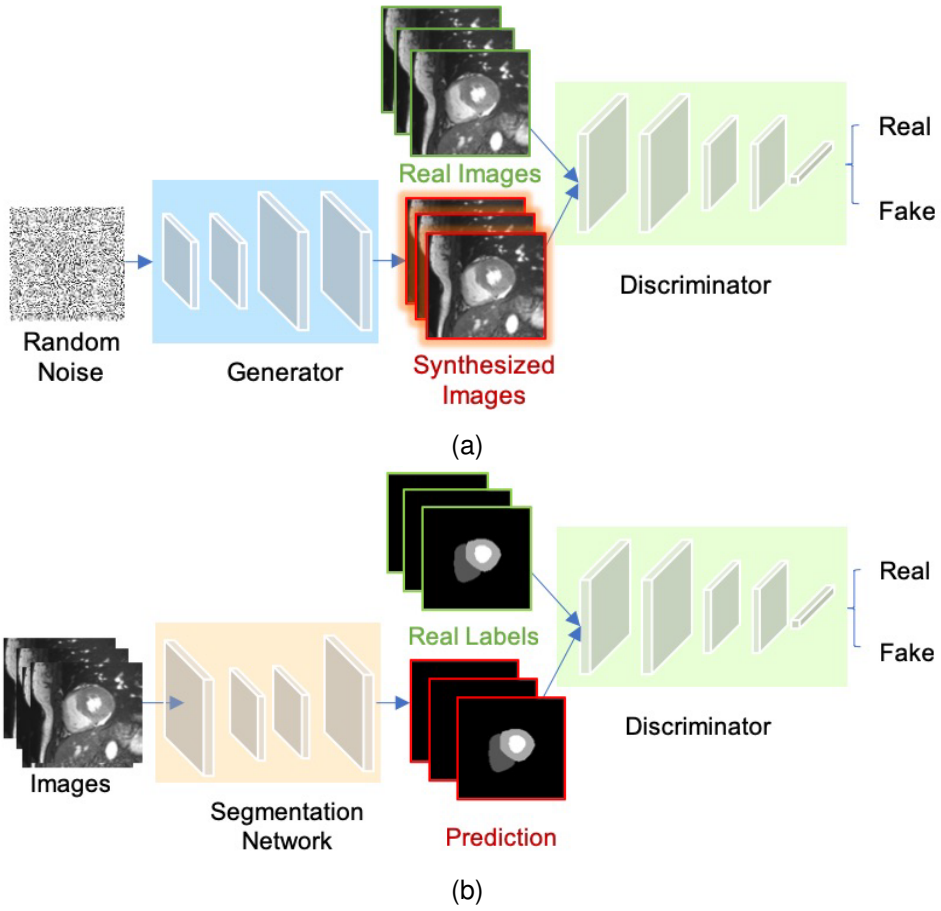

Figure 3.7: a) Chart of GANs framework for cardiac image synthesis. b) Schematic of adversarial training for cardiac image segmentation [195].

3.1.6/ Advanced Building Modules for Better Segmentation

Recently, several researchers have introduced advanced building modules to learn improved features for the accurate segmentation of images. These modules have been extensively used in previous neural networks to boost the performance of cardiac image segmentation. With this aim, we report in this section three different types of state-of-the art methods: a) advanced convolutional blocks for multiscale feature aggregation (e.g., deep supervision [59], inception modules [66], dilated convolutional kernels [67], atrous spatial pyramid pooling [92]); b) adaptive convolutional kernels to capture most relevant

features (e.g., attention units [113], squeeze-and-excitation blocks [138]); c) interlayer connections to recover previous features in the following layers (e.g., residual connections [72], dense connections [96]).

3.2/ TRAINING NEURAL NETWORKS

The training process is the most challenging step on DL methods due to the computational and configuration intricacy required for the execution. This process needs a dataset including paired images and ground truths, an optimizer, and a loss function. The model training aims to get the best network parameters to reduce the loss function.

3.2.1/ GRADIENT DESCENT OPTIMIZER

A deep network contains millions of parameters representing a mathematical solution to such a task. The trained network is adapted to the learning process beneath a specific parameter set by optimizing many network attributes. In particular, gradient descent is an optimization algorithm to reduce the loss function. Different gradient descent optimizers have been designed (e.g., Momentum SGD [8], AdaGrad [36], Adam [47]).

3.2.2/ LOSS FUNCTIONS IN DL

During the training process, we reduce the network error through a loss function, which assesses how well the learning algorithm fits the dataset. To that end, a suitable loss function is highly required to design and configure the network.

Given a series of of paired images and labels $\{(x_i, y_i) : i = 1, ..., N\}$, the network learns the mapping link of $x \rightarrow y$. Thus it predicts the output $(\hat{y})$ the closest possible to the ground truth (y). In the following, we report different loss functions frequently used for regression, image classification, and segmentation.

Mean Squared Error Loss (MSE), also recognized **L2 Loss** is the default loss function for regression tasks such as image reconstruction, heart localization. The MSE is defined as:

$$L_{MSE} = \frac{1}{N}\sum_{i=1}^{N}(y_i - \hat{y}_i)^2 \tag{3.1}$$

where y_i, $\hat{y}_i$ denote the vectors of the gold standard and predicted values, N represents the number of dataset samples.

Cross-entropy (CE) is the most used loss function for image classification and segmentation problems. In multi-class segmentation, and for every class, this loss resumes the pixel-wise probability errors between the actual gold standard map y and its relative predicted output p.

$$L_{CE} = -\frac{1}{N}\sum_{i=1}^{N}\sum_{c=1}^{C} y_i^c log(p_i^c) \tag{3.2}$$

where C represents the number of all categories.

Especially for image segmentation, several researchers used **soft-Dice loss function** [78], that penalizes the dissimilarity between the actual gold standard map and its corresponding predicted segmentation at pixel-level:

$$L_{Dice} = 1 - \frac{2\sum_{i=1}^{N}\sum_{c=1}^{C} y_i^c p_i^c}{\sum_{i=1}^{N}\sum_{c=1}^{C}(y_i^c + p_i^c)} \tag{3.3}$$

Moreover, different variants of the cross-entropy and soft-Dice loss functions (e.g., the **weighted cross-entropy loss** [98, 91] and **weighted soft-Dice loss** [117, 169]) are widely utilized to solve the class imbalance issues in medical image segmentation tasks in which the loss value is weighted to consider infrequent categories.

Several other DL networks use a **hybrid loss** that fused various loss functions (e.g., **focal loss** [160], soft-Dice loss, and weighted cross-entropy) to alleviate the class imbalance problem, and so to boost the segmentation performance [118, 185].

3.2.3/ REDUCE OVER-FITTING

Due to the limited training size datasets compared to the number of the learnable parameters in a deep model, over-fitting is the greatest challenge of training deep models (see Figure 3.8). Below, we review few methods overcoming this issue in the literature:

trained with limited size datasets

Weight initialization [33, 62, 57] is a crucial conception choice that aims to impede the outputs of layer activations from vanishing or exploding in the forward transfer process of DL networks.

Dropout [40, 54], a regularization method to avoid overfitting by randomly removing a fraction of nodes in DL networks over each training iteration, is amongst the widely used features for improving the network's performance.

Data augmentation [188, 194] is an effective technique used in model training, where it raises the number of input data by artificially generating training images through applying

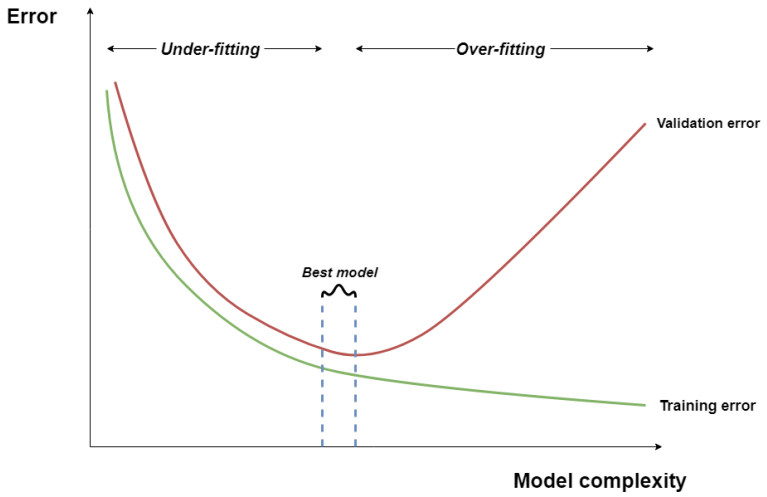

Figure 3.8: Illustration of over-fitting [171].

an ensemble of affine transformations to existing data.

Transfer learning is a deep network method that aims to reuse a model pre-trained on existing large datasets, using its knowledge gained for this task. The model can rapidly converge even with restricted data. Several works have proved the potential of transfer learning in improving the network generalization capacity for cardiac ventricle segmentation [161, 165, 169].

3.3/ EVALUATION METRICS

How to assess the efficiency of segmentation methods is a crucial issue. The validity of segmentation algorithms can be evaluated in many aspects, such as quantitative accuracy, inference time, and memory uses. Below we mainly outline the EMIDEC challenge's metrics[2] for measuring the performance of segmentation algorithms. Region-based metrics and volume-based metrics were computed for each test subject. After that, we measured their mean values to evaluate the performance of our myocardial disease segmentation. Frequently used comparison measures to evaluate automatic segmentation, such as volumetric Dice similarity coefficient or Hausdorff distance, have proven to be good geometric similarity evaluation metrics. In the present task, the volumetric difference metric for evaluating 3D myocardial segmentation is calculated to visualize the volume-wise performance of the approach. Though quantitative metrics are utilized to compare several methods on benchmarks (doctors' manual-contouring for medical segmentation), qualitative results are significant in concluding which technique is best.

1. **Dice similarity coefficient (DSC)** is a popular metric in validating medical image

[2]Source:https://github.com/EMIDEC-Challenge/Evaluation-metrics/.

segmentation (see Eq. 3.4). It is commonly used to compute the similarity between predicted and gold standard maps. Its value range is 0 (mismatch) to 1 (excellent match).

$$DSC = 2\frac{|P \cap G|}{|P| + |G|} \tag{3.4}$$

where P, G denote the predicted and gold standard maps, respectively.

2. **Hausdorff distance (HD)** [50] calculates the degree of similarity amongst two sets of points: the distance between the two delineations of the gold standard and the predicted segmentation. It is a complementary statistic to the DSC. The HD identifies segmentations with wide local differences, although they were well segmented. A lower value of HD mirrors a higher segmentation performance. The metric is determined as follows:

$$HD = (\max_{p_i \in P}(\min_{g_j \in G}(d(p_i, g_j))), \max_{g_i \in G}(\min_{p_j \in P}(d(p_i, g_j)))) \tag{3.5}$$

where $P = \{p_i : i = 1, ..., N_P\}$, $G = \left\{g_j : j = 1, ..., N_G\right\}$ denote the predicted and gold standard maps, respectively, d represents the distance between p_i and g_j.

3. **Absolute volume difference (AVD)** measures the difference average across a whole set of slices between predicted V_P and gold standard V_G LV volumes.

4. **Absolute volume difference rate according to the volume of the MYO (AVDR)** is computed as follows:

$$AVDR = \frac{AVD}{V_{MYO}} \tag{3.6}$$

where $AVD = |V_P - V_G|$ and V_{MYO} is the MYO volume of the gold standard annotation.

3.4/ CONCLUSION

DL has been the research boom and the development engine of the image area. This chapter summarizes different neural networks and several methods for model training. Then, a brief overview of evaluation metrics for image segmentation is provided. The next chapter presents a detailed literature review of the state-of-the-art medical image segmentation, including scar segmentation approaches and benchmarking CMRI datasets.

4

State-of-the-Art

This chapter reviews a summary of DL-based methods, highlighting their contributions to network design. Several recent studies based on DL have demonstrated excellent performances in segmenting particular tissues such as the LV, scars, and coronary vessels, aiding follow-up quantitative analysis of cardiovascular anatomy and function. Benchmarking datasets with assessment metrics are much required to compare new methods for MI segmentation with state-of-the-art. Thus, we conduct a brief coverage of popular datasets for the LV myocardial segmentation task.

4.1/ Medical Image Segmentation

Medical image segmentation, dividing an image into several predefined sets of organs or diseased bodies from medical imaging modalities, is one of the grand challenges, in medical image analysis to assist doctors in diagnosing and make decisions significantly. In the previous few years, many researchers have applied DL-based networks to medical image segmentation in the scar [151, 148, 177], pancreas [65, 134], atrial [127, 147], prostate [121], brain [50, 82, 94], lung [74], and multi-organ [124, 112]. Their automated segmentation accuracy has outperformed classical segmentation techniques, including thresholding [35], edge-based [23], and region-based methods [20].

4.2/ Commonly DL Architectures for Medical Image Segmentation

4.2.1/ 2D U-Net

Based on FCN architecture, Ronneberger et al. [64] proposed a U-Net network for biomedical image segmentation. This model comprises a U channel, composed of two paths of analysis (contracting) and synthesis (expansive), and skip-connections linking

the layers of the contracting path to their counterparts of the expansive one to provide them crucial high-resolution features. The network architecture uses two 3×3 convolutions followed by a ReLU activation function and a max-pooling operation to reduce the size of the latent image. The process is repeated until attaining a single features vector, useful to reconstruct an image with probability-wise classified pixels for accurate segmentation by incorporating transmitted outputs during the analysis path. The proposed network simultaneously fuses low-level feature maps, for better accuracy, with high-level feature maps, for complex features extraction. The U-Net architecture is shown in Figure 4.1.

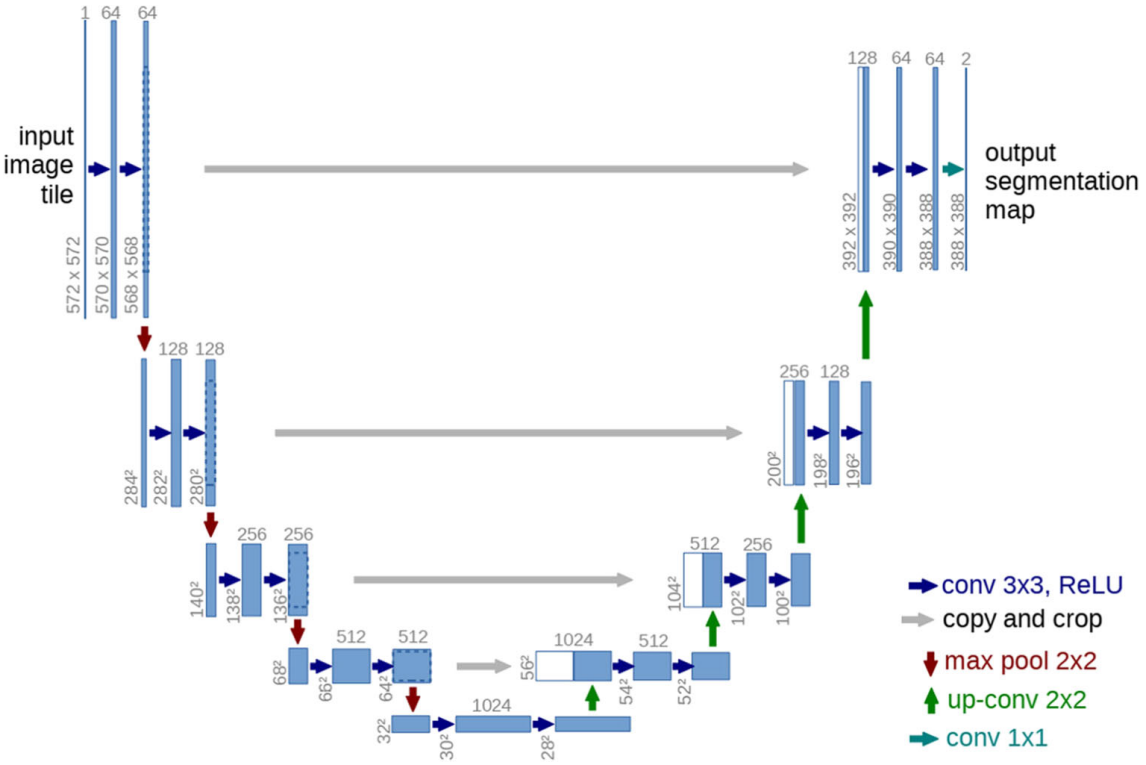

Figure 4.1: Original U-Net implementation. Skip-connections are represented by horizontal arrows [64].

Thanks to its outstanding performance, U-Net, and its variants (integrating novel modules and other concepts) have been extensively applied to many domains of computer vision [137, 91, 154, 125, 187]. For example, Gordienko et al. [137] employed a U-Net-based network for lung segmentation using X-ray scans. Their design achieved fast and accurate image segmentation. Farrag et al. [213] compared several automated frameworks for LV myocardial segmentation in native and contrast-enhanced T1-maps. The authors proved that U-Net architecture achieved better results than Dense Nets and Attention Nets, indicating the reliability of the U-Net-based method in clinical applications. Figures 4.2 and 4.3 show resultant myocardial segmentation of the U-Net-based architecture in native and contrast-enhanced T1-maps, respectively.

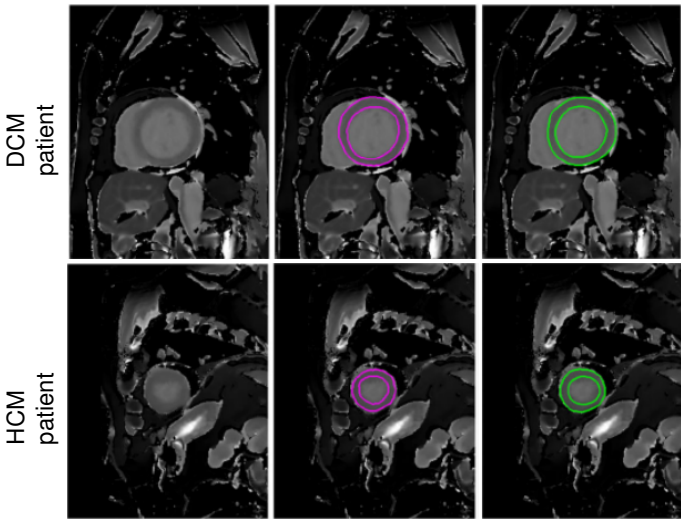

Figure 4.2: Myocardial contours in two example cases from DCM and HCM patient groups. Columns from left to right represent the original native T1-maps, Ground truth, and U-Net-based contours. [213].

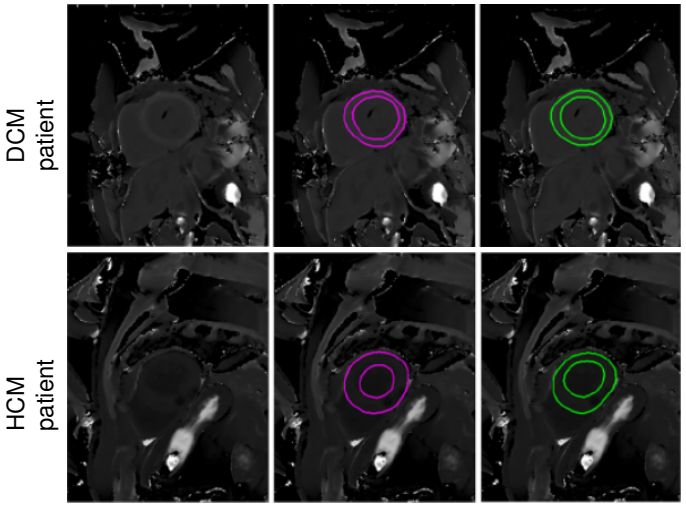

Figure 4.3: Myocardial contours in two example cases from DCM and HCM patient groups. Columns from left to right represent the contrast-enhanced T1-maps, Ground truth, and U-Net-based contours. [213].

4.2.2/ 2.5D Approaches

Several networks performing medical image segmentation are based on 2.5D approaches. These approaches reaped the benefits of 3D segmentation by integrating (partial) 3D information to improve segmentation, whereas sidestepping its high memory consumption challenges. One of the more frequent methods is to use an ensemble of 2D CNNs applied to three orthogonal views of many directions (i.e., axial, coronal, and sagittal views) [44]. Such a 2.5D approach has richer neighboring pixel spatial information with lower computational cost than 3D [154]. These studies demonstrated slightly

improved accuracy than 2D. Since a 3D volume represents a stack of adjacent 2D slices (2D image with neighbor slices), other alternatives integrated neighbor slice information to adduce a 3D temporal context for better segmentation performance. For example, Ganaye et al. [166] incorporated neighboring slices to that of the central as different input channels. Some authors investigated a 2.5D design system combining 2D and 3D methods [150, 207].

Zheng [189] used a U-Net-based architecture that provides spatially consistent results on a whole volume through propagating the segmentation across slices to perform 2D segmentation on both ventricles, including the MYO. Their network accuracy appears to be in line with manual delineations, achieving a Percentage of Good Contours (PGC, defined in [31]) of "99.21%" for LV epicardial and "97.08%" for LV cavity with the Sunnybrook dataset (see section 4.4.1). Moeskops et al. [79] proposed a 2.5D approach to assess whether a single CNN can perform several segmentation tasks. The authors proved this concept using multiple modalities (i.e., brain MRI, breast MRI, and cardiac CT angiography) for each of the three segmentation tasks. Their results showed that such a system could visualize diverse anatomical structures with multiple modalities without task-specific training. Other 2.5D approaches proposed hybrid image segmentation using a DL network fused with statistical shape modeling. For instance, Wang and Smedby [114] correlated orthogonal 2D U-Nets' outputs with a volumetric shape prior for better delineations. Their network demonstrated great results on CMRI segmentation.

4.2.3/ Fully Volumetric Approaches (3D Approaches)

In this section, we will review two state-of-the-art networks based on 3D data processing. Most of them expanded the core idea of 2D approaches and modified it to a higher dimensional space [196, 170, 70, 78]. Compared to 2D and 2.5D approaches, volumetric images may provide complete 3D information in different orientations rather than in one view or three orthogonal views. Nevertheless, one of the primary challenges of such 3D networks resides in their higher requirement of resource consumption, as a consequence of the increased size of the model parameter space, restricting their implementation.

4.2.3.1/ 3D U-Net

One of the most famous variants of U-Net architecture to reinforce it with richer spatial coherency information is 3D U-Net, proposed by Cicek et al. [70]. The authors extended the U-Net architecture via substituting 2D operations with their volumetrics counterparts. Figure 4.4 provides a schematic representation of 3D U-Net. The proposed algorithm provided dense volumetric segmentation from learned sparse 2D annotations. It densely segmented new data. Extensive results demonstrated its efficiency on a complex and

highly variable 3D structure.

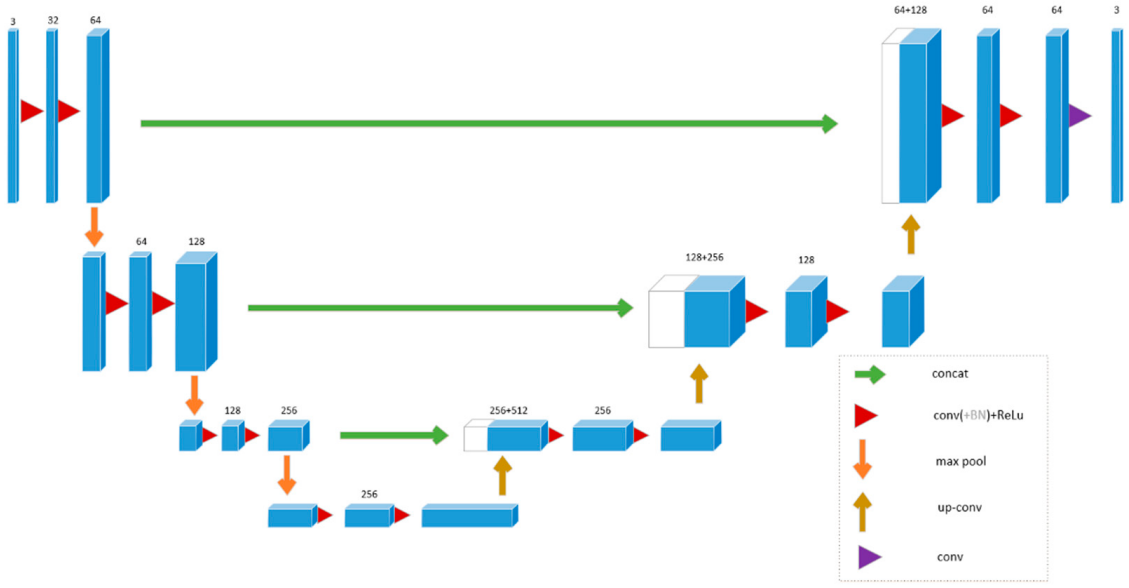

Figure 4.4: Schematic representation of 3D U-Net architecture [70].

The advent of 3D U-Net is of great interest to process volumetric images. Many volumetric segmentation methods, including LV CMR delineation, re-used the 3D U-Net model [197, 117, 91, 97, 108]. For instance, Fahmy et al. [197] proposed a 3D U-Net-based model with a sliding window to process large input stacks for accurate LGE scar quantification. The suggested method achieved consistent performance across diverse vendors. Yang et.al [117] developed a fully automatic network for ventricular structure segmentation. Their network is similar to [70] but replaces the concatenation operator with a Residual Unit (ResU). Deep supervision and transfer learning are used to improve the training process. Using Multi-class Dice Similarity Coefficient, this network reached promising results (DSC scores of “0.8037” for LV epicardial and “0.8580” for LV endocardial with the ACDC dataset (see section 4.4.4)).

4.2.3.2/ V-NET

In [78], the V-Net model to MRI prostate volume segmentation based on a volumetric CNN is proposed. Its network structure is illustrated in Figure 4.5. The authors brought a contribution to a novel objective function based on DSC. They also used 3D convolutions with a kernel size of $2 \times 2 \times 2$ and a stride of 2. The convolutions replaced pooling with the benefit of having a smaller memory footprint. PReLU non-linearities [57] were employed throughout the model. Similar to [64], it propagated features extracted from the compression path to the decompression path to assemble fine-grained detail, yielding a two-channel volumetric segmentation at the last convolutional layer. Finally, the outputs were turned into probabilistic segmentation by using soft-max voxelwise.

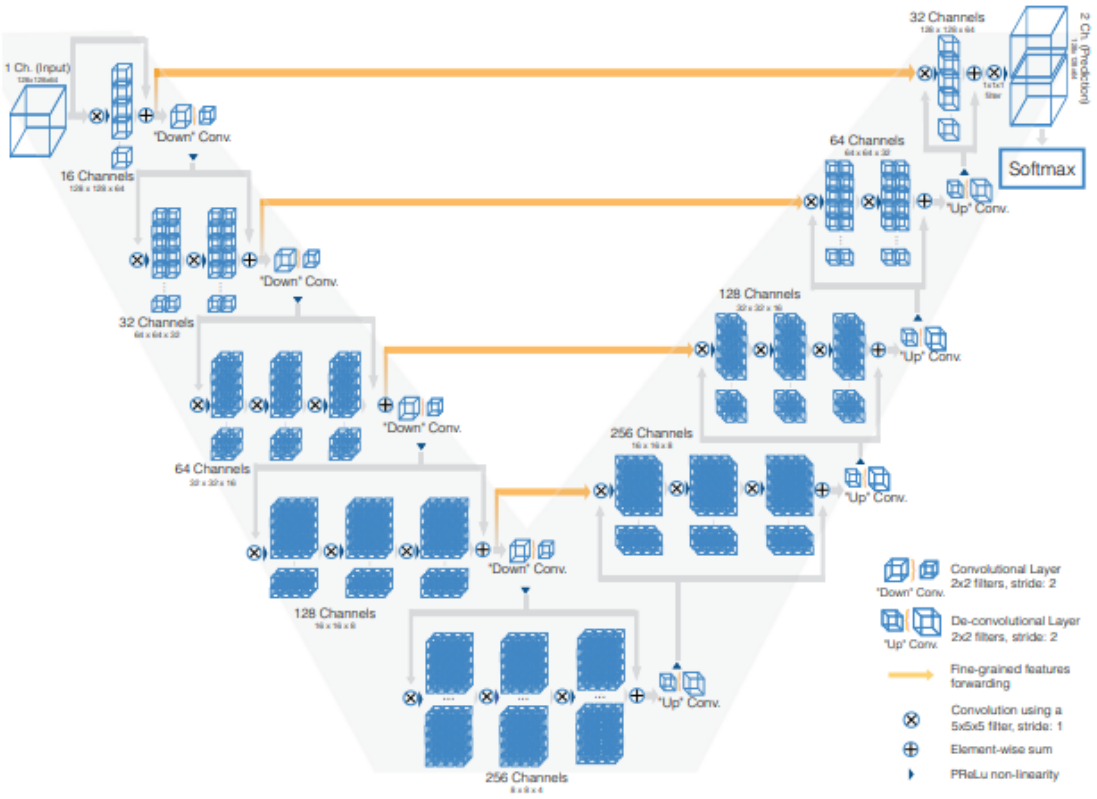

Figure 4.5: Original structure of V-Net [78].

The experimental evaluation demonstrated that V-Net model reached good performances on the "PROMISE 2012" challenge test dataset [49]. This method proved its capacity in cardiac image segmentation tasks [218, 146]. For instance, Vesal et al. [218] performed extensive experiments and interesting metrics comparison against V-Net, 3D U-Net, and several variants of the latter, including a multi-stage approach, for a multi-class segmentation on the ACDC dataset. Based on dilated convolutions and residual connections in the analysis path, the proposed multi-stage network reached a DSC score of "0.928" for LV and "0.853" for MYO delineations, compared to "0.908" and "0.809" for the V-Net and "0.889" and "0.805" for the original 3D U-Net. Gibson et al. [136] proposed deep-learning-based architecture, known as DenseVNet, with a larger receptive field to segment eight organs. Compared to [78], DenseVNet achieved remarkably higher DSC scores for all organs (e.g., "0.84" vs. "0.72" for the gallbladder, "0.76" vs. "0.68" for the esophagus, "99.21%" vs. "0.71" for the pancreas).

4.3/ DL Methods for CMRI Segmentation

CMRI is used to accurately quantify cardiac disease (e.g., scars) and assess the heart's anatomy and function. At present, CMRI draws much attention in the cardiac analysis

domain. In this section, we described several DL-based CMRI segmentation networks.

4.3.1/ VENTRICLE SEGMENTATION

As the LV plays a significant role in cardiac function assessment, many research studies have been made. We reviewed in Table 4.1 a list of bi-ventricle segmentation algorithms that have been evaluated on the ACDC dataset[1]. Our comparison comprises challenge participants' techniques and three other segmentation models that have been developed after the challenge: [156, 172, 178]. As shown, the top networks are those built by Isensee et al. [97] and Li et al. [172]. For example, compared to the classical level-set technique [93], both models reached higher accuracy, highlighting the efficiency of DL-based models.

Table 4.1: Segmentation accuracy of previous works on the testing (ACDC) dataset. Best dice value for each structure is shown in bold.

Methods	End diastolic			End systolic		
	LV	RV	MYO	LV	RV	MYO
Isensee et al. [97]	**0.968**	**0.946**	0.902	**0.931**	0.899	**0.919**
Baumgartner et al. [91]	0.963	0.932	0.892	0.911	0.883	0.901
Jang et al. [98]	0.959	0.929	0.875	0.921	0.885	0.895
Zotti et al. [125]	0.957	0.941	0.884	0.905	0.882	0.896
Khened et al. [169]	0.964	0.935	0.889	0.917	0.879	0.898
Wolterink et al. [115]	0.961	0.928	0.875	0.918	0.872	0.894
Patravali et al. [108]	0.955	0.911	0.882	0.885	0.819	0.897
Rohé et al. [110]	0.957	0.916	0.867	0.900	0.845	0.869
Tziritas and Grinias [93]	0.948	0.863	0.794	0.865	0.743	0.801
Yang et al. [117]	0.864	0.789	N/A	0.775	0.770	N/A
Li et al. [172]	0.967	0.920	**0.949**	0.902	**0.905**	0.917
Zotti et al. [156]	0.963	0.934	0.886	0.912	0.885	0.902
Painchaud et al. [178]	0.961	0.933	0.881	0.911	0.884	0.897

*Clinical metrics were also taken into account for the ranking.

4.3.1.1/ FCN-BASED SEGMENTATION

Tran [86] uses an FCN [84] to segment the LV, MYO, and RV on SA CMRI. Their automated FCN-based method reached significant segmentation performance compared

[1] Source: https://www.creatis.insa-lyon.fr/Challenge/acdc/

to classical techniques in terms of speed and accuracy. A variety of more advanced FCNs-based studies have been developed to perform remarkable improvements in segmentation performance. Indeed, much research has been conducted on optimizing the model architecture to improve the feature learning potential for segmentation [169, 173, 190, 187, 130, 98, 165]. For instance, in [169] a dense U-Net with inception modules is proposed to fuse multiscale features for accurate segmentation across images with wide anatomical variability. In [83], Poudel et al. designed a recurrent FCN (RFCN) based on GRU, a variation of LSTM [6], and FCN networks to learn image representations from 2D image stacks and perform LV segmentation. RFCN fuses detection and segmentation into a unique architecture. Multiple works [98, 117, 181, 160] introduced several loss functions (e.g., weighted cross-entropy loss, weighted Dice loss, and focal loss) for better segmentation performance. Due to CMR scans' motion artifacts, restricting the applicability of 3D approaches for segmentation [91], most FCN-based networks utilize 2D architectures, which cope better in these cases.

4.3.1.2/ Temporal and Spatial Coherence

As 2D Networks are used to process every 2D slice of a whole volume, instead of a 3D volume, the primary disadvantage of applying 2D cardiac segmentation networks is that they work slice-by-slice without learning inter-slice dependencies. Thereby, 2D models may not be sufficient to segment the LV on slices where the boundaries of the LV are not greatly delineated. Multiple studies have leveraged further contextual information such as shape priors [125, 159] to overcome this issue and thus improve 2D FCN segmentation. Several other methodologies used RNNs, and multi-slice models (2.5D models) [83, 108, 154, 164] to introduce spatial constraints, improving the segmentation of stack of slices. These models are also used to highlight Spatio-temporal information over the cardiac cycle's frames for better segmentation performances [115, 141, 149, 140, 164].

4.3.1.3/ Anatomical Constraints

The training process using only standard loss functions may fail to extract relevant anatomical structures' features. Thus, different works explored the benefit of integrating anatomical constraints at the training step for a perfect model prediction. These constraining, represented as regularization terms to consider prior knowledge (e.g., topology [162], contour [159], and shape [107, 156, 186]), force the model to produce more accurate segmentation results. For example, Oktay et al. [107] proposed an ACNN model that embeds prior knowledge into CNNs-based segmentation through an autoencoder network. Its output is enforced to follow a non-linear compact representation of the underlying anatomy. Zotti et al. [156] developed a GridNet-based network that incorporates a cardiac shape

prior to help kinetic cardiac MRI segmentation. Unlike these models, Painchaud et al. [178] developed a Variational AE (VAE) to refine the network's output through correcting non-anatomically plausible segmentation masks in the post-processing step.

4.3.1.4/ Multi-task Learning

Over the years, there is an increased interest in regularizing cardiac segmentation networks through achieving simultaneously additional tasks that are pertinent to the principal segmentation task (e.g., ventricle size classification [152] and cardiac function estimation [131]). Training a model for several tasks helps the model learn valuable features for better segmentation accuracy.

4.3.1.5/ Multi-stage Models

Various automated networks have been designed using a multi-stage pipeline, dividing the main segmentation task into subtasks [144, 154, 172, 101, 111, 205, 217]. An essential stage in the cardiac segmentation method is automatically localizing the target structure in the MRI volume to segment slices based on the localization result, reducing computational complexity. For example, Sulaiman et al. [205] first estimate a coarse density map localizing the structure of interest to then focus the second stage of the model (segmentation) in the Region(s) Of Interest (ROI). Their network achieves better segmentation performance than previous CNN-based segmentation methods. Morever, Omega-Net developed by Vigneault et al. [144] for the ACDC challenge, includes several stages: First, an initial segmentation is achieved on the input image. Subsequently, the features learned over this initial stage are employed to predict the parameters required for transforming the image into a canonical orientation. Finally, the transformed image is segmented.

4.3.1.6/ Hybrid Segmentation Approaches

Some approaches focus on fusion DL methods with traditional cardiac segmentation ones such deformable models [68, 176], graph-cut segmentation algorithms [175], and level-sets methods [106, 132] for better generalization. DL models are used for informative feature extraction and initialization steps to minimize manual interactions dependence and reach higher segmentation performance. For instance, Avendi et al. [68] adopted a CNN to detect the LV in cardiac SA images and an AE to deduce the LV shape. This deduced shape is integrated into deformable models to get the best compromise for a more accurate segmentation result. Alike, Ngo et al. [106] applied a Deep Belief Network (DBN) to direct a level-set method for accurately LV segmentation.

4.3.2/ Scar Segmentation

4.3.2.1/ Scarcity of Networks Due To A More Recent Interest

LGE-MRI is often used to put in evidence MI regions and lesions assigned to other diseases for better management of scar [7]. Earlier scar segmentation was usually achieved using traditional techniques (e.g., thresholding and clustering techniques), responsive to the local intensity variations [151]. The primary drawback is its need for manual delineation of the ROI, reducing the computational costs [69]. These techniques are not relevant for advanced research works and clinical applications.

In recent studies, DL networks have been fused with classical segmentation tools to segment scar regions. For example, the authors in [116] employed an atlas-based technique for LA identification and a DL model for fibrotic tissue detection in that area. Chen et al. [128] used an end-to-end DL method for LA and atrial scars segmentation. In this method, a multi-view CNN with a recursive attention block is proposed to improve the segmentation performance by combining features from different views.

Segmentations of MYO lesions, particularly MI and MVO delineations algorithms involving DL, are less common and more recent. Motivated by the success of DL, Fahmy et al. [133] adopted a U-Net architecture for segmenting LV MYO and scars from LGE-MRI obtained from subjects with heart disease. Moccia et al. [177], and Zabihollahy et al. [151] applied a semi-automated technique that needs manual delineation of the MYO and then used a 2D network to discriminate scars from healthy MYO. Nowadays, fully automated infarction segmentation is still a challenging task. Xu et al. [148] proposed an RNN which learns motion patterns for automatic MI segmentation from cine MRI sequences without the injection of contrast agents. Compared to the ground truth segmentation on LGE-MRI, this network achieved a great overall Dice score. De La Rosa et al. [163] proposed an automatic network for scar segmentation, including MVO regions from LGE-MRI. Their methodology is derived from VGG19 and consisted of two blocks. Firstly, healthy and diseased scans are distinguished using a classifier. Then, the MI is segmented by an initial fast coarse segmentation which is further refined by a boundary reclassification strategy. The proposed network reached state-of-the-art segmentation performances.

4.3.2.2/ EMIDEC Segmentation Networks

EMIDEC segmentation aims to automatically segment the MYO and the diseased regions on each slice of LGE-MR volume. As shown in Table 4.2, many challengers proposed two-stage networks: a) delineation of the MYO (in its first stage); b) segmentation of the myocardial diseases around the vicinity of the MYO region (in its second stage). However, some others developed one-stage networks to perform a segmentation of all the tissues

of interest in a single step.

Table 4.2: Main concepts of EMIDEC challenge methods.

Contest	Methods	Description
EMIDEC Segmentation	Camarasa et al.[a] [193]	MYO: 3D U-Net variant Scar: 3D U-Net variant
	Feng et al.[b] [198]	2D U-Net with dilated convolution
	Girum et al.[a] [199]	MYO: 2D U-Net with SE block Scar: 2 U-Net with SE block
	Huellebrand et al.[a] [201]	MYO: 2D U-Net variant Scar: Mixture model
	Yang and Wang [b] [208]	2D U-Net with SE and SK blocks
	Zhang[a] [209]	MYO: 2D U-Net variant Scar: 3D U-Net variant
	Zhou et al.[b] [210]	2D U-Net with Attention

[a] Two-stages model, [b] One-stage model.

Camarasa et al. [193] proposed two approaches to assess if the uncertainty of an auxiliary unsupervised task is helpful for myocardial infarction segmentation. As illustrated in Figure 4.6, their Baseline method first determined the ROI centered on the non-background labels to then used U-Net architecture to segment all myocardial regions from the definite ROI. Similar to the baseline segmentation, the Uncertainty-based method first localized the ROI. Then, a probabilistic Auto-Encoder is employed to provide an uncertainty map relative to ROI reconstruction. An uncertainty-based U-Net used the generated uncertainty map for myocardial delineations.

Feng et al. [198] proposed an automatic LGE-MRI segmentation model using: a) rotation-based augmentation to force the model to eliminate the image orientation and learn the anatomical and contrast relationships; b) dilated 2D U-Net to increase the robustness of the network against several slices' misalignment. The authors used the weighted cross-entropy and soft-Dice loss functions to alleviate the class imbalance issue. They also favored slices containing myocardial disease areas, which existed in few cases, particularly the MVO. Girum et al. [199] developed a two-stage CNN network to segment the anatomical structures firstly and then pathological areas from LGE-MRI. The segmented MYO tissue from the anatomical network is further employed to refine the pathological network's segmentation, thus produce the final four-class segmentation result (see Figure 4.7).

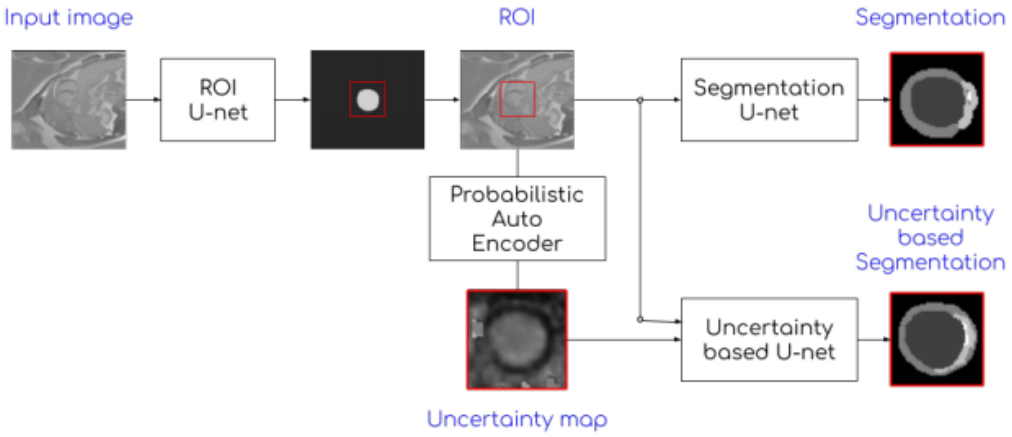

Figure 4.6: Overview of the segmentation network [193].

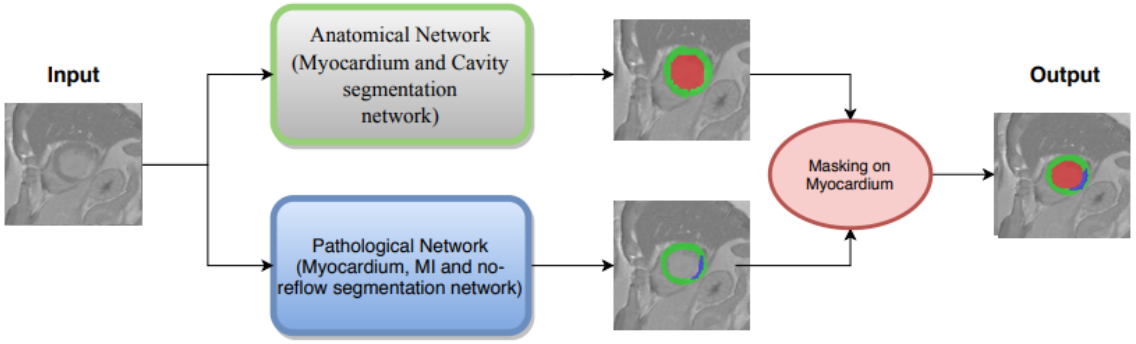

Figure 4.7: Schematic representation of the segmentation network [199].

Huellebrand et al. [201] compared a hybrid mixture model approach with two U-Net segmentations. The proposed mixture model is inspired by [39] and is suited to EMIDEC data. This model distinguished the infarct zones depending on the intensity distribution. The authors demonstrated that a better segmentation is obtained using a mixture of Rayleigh and Gaussian than a mixture of Rician and Gaussian. In addition, they realigned the image slices to avoid any inconvenience due to respiratory motions. Yang and Wang [208] proposed an improved and hybrid U-Net architecture for myocardial segmentation in LGE-MRI. The modified U-Net embodied the Squeeze-and-Excitation Residual (SE-Res) module in the encoder part and Selective Kernel (SK) block in the decoder part. The SE-Res module aimed to mold the interdependencies between features' channels and SK block to adaptatively settle the respective field. Figure 4.8 shows category and segmentation labels and hybrid branches that are used to supervise the complete segmentation process.

Zhang [209] proposed a cascaded convolutional neural network to segment myocardial areas from LGE-MRI automatically. Its method achieved the best segmentation performance. As shown in Figure 4.9, the winner first employed 2D U-Net to focus on the intra-slice information for a preliminary segmentation, and then a 3D U-Net to use the

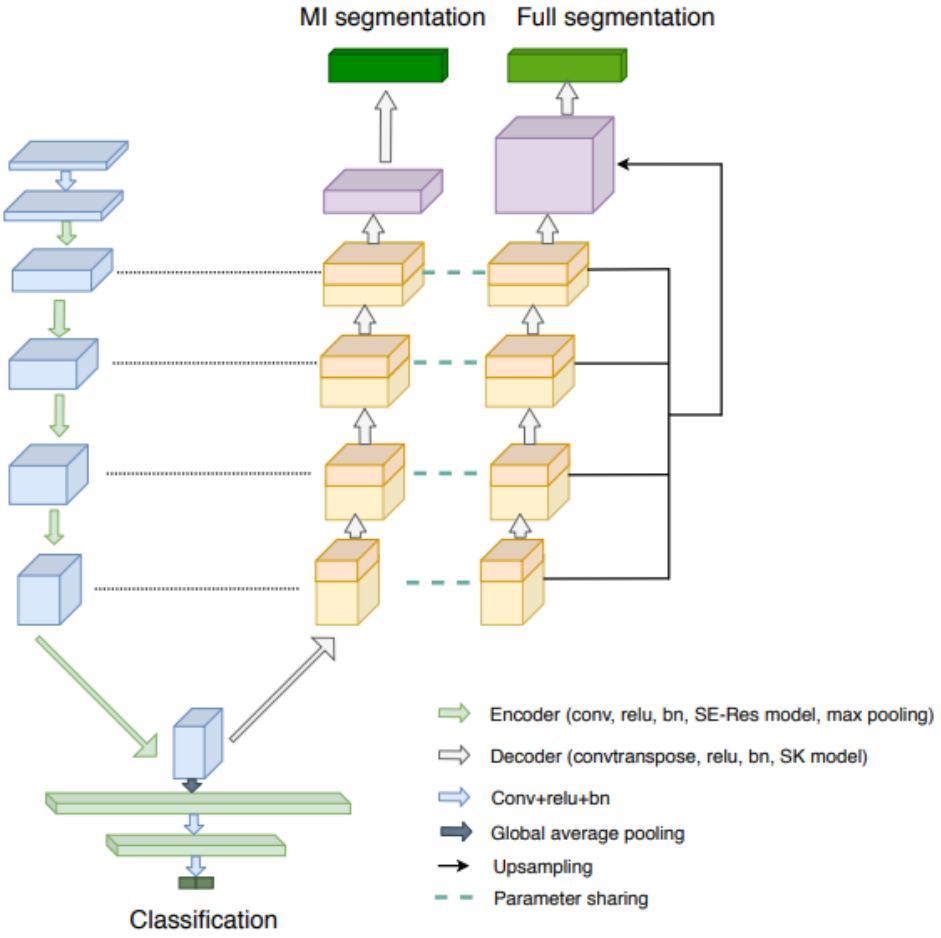

Figure 4.8: Overall architecture of the segmentation network [208].

volumetric spatial information for a better segmentation based on both original volume and 2D segmentation. Finally, post-processing removing all the scattered pixels from the latest segmentation is applied to yield the final segmentation.

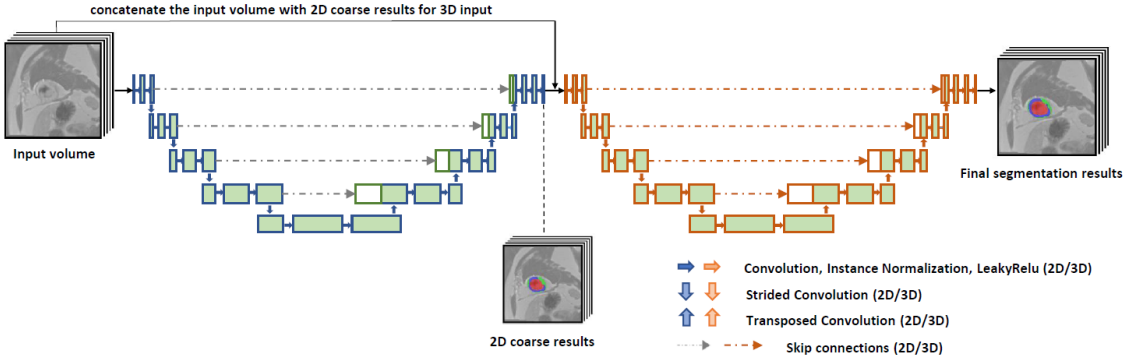

Figure 4.9: Framework of the cascaded convolutional neural network [208].

Zhou et al. [210] developed an anatomy prior-based network, which fuses the U-Net segmentation architecture with attention blocks (see Figure 4.10). They also presented a

neighborhood penalty strategy to evaluate the inclusion relationship among the MYO and diseased regions and a data augmentation technique based on the mix-up strategy [123] to interpolate two images and their corresponding segmentation maps.

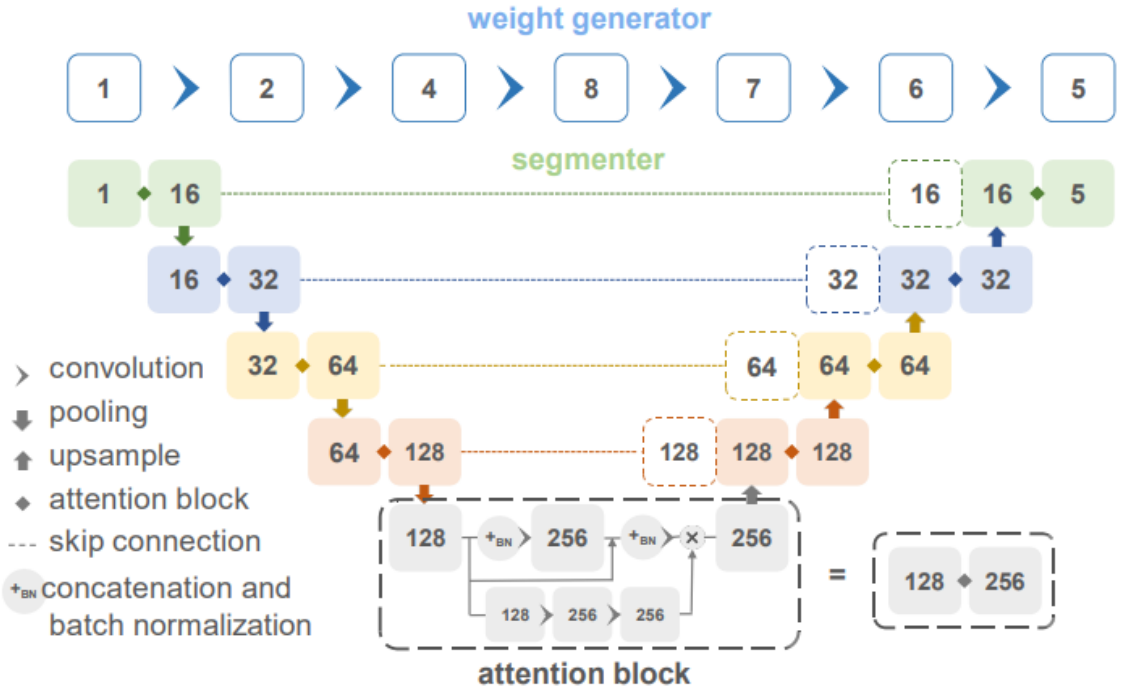

Figure 4.10: Schematic representation of anatomy prior based U-Net architecture [210].

4.3.3/ Automatic Whole Heart Segmentation

DL-based segmentation has been extensively used to segment the principal heart's substructures in 3D MRI, as the primary step for diagnosis and treatment planning [120, 88, 76, 143]. The authors in [120] applied a 3D dense FCN to 3D MR scans for MYO and blood pool segmentation. Thanks to the availability of benchmark datasets for whole heart segmentation, DL-based networks used in recent medical image segmentation research segment more specific substructures (e.g., aorta, MYO, and four chambers) from 3D MRI.

4.4/ Existing CMRI Datasets for the Task

The heterogeneous aspect of the tissue of interest (huge size, shape, and location variations from one subject to another [99]) is one of the main challenges in medical image segmentation. In addition, the requirement for a proper dataset is still critical to reaching coherent segmentation results. Thus, some prevalent challenges are established to

achieve accurate LV segmentation and benchmark several CMR segmentation networks. Table 4.3 depicts the MRI cardiac dataset details mentioned below.

Table 4.3: Summary of benchmarking CMRI datasets available for comparison goals.

Name	Year	Nb subjects		Ground truth			
		Train	Test	LV	RV	MYO	Pathology
Sunnybrook	2009	45	-	✔	✘	✔	✔
LV	2011	100	100	✔	✘	✔	✘
LivScar	2012	10	20	✔	✘	✔	✔
ACDC	2017	100	50	✔	✔	✔	✔
EMIDEC	2020	150	50	✔	✘	✔	✔

4.4.1/ SUNNYBROOK CMR LV SEGMENTATION CHALLENGE - MICCAI 2009

The Sunnybrook Cardiac Data (SCD)[2] contains 45 cardiac cine MRI images from a fusion group of subjects and several pathologies: hypertrophy cardiomyopathy, HF with infarction, HF without infarction, and healthy. The MRI images are provided with a set of hand-drawn delineations, given in text files, for both endocardium and epicardium [31]. The data were acquired with a 1.5T GE Signa MRI and temporal resolution of 20 cardiac phases for 10-15 second breath-holds. Recent works [52, 68, 85] reported several segmentation approaches' results achieved since the SCD challenge.

4.4.2/ LV SEGMENTATION CHALLENGE (LVSC), MICCAI-STACOM 2011

The database comprises CMR acquisitions in long axis and SA views from 200 subjects with coronary artery disease and prior MI. Binary segmentation masks of the MYO for the 100 training subjects were provided. It is made disposable via the Cardiac Atlas Project [37]. Multiple MRI scanners were used: GE Medical Systems (Signa 1.5T), Philips Medical Systems (Achieva 1.5T, 3T, and Intera 1.5T), and Siemens (Avanto 1.5T, Espree 1.5T, and Symphony 1.5T). The data are a clinically significant subject group as mass and volume are fundamental diagnostic indicators of adverse cardiac remodeling. This challenge[3] highlights LV segmentation approaches' performances [55]. This survey generated consensus segmentation images based on the STAPLE algorithm [16] using three semi- and two fully automated networks of contributing participants (raters).

[2] Source: http://smial.sri.utoronto.ca/LVChallenge/Home.htmls/
[3] Source: www.cardiacatlas.org/challenges/lv-segmentation-challenge/

4.4.3/ VENTRICULAR INFARCT SEGMENTATION CHALLENGE (LIVSCAR), MICCAI 2012

The LivScar dataset is presented in the review [75]. The database[4] contains 30 LGE-MRI of humans (nh=15) and pigs (np=15), obtained from two imaging centers (see Figure 4.11). A myocardial mask, manually drawn by an expert observer using SA view slices, was publicly available. The human and porcine data were acquired with a 1.5T MR unit (Philips Achieva, The Netherlands) and 3T MRI unit (Siemens Healthcare, Germany), respectively. An exciting characteristic of this dataset is its heterogeneous image quality, which is helpful to perform the robustness of a network.

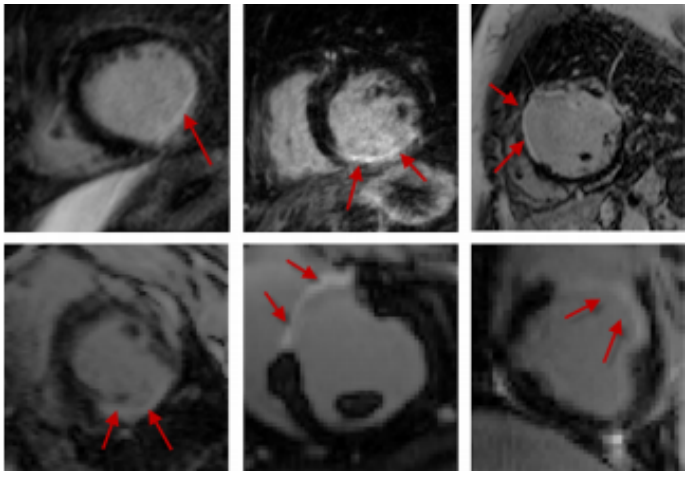

Figure 4.11: A sample of LivScar dataset. (top-row) Human; (bottom-row) Porcine [75].

4.4.4/ AUTOMATED CARDIAC DIAGNOSIS CHALLENGE (ACDC), MICCAI-STACOM 2017

The ACDC dataset [126] was acquired in clinical routine at the University Hospital of Dijon (France) with two MRI scanners of magnetic strengths ((1.5T - Siemens Area and 3T - Siemens Trio Tim), Siemens Medical Solutions, Germany). The expert annotations are manually delineated 3D volumes of the MYO, the LV and RV cavities, at end-systolic and end-diastolic slices. A set of SA view slices cover the LV, with a thickness from 5 mm to 10 mm and at times an interslice gap of 5 mm. The data coat different pathologies with enough patients to efficiently train deep-based networks and evaluate the primary physiological parameters' variability acquired from cine MRI. The dataset includes SA view MRI for 150 subjects evenly contains five classes: (NOR: patients with normal cardiac anatomy, MINF: patients with MI, DCM: patients with dilated cardiomyopathy, HCM: patients with hypertrophic cardiomyopathy, and ARV: patients with abnormal RV). Figure 4.12 presents a visualized example.

[4] Source:https://www.doc.ic.ac.uk/~rkarim/la_lv_framework/lv_infarct/index.html/

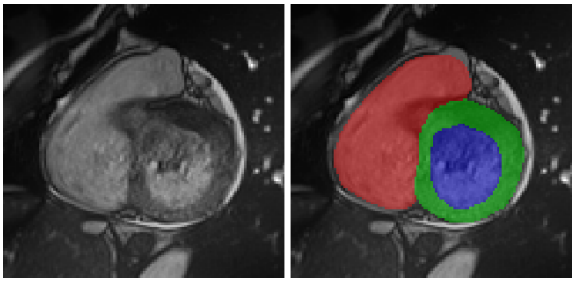

Figure 4.12: Visualized examples in ACDC challenge. (left) Input image. (right) Ground truth [126].

4.4.5/ Automatic Evaluation of Myocardial Infarction from Delayed-Enhancement CMRI (EMIDEC) Challenge, MICCAI-STACOM 2020

The EMIDEC dataset [202] comprises 150 clinical exams with LGE-MRI in SA view covering the LV from healthy subjects (nh=50) or cases with MI (ni=100), using a NIfTI format, and their respective myocardial annotations (i.e., the MYO, MI, and MVO). The EMIDEC challenge[5] aims first to classify whether the patient is healthy or pathological from the attached clinical characteristics (e.g., age and ECG), available on a text file, with or without LGE-MRI, and then automatically segment the several relevant regions (the LV MYO, MI, and MVO). All acquisitions were performed with a 1.5 T and a 3T (Siemens Medical Solution, Erlangen, Germany) 10 minutes after injecting a contrast agent (Gd-DTPA; Magnevist Schering- AG, Berlin, Germany). The data include a stack of SA view slices with a slice thickness of 8 mm and pixel spacing between 1.25×1.25 mm^2 and 2×2 mm^2. The number of slices goes from 5 to 10 per exam. EMIDEC challenge presents these principal issues: data imbalance, low contrast, heterogeneous appearances of diseased regions, and various SA views. To the best of our knowledge, the EMIDEC challenge is the first one that provided annotated data and clinical information for improving methods' classification and segmentation.

4.4.6/ Other Datasets

To evaluate performances of CMRI segmentation approaches, other international challenges, providing LGE-MRI and manual delineations, have been organized over the MICCAI conference (e.g., the MS-CMRSeg challenge[6] and the MyoPS challenge[7]). Although, their subjects' number was inferior to that in the EMIDEC dataset. Visualized samples in both segmentation tasks are shown in Figure 4.13 and Figure 4.14.

[5] Source: http://emidec.com//
[6] Source: https://zmiclab.github.io/projects/mscmrseg19/
[7] Source: http://www.sdspeople.fudan.edu.cn/zhuangxiahai/0/MyoPS20/

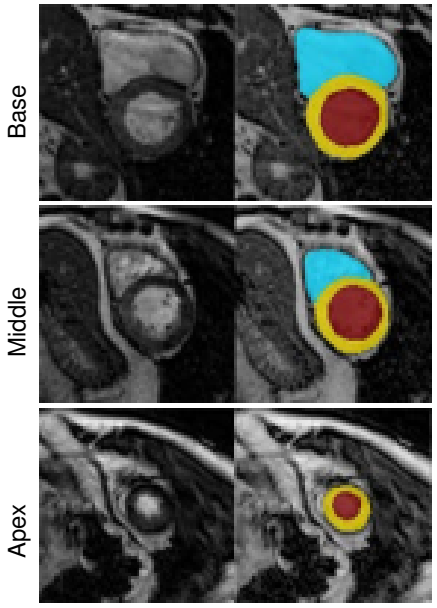

Figure 4.13: Visualized examples in MS-CMRSeg challenge. Rows from top to bottom represent the basal, middle and apical slices, respectively. (left) Input image. (right) Ground truth [180].

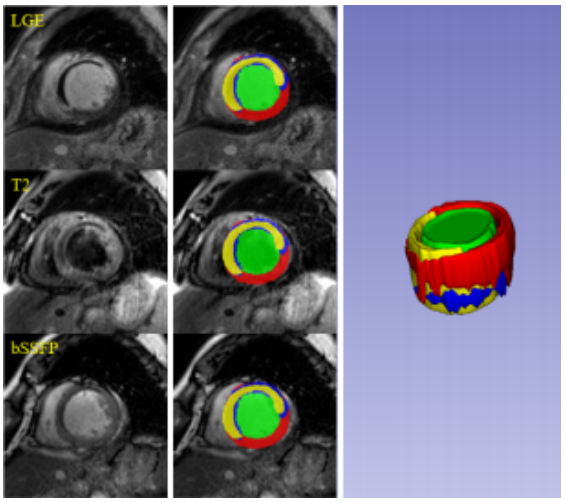

Figure 4.14: Visualized examples in MyoPS challenge. From Left to Right: Input image, Ground truth, and 3D rendering [216].

4.5/ CONCLUSION

This chapter reviewed existing CMR datasets and algorithms for cardiac image segmentation to give a global overview of advanced networks performed on LV, myocardial, and infarct segmentation, the main concerns in this thesis. Based on the reported assessment, we compared previous works on segmentation benchmark datasets. The presented state-of-the-art provides a global starting layer from which the idea of our delineation methodologies has been deepened.

II

CONTRIBUTION

5

Proposed Methodology

This thesis aims to design deep network models for automatic myocardial segmentation on LGE-MRI and find hyperparameters that provide the best performance. Based on the survey of segmentation techniques described above, this chapter focuses on the approaches applied to solve the infarct segmentation' issue. A comprehensive myocardial quantification on cardiac LGE-MRI implementation has been designed in a Python environment on a Tesla V 100 machine with four embedded GPU.

5.1/ Overview of the Proposed Process

As mentioned above, we developed DL-based methodologies for infarct segmentation on LGE-MRI. The proposed process first applies a pre-processing stage on the whole EMIDEC dataset. The processed LGE-MR images are then passed through proposed models to provide a myocardial segmentation map. The labeling of the target regions is finally post-processed, remapping it to the original volume size and smoothing the segmentation result. The details of the process stages are summed up in the following sections.

5.2/ Data Processing

In this work, the EMIDEC dataset was used for assessment purposes. This section will depict the data processing (i.e., pre-processing including data dimension choice and post-processing methods). It is a necessary stage in DL-based image segmentation.

5.2.1/ Pre-processing

Data pre-processing task was performed before models training and testing to efficiently prepare the data for the following myocardial segmentation step. Particularly, target im-

ages and their associated labels were cropped to a normalized set whose center was the centroid of the LV cavity tissue to reduce the processing area. A reduction of the original data dimension is required to remove unnecessary information and accelerate the segmentation processing. An automatic crop function is proposed to determine a sub-volume containing myocardial tissues in all SA slices from the LGE-MRI.

Since EMIDEC data size varied from subject to subject, cropped LGE-MRI sizes were standardized. To this end, all MR volumes were resized to $96 \times 96 \times 16$ pixels^3 volume size (i.e., the best minimum crop size found) through adding empty slices [203].

The resulting images were further processed through standard adaptive histogram equalization technique to enhance the image quality [5, 206] and a non-local mean denoising to smooth the image [17]. The preprocessed image results can be observed in Figure 5.1.

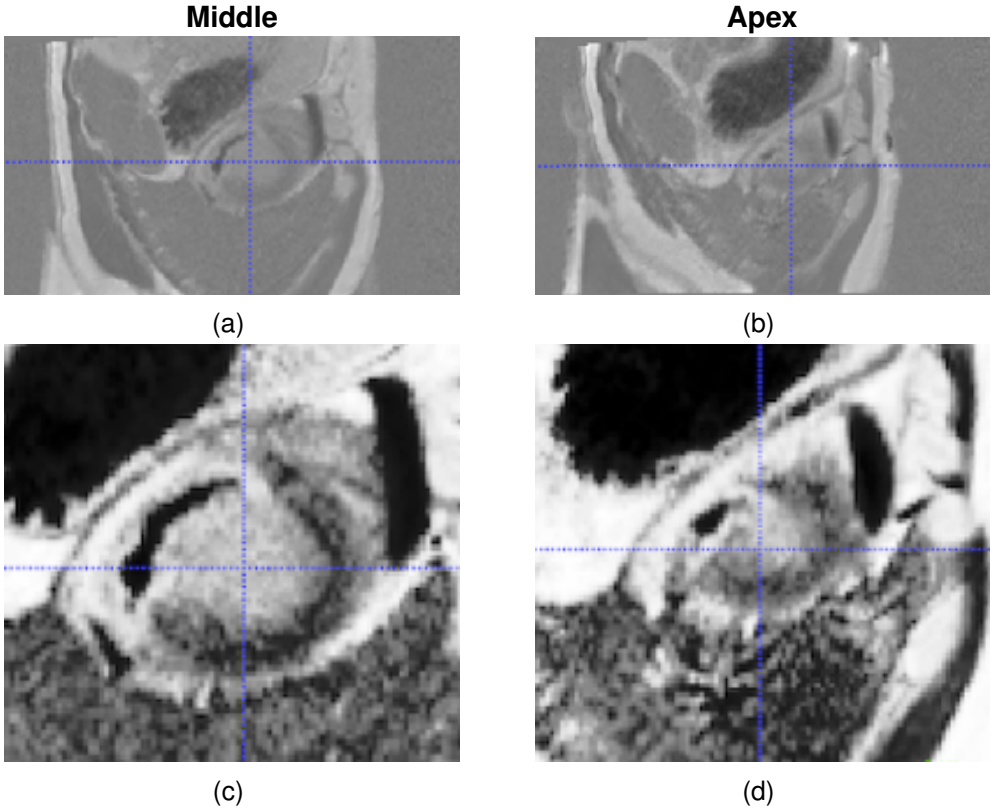

Figure 5.1: Two LGE-MRI slices of a patient, showing the original image (a, b) and the preprocessed image (c, d).

5.2.2/ Post-processing

Post-processing was required as the last stage in the segmentation pipeline for an accurate smoothing of prediction contours while removing noisy predicted tissues. This computational step will improve the quantification performance, including false-positive

reduction. A mathematical morphology image opening operation with a kernel size of 3×3 is performed to exclude any isolated or small predicted segments with a minimum setting size of 64 voxels from the segmentation result. We also used connected components for better segmentation of diseased regions in the whole slices in LGE-MRI stacks.

A majority voting technique based on all fusions of segmentation maps, obtained with varying training parameters, is required to increase sensitivity for segmenting myocardial tissues, yielding the desired results. For example, the voxel was labeled as MI if at least three out of the proposed models' outputs predicted this voxel as an MI label. The final segmentation network (or ensemble) that achieves the highest DSC on the training set is automatically chosen. In the last step, labeled cropped slices were resized to the original volume size.

5.3/ NETWORK ARCHITECTURES

This section presents an end-to-end overview of our proposed models. We achieved the myocardium quantification issue using three approaches: the 2.5D SegU-Net framework and 3D constrained frameworks based on volumetric U-Net architecture. Significant reasons motivated the choice of these approaches. As reported in the previous chapters, 2D U-Net, 3D U-Net, and 2.5D methods achieved outstanding performance in medical segmentation. Several authors have also introduced anatomical constraints, contextual information, and advanced building blocks such as inception modules and atrous spatial pyramid pooling to improve image segmentation.

5.3.1/ ALGORITHM 1: SEGU-NET

Algorithm 1: SegU-Net

Khawla Brahim, Abdul Qayyum, Alain Lalande, Arnaud Boucher, Anis Sakly, and Fabrice Meriaudeau.
A Deep Learning Approach for the Segmentation of Myocardial Diseases
25th International Conference on Pattern Recognition, (ICPR), IEEE, ISBN 978-1-7281-8808-9, pages 4544–4551, May 05, 2021.
DOI: 10.1109/ICPR48806.2021.9412793

The first network we proposed for the myocardial segmentation issue is called 2.5D SegU-Net. The algorithm is a hybrid of SegNet [90], and U-Net [64] networks. The schematic view of our approach can be seen in Figure 5.2. In total the proposed model has 29 convolutional layers, 3×3 filter kernel of convolution, and an increased number of filters from 64 to 512 for extracting different feature representations. Our proposed methodology

has a U-shaped encoder-decoder architecture. Max pooling indices [90] and skip connections [64] are incorporated to improve myocardial segmentation. The yellow arrows indicate the pooling indices and skip connections between the contracting part and the expansive part. Indeed, the proposed algorithm benefits from U-Net and SegNet based architectures, i.e., the capacity to capture fine image details and the computational efficacy. The model output for each input of sub 2.5D was one segmentation map with a size of $224 \times 224 \times 3$, representing the predicted category of each pixel relative to the tissue type (MYO, scar, MVO, or background (BG) areas). The loss function was weighted to alleviate the class imbalance issue. The process is repeated for 100 epochs, using the following parameters: Batch size = 2, Adadelta [41] as the optimizer algorithm, BN, and ReLU activation function were done on each layer of the model structure, and a multi-class softmax classifier with four labeled outputs: BG (0), MYO (1), MI (2), and MVO (3) as a model prediction.

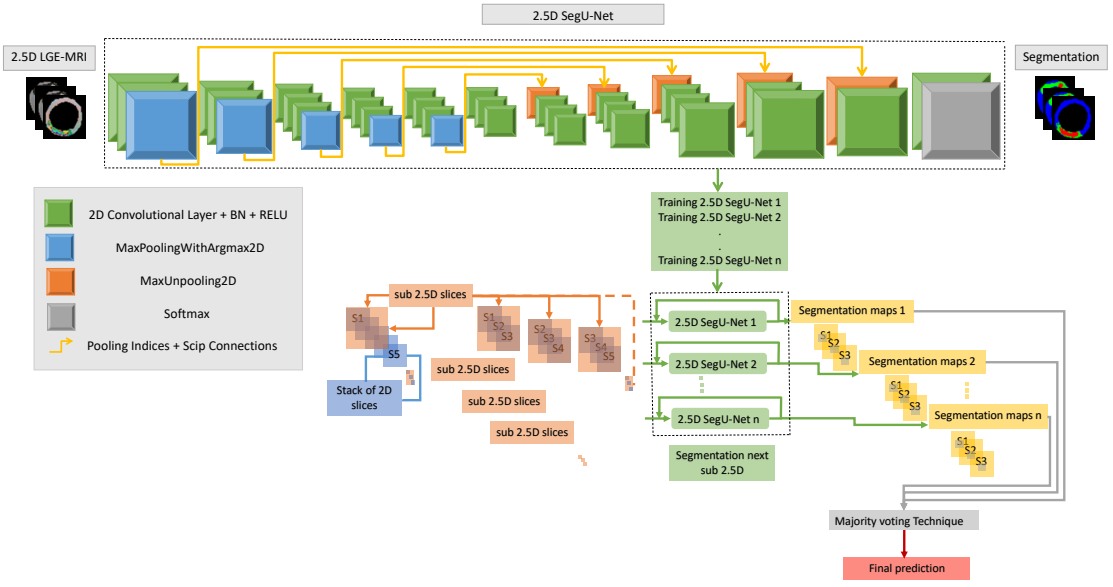

Figure 5.2: Architecture of the proposed 2.5D SegU-Net network based on late-combination method for myocardial segmentation.

Consider a stack of n "rgb" slices $(224 \times 224 \times 3 \times n)$, we create a sub 2.5D from each three consecutive slices, resulting in n–2 sub 2.5D of size $224 \times 224 \times 3$, which contain spatial information of the 3D data. As a consequence of sub 2.5D overlapping, the majority of slices were processed three times. We varied estimated training parameters for better myocardial segmentation performance. The proposed model has been implemented using Tensorflow (version 1.14.0) and Keras (version 2.3.1) libraries.

5.3.2/ ALGORITHM 2: SPIU-NET

Algorithm 2: SPIU-Net

Khawla Brahim, Abdul Qayyum, Alain Lalande, Arnaud Boucher, Anis Sakly, and Fabrice Meriaudeau.
A 3D Network Based Shape Prior for Automatic Myocardial Disease Segmentation in Delayed-Enhancement MRI
IRBM, Elsevier, Date of Publication: February 15, 2021.
DOI: 10.1016/j.irbm.2021.02.005

Our second algorithm, SPIU-Net, improves the U-Net architecture by extending a shape prior constraint to help handle anatomical inconsistencies. We also incorporated several blocks (i.e., CBAM (Convolutional Block Attention Module), inception residual, and EDP (Expansion, Depth-wise, and Projection layers) blocks to the proposed algorithm).

Figure 5.3 shows our proposed shape prior-based model for fully myocardial segmentation. Segmenting the MYO is a significant stage towards identifying both healthy MYO and MI. The SPIU-Net model comprises two essential steps. We first introduce the anatomical network to segment the MYO and LV cavity structures. Then, the 3D pre-trained Autoencoder network and the 3D U-Net architecture were fused to produce the final myocardial segmentation. Details of each stage are explained in the following paragraphs.

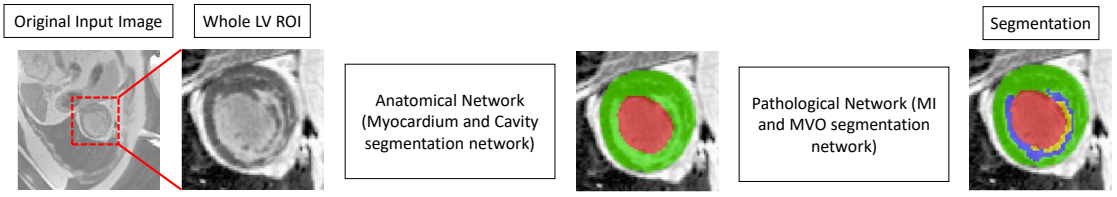

Figure 5.3: Workflow of the SPIU-Net segmentation approach with two components: anatomical and pathological networks. As mentioned above, we first crop the ROI. An anatomical network is then applied to the ROI images to segment the LV cavity and the MYO regions. Finally, a pathological network is proposed to identify damaged areas (scar and MVO) from MYO segmented tissues. The red, green, blue, and yellow colors denote the LV cavity, the MYO, scar, and MVO, respectively.

5.3.2.1/ ANATOMICAL NETWORK

The proposed anatomical model is built based on an encoder-decoder architecture. We have introduced the proposed CBAM in the encoding path and the proposed EDP block in the decoding path. A modified attention module has been used in concatenated shortcut connections to pass contextual and positional features from the contracting path to the

extracting path.

The features maps are aggregated from several branches using kernels of different sizes in the inception residual block. The residual connections provide smooth learning regarding the layer inputs, rather than learning an unreferenced function [66]. The proposed anatomical network is shown in Figure 5.4.

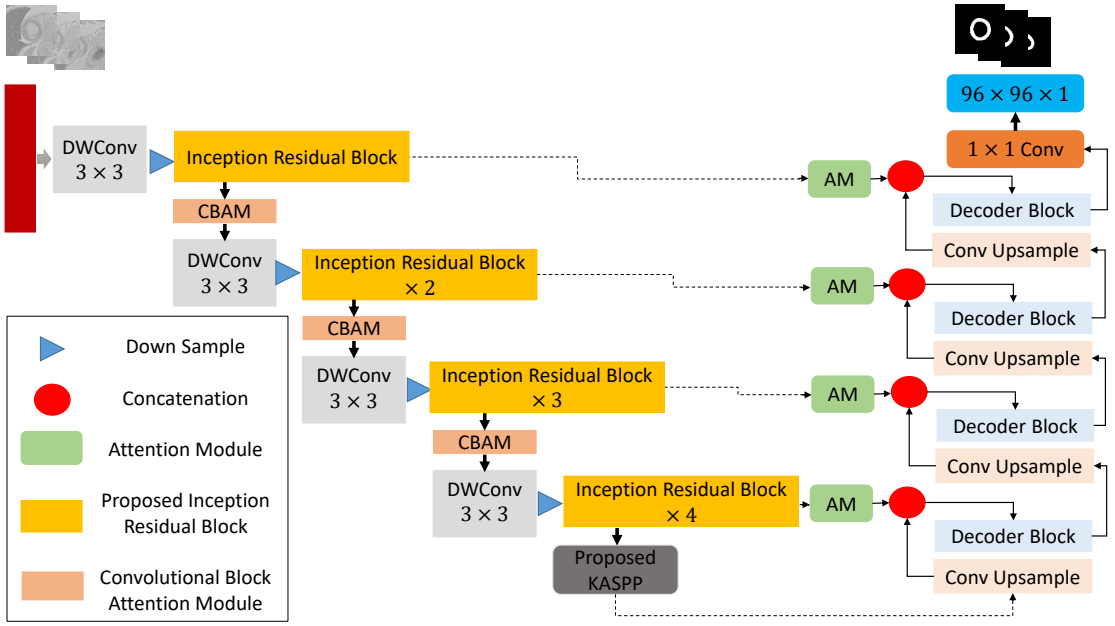

Figure 5.4: Overview of the proposed anatomical network based on inception residual, CBAM, and decoder (EDP) blocks for accurate myocardium segmentation.

Figure 5.5 shows the detailed architecture setting of the inception residual block. Compared with the original inception residual module, BN layer has been used after each convolutional layer, excluding bottleneck layers. We used 1×1 and 3×3 kernel, and also introduced 5×5 kernel branch as inspired by the DeepLab network [129]. BN layer makes smooth training and may avoid gradient vanishing while keeping convolutional layers. At each inception residual block we doubled the number of feature channels. The feature maps are aggregated through convolving with three kernels (i.e., 1×1, 3×3, and 5×5). The 3×3 and 5×5 kernels are further decreased into 1×3, 3×1, 1×5, and 5×1 to minimize the number of training parameters.

Given x_l is the output of the l^{th} layer, $c_{(n\times n)}(.)$ is a $n \times n$ kernel convolutional layer, $c_b(.)$ designates the BN layer, and 1×1 Conv denotes the bottleneck layer. The output of each inception residual block is summarized in Eq. 5.1.

$$x_{l+1} = c_{1\times1}(c_{1\times1}(x_l)).c_b(c_{3\times3}(c_{1\times1}(x_l))).c_b(c_{3\times3}(c_b(c_{3\times3}(c_{1\times1}(x_l))))).c_b(c_{5\times5}(c_b(c_{5\times5}(c_{1\times1}(x_l))))) + x_l \tag{5.1}$$

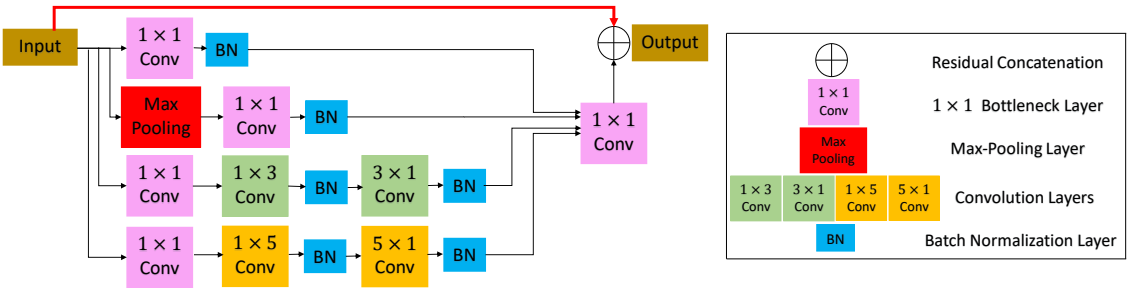

Figure 5.5: Proposed inception residual block.

We have incorporated the EDP block into the expanding path to extract pertinent semantic information. The overall graphic scheme of the decoder block is presented in Figure 5.6.

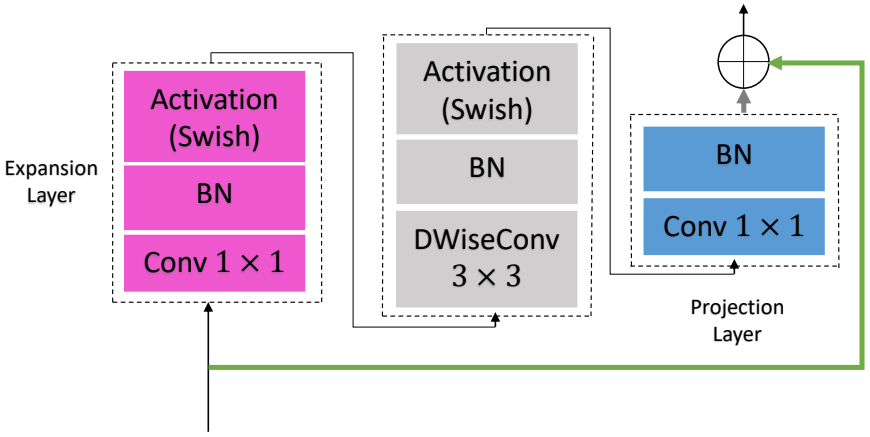

Figure 5.6: Proposed EDP block.

Woo et al. [145] proposed the CBAM, which extract attention maps and multiply them by input feature maps to get adaptive feature refinement. The channel and spatial attention maps are generated by exploiting features' inter-channel and inter-spatial relationships, respectively. Every channel of a feature map is considered a feature detector. The feature descriptors are produced by applying both average-pooling and max-pooling operations along the channel axis and concatenated them. Using pooling operations is supposed to be efficient in highlighting informative significant areas. The 1×1 2D convolutional layer is applied to the 2D descriptor, getting the raw attention map. A swish-based sigmoid function is employed on the final attention map. In the experiment, the spatial attention module is used before the channel attention module, providing better performance (see Figure 5.7).

Huang et al. [167] introduced a Kernel-Sharing Atrous Convolutional (KSAC) layer in Atrous Spatial Pyramid Pooling (ASPP) module. The 3×3 kernel is shared with atrous convolutional layers with different dilation rates. In the proposed algorithm, we have extended KSAC and combined several features extracted from the convolutional path with

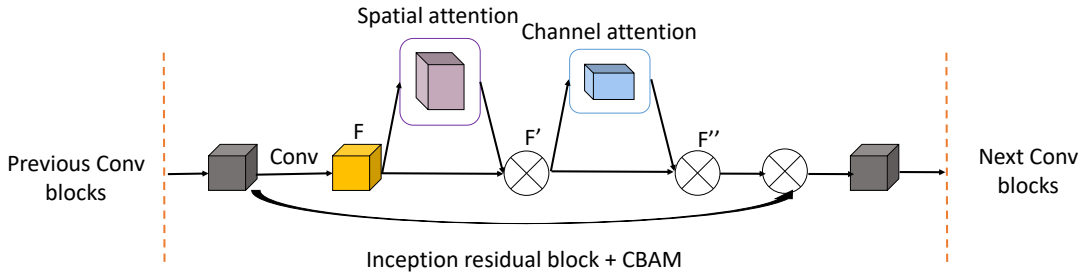

Figure 5.7: Proposed CBAM.

different scale (5 scales) in the KASPP. The proposed K-Atrous Spatial Pyramid Pooling (KASPP) module (see Figure 5.8) extracted multi-scale contextual information from the downsampling path of the anatomical network.

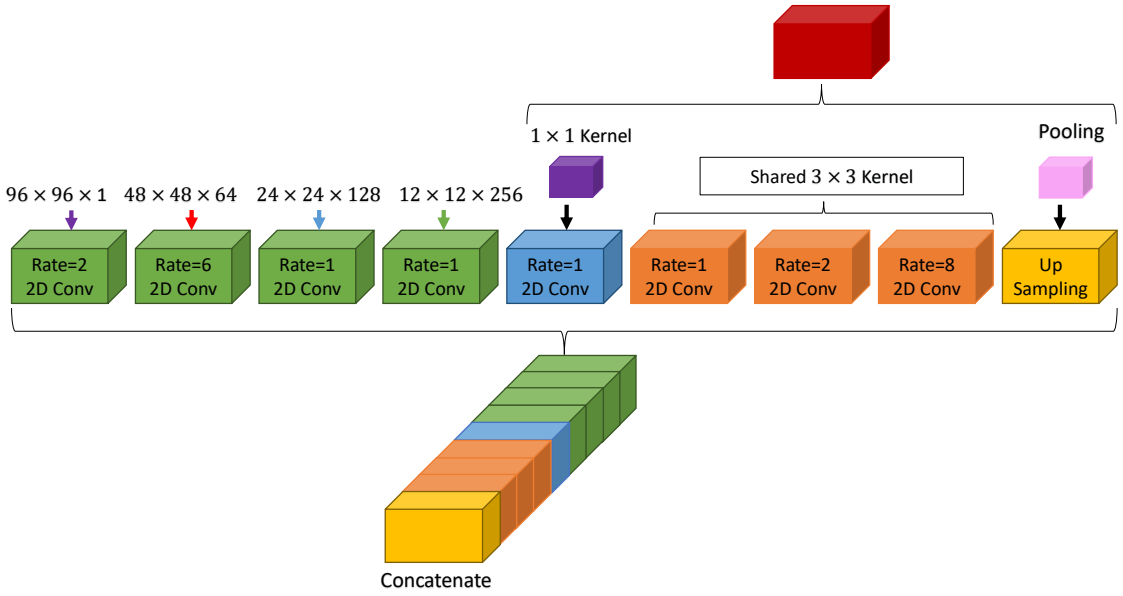

Figure 5.8: Proposed KASPP module.

5.3.2.2/ PATHOLOGICAL NETWORK

In this stage, we proposed to improve myocardial segmentation consistency with deep network predictions by incorporating prior constraints. As shown in Figure 5.9, our 3D pathological network combines 3D U-Net with a Shape-Reconstruction (SR) module to constrain prior knowledge shape [186]. 3D Autoencoder aims to accurately encode and reduce the original input volume, which may be reconstructed from the encoded representation. A pre-trained 3D Autoencoder is an effective model to regularize the segmentation output into a realistic shape. It is connected to the 3D U-Net and takes the segmented volume as input. A regularization term is proposed to restrain the segmentation output. In experiments, we choose to extract volume patches of size $12 \times 12 \times 12$ pixels^3, yielding the

best-obtained results for damaged myocardial segmentation. The proposed pathological network was implemented using the Chainer library, Batch size of 4, and Adam optimizer with a learning rate $\alpha = 10^{-4}$.

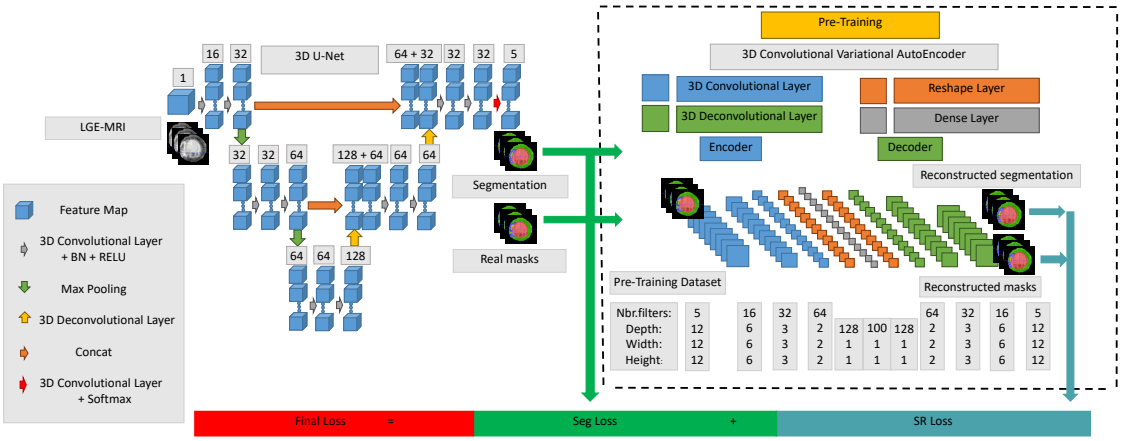

Figure 5.9: Overall network structure of our 3D pathological approach for myocardial disease segmentation. The number of channels is denoted above every feature map.

The proposed algorithm used the 3D U-Net architecture. In short, successive convolution-pooling layers are introduced in the contracting path to capture more high-level semantic features. The feature maps are then up-sampled to retrieve the localization for each voxel. Skip connections concatenated symmetrically features from contracting and expanding pathways to recover fine-grained details in the prediction. In the last layer, a $1 \times 1 \times 1$ convolution reduced the output channels' number to that of the predicted categories (i.e., five in our myocardial segmentation task).

The 3D regulariser network has a fully connected layer, including five neurons denoting the predicted categories (BG, LV cavity, MYO, MI, and MVO areas). The weights of the pre-trained 3D Convolutional Variational AutoEncoder (CVAE) network were first transferred. Then, they were fine-tuned via using Adam optimizer over the training data. The pre-trained CVAE architecture has in-depth knowledge about segmenting different feature representations' types, and by fine-tuning its training parameters, it learns the present task feature representations.

In segmentation, we used the Jaccard loss function, which is a metric-inspired loss based on a Jaccard score, computing the overlap between two objects [122]. A weighted Jaccard (wIOU) and a mean weighted Jaccard (mwIOU) are two loss functions using the class weights and the weight coefficient's ratio to the sum of the weight coefficients, respectively. To alleviate the class imbalance between relatively small segmentation categories and the extensive BG, we optimize the summation of a Jaccard-based (i.e., wIOU or mwIOU) loss and a shape constraint loss. In short, the following equation gives the final loss function used for training the proposed pathological network.

$$L_{Final} = L_{Seg} + \lambda_{SR} \times L_{SR} \tag{5.2}$$

where L_{Seg} represents the wIOU or mwIOU based loss function, λ_{SR} denotes the regularization term and L_{SR} indicates the L2 loss function that is defined in Frobenius norm Eq. 5.3. $\lambda_{SR} = 10^{-2}$ was found to be the best choice.

$$L_{SR} = \sum_{i=1}^{n} ||RP_i - RG_i||_F^2 \tag{5.3}$$

where n denotes the total number of training volumes, RG_i is the reconstructed ground truth, RP_i is the reconstructed predicted segmentation and $||.||_F$ representes the Frobenius norm of an $m \times n$ matrix.

5.3.3/ Algorithm 3: ICPIU-Net

Algorithm 3: ICPIU-Net

Khawla Brahim, Tewodros Weldebirhan Arega, Arnaud Boucher, Stephanie Bricq, Anis Sakly, and Fabrice Meriaudeau.
An Improved 3D Deep Learning-Based Segmentation of Left Ventricular Myocardial Diseases from Delayed-Enhancement MRI with Inclusion and Classification Priors Information U-Net (ICPIU-Net)
Submitted to Computer Methods and Programs in Biomedicine, Elsevier, September 15, 2021.

The pipeline of our last algorithm, ICPIU-Net, is displayed in Figure 5.10. Since myocardial diseases (scar and MVO) are ensured to be localized within the MYO, it makes sense to first segment the MYO and LV cavity to remove other hyper-enhanced and hypo-enhanced regions of the LGE-MRI.

A block diagram of our ICPIU-Net approach is presented in Figure 5.11. In the training phase, Anatomical-Net and Pathology-Net were trained separately on 100 LGE-MRI. 50 LGE test MRIs were passed to the trained network to produce the corresponding segmentation maps in the testing phase. Each stage's details are described below.

5.3.3.1/ Anatomical Network

The segmentation methods used in the proposed anatomical network are inspired by the state-of-the-art nnU-Net [214] architecture with default settings. nnU-Net is a fully automatic segmentation network based on U-Nets [64] structure. It adapts to any new

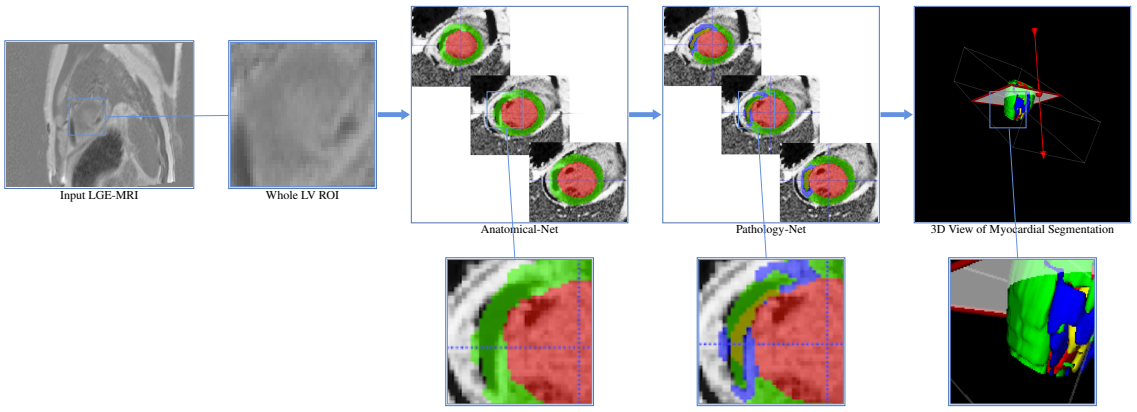

Figure 5.10: Pipeline of our proposed ICPIU-Net network for automatic myocardial disease segmentation. The red, green, blue, and yellow colors represent the LV cavity, the MYO, MI, and MVO.

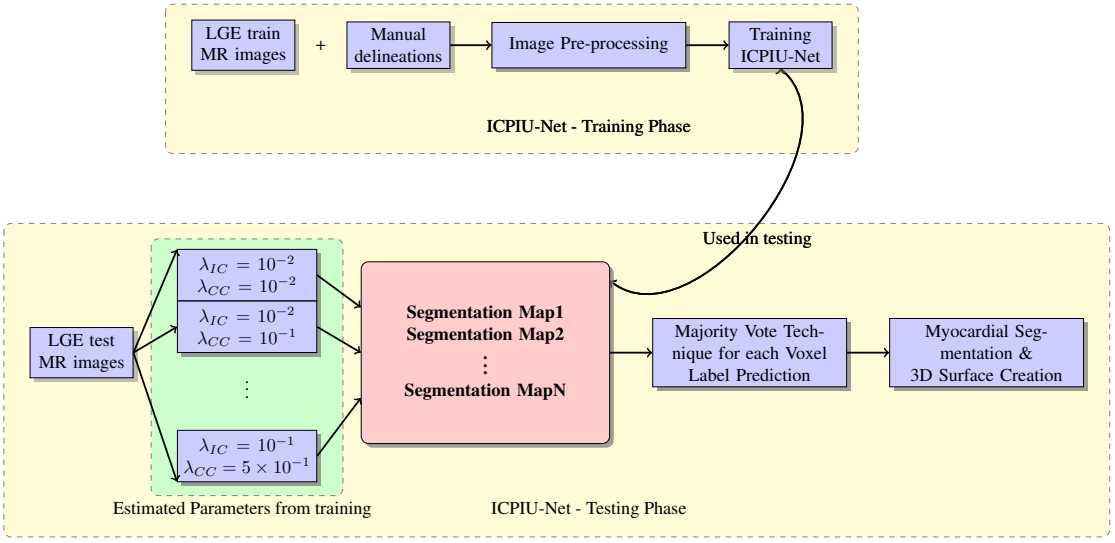

Figure 5.11: Schematic flowchart of ICPIU-Net approach.

challenge in the biomedical field. nnU-Net proved high-quality configurations on a wide diversity of datasets and target image properties [214]. Similar to U-Net, a stack of convolutional layers between poolings in the down-sampling path and of deconvolution operations in the upsampling path is used. Nevertheless, it replaced ReLUs activation functions with leaky ReLUs (leakiness = 10^{-2}) and used instance normalization [87] instead of BN [58]. The operations are arranged as follows: convolution - instance norm - leaky ReLUs. The downsampling is done using strided convolutions rather than max-pooling. nnU-Net ensembles 2D U-Net and 3D U-Net architectures. 2D U-Net trained whole slices to focus on intra-slice information. 3D U-Net is used to learn volumetric spatial features. Therefore, the cross-validation outputs automatically yield to the best-obtained ensemble to be used for the testing prediction.

The proposed anatomical network used 2D, 3D, and cascaded U-Net to overcome the practical shortcoming of a 3D U-Net network on datasets with huge-size images. In a cascaded U-Net architecture, we first trained a 3D U-Net on 3D downsampled images for a preliminary segmentation. The segmentation outputs are then upsampled to the original resolution and transferred to a second 3D U-Net architecture, trained on patches at full resolution for final anatomical segmentation.

The anatomical network has been implemented using the Pytorch source code [1] based on the nnU-Net architecture. To train our approach, we used a five-fold cross-validation and Adam optimizer with an initial learning rate of 3×10^{-4}. The learning rate is decreased over the training process using a polynomial learning rate scheduler. The SA slice and volume inputs are provided for both 2D and 3D U-Nets, respectively. The sum of the Cross-entropy loss (L_{CE}) and the Dice loss (L_{DICE}) is applied to train the proposed anatomical network, as the final loss function (Eq. 5.4).

$$L = L_{CE} + L_{DICE} \tag{5.4}$$

The L_{DICE} loss function is defined as follows:

$$L_{DICE} = -\frac{2}{|K|}\sum_{k\in K}\frac{\sum_{i\in I} u_i^k v_i^k}{\sum_{i\in I} u_i^k + \sum_{i\in I} v_i^k} \tag{5.5}$$

where u represents the softmax output of the proposed anatomical network and v refers to the one-hot encoding of the gold standard delineation drawn manually by the experts. Both u and v have shape $I \times K$ with $i \in I$ indicates the pixels' number in the training patch/batch and $k \in K$ denotes the different categories.

5.3.3.2/ Pathological Network

Our last pathological network extended and modified the pathological framework of SPIU-Net, integrating more prior knowledge for better segmentation performance. The training process took a total time of 314 mins for 200.000 iterations. As shown in Figure 5.12, we incorporated the inclusion (IC in cyan) and class constraints (CC in purple) modules, linked as an extended framework and to the bottom of the 3D U-Net architecture respectively, to improve the final prediction of myocardial disease segmentation. These constraints are proposed as auxiliary L_{IC} and L_{CC} loss terms for highlighting small categories tissue to aid the segmentation.

We trained the proposed 3D CVAE using an iterative optimization process with manual

[1] Source:https://github.com/MIC-DKFZ/nnunethttps://github.com/MIC-DKFZ/nnunet

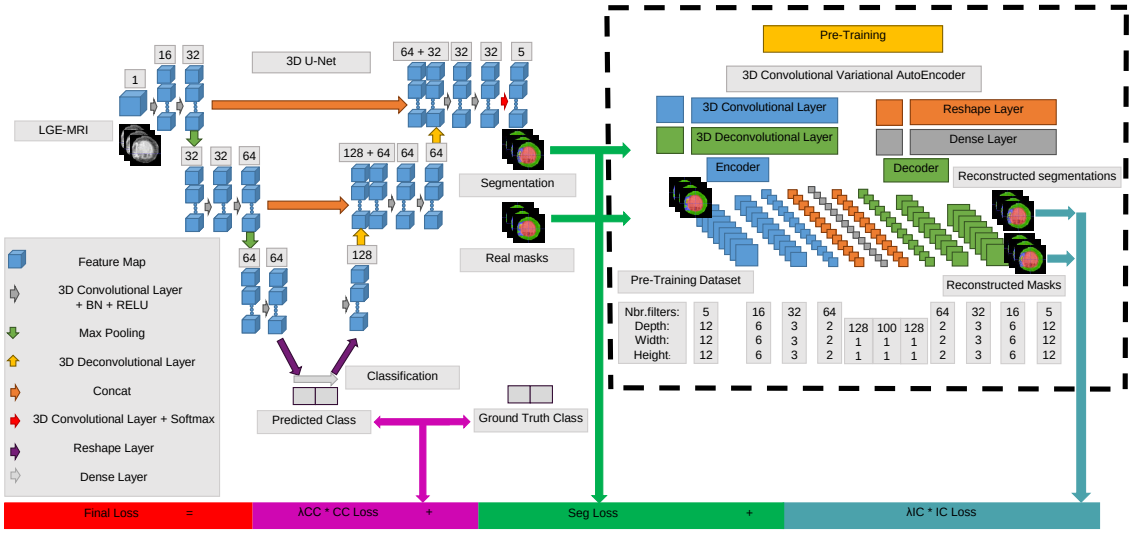

Figure 5.12: Schematic representation of the proposed pathological segmentation network. Both inclusion and class constraints are used to better supervise diseased myocardial segmentation.

delineations to represent anatomically plausible shapes with inclusion constraint segmentation. A pre-trained 3D CVAE on several input cardiac shapes is used as a constraint to transform a segmentation output into a correct shape [186]. The 3D pre-trained CVAE has in-depth knowledge about segmenting different feature representations' tissues. Compared to [186], our proposed 3D CVAE learned the myocardial shape as well as the inclusion of the MVO region into the scar itself into the MYO. The inclusion criteria yielded plausible reconstruction with accurate localization of the cardiac tissues' contours. The schematic representation of the proposed 3D CVAE architecture can be seen in Figure 5.12.

We also proposed a binary classification module to differentiate infarcted subjects from healthy cases. The proposed is introduced in the pathology segmentation process for constraining the predicted label in this known class.

Optimizing the appropriate loss function for accurate segmentation is critical in the training process, especially to alleviate the class imbalance issue. To this end, we trained our pathological network with a fusion of multi-class IOU loss L_{Seg} [168], inclusion constraint loss L_{IC}, and a classification constraint loss L_{CC}. This final loss function is summarized in Eq. 5.6.

$$L_{Final} = L_{Seg} + \lambda_{IC} \times L_{IC} + \lambda_{CC} \times L_{CC} \tag{5.6}$$

where λ_{IC} represents the inclusion constraint penalty-term, L_{IC} denotes the L2 loss function which is defined in Frobenius norm (Eq. 5.7), λ_{CC} indicates the class constraint

penalty-term and L_{CC} is the cross-entropy loss function. We regulate with λ_{IC} and λ_{CC} weights in the gap $[10^{-2}, 10^{-1}]$.

$$L_{IC} = \sum_{i=1}^{n} \|RP_i - RG_i\|_F^2 \tag{5.7}$$

where n indicates the total number of training data, RG_i designates the reconstructed manual contouring, RP_i denotes the reconstructed segmentation output and $\|.\|_F$ represents the Frobenius norm of an $m \times n$ matrix.

The multiclass L_{Seg} loss function computes the overlap between two samples [122] and is integrated into the pathological framework as follows:

$$L_{Seg} = L_{IoU} = \frac{1}{|C|} \sum_{c \in C} \frac{\sum_i p_{ic} \times p_{ic}^*}{\sum_i p_{ic} + p_{ic}^* - p_{ic} \times p_{ic}^*} \tag{5.8}$$

where p_{ic} denotes the prediction score at position i for class c, and p_{ic}^* represents the ground truth distribution being a delta function at yi^*, the true label.

5.4/ CONCLUSION

This chapter proposes three accurate myocardial segmentation models based on a U-Net architecture with introduced blocks. The next chapter focuses on results and extensive experiments on the EMIDEC dataset performed using the proposed networks to assess their efficiency to segment the whole myocardium.

6

Experimental Results and Discussion

This chapter outlines the outputs of each segmentation algorithm depicted in chapter 5 to the expert references of EMIDEC datasets. Each algorithm segmentation output is assessed with standard evaluation metrics introduced in chapter 3.

6.1/ Finding the Best Model

Quantifying pathological regions in the LV may have significant clinical involvements. This work proposes an evaluation framework for several methods that segment and quantify myocardial areas. To evaluate how our approaches handled the MYO and diseased regions, we compare their outputs against several network's outputs, submitted to respond to the EMIDEC challenge, and a reference standard annotation.

6.2/ Network Performance

In summary, in this section, we assessed the performance of three novel DL methods which have been proposed for automatic myocardial segmentation, as described in chapter 5.

6.2.1/ Experiment One - SegU-Net Segmentation

6.2.1.1/ Accuracy of Intra-observer Manual Myocardial Delineation

The first proposal is achieved before the EMIDEC dataset has been publicly available. Intra-observer variability of manual segmentation of both healthy and diseased myocardial contours in LGE-MRI is necessary to establish a gold standard for clinical diagnosing

and the assessment of automatic segmentation methods. To assess, intra-observer variability, a subset of cases (in total, nc = 35 exams, ns = 210 slices) was fully re-contoured by the same expert. The agreements of the intra-observer for myocardial manual delineations in terms of IOU, Accuracy, and DSC metrics, are summarized in Table 6.1, showing the relevance of an expert observer's manual masks to evaluate the myocardial segmentation approaches. For all considered metrics, estimation of BG, healthy and diseased myocardial regions were consistently efficient for reference two when compared against reference one (intra-observer DSC scores varied from "0.67561" to "0.99836" and Accuracy from "0.74108" to "0.99842").

Table 6.1: Metrics comparing intra-observer manual myocardial correlations.

Local measures	BG	MYO	MI	MVO
IOU	0.99665	0.67385	0.50625	0.57868
Accuracy	0.99842	0.77974	0.74108	0.92347
DSC	0.99836	0.80834	0.67561	0.71602

6.2.1.2/ Evaluation Results of SegU-Net Methodology

In this study, a 2.5D SegU-Net has been trained to perform accurate automatic segmentation of infarcted subjects. Qualitative and quantitative evaluations were performed. Representative examples of the masks produced by the intra-observer manual segmentation and the output from the proposed network for test data are visualized in Figure 6.1. The experimental result shows that the automated approach yielded good segmentation of myocardium tissue. As compared to the intra-observer ground truths, the proposed SegU-Net model can also accurately detect myocardial diseased areas.

Table 6.2 and Table 6.3 demonstrate the agreement between the proposed automated segmentation and intra-observer manual masks in identifying myocardial contouring using IOU, Accuracy, and DSC comparison metrics. These performance metrics have been measured on base, middle, and apex slices. For considered metrics, our proposed network achieved better scores against the intra-observer study. The extensive validation of our algorithm turns this proposal into an efficient tool with clinical transfer potential.

Table 6.2: Results. Final SegU-Net values % First intra-observer manual segmentation.

Local measures	BG	MYO	MI	MVO
IOU	0.99998	0.98960	0.91808	0.58423
Accuracy	0.99999	0.99805	0.96945	0.90470
DSC	0.99999	0.99478	0.95729	0.73755

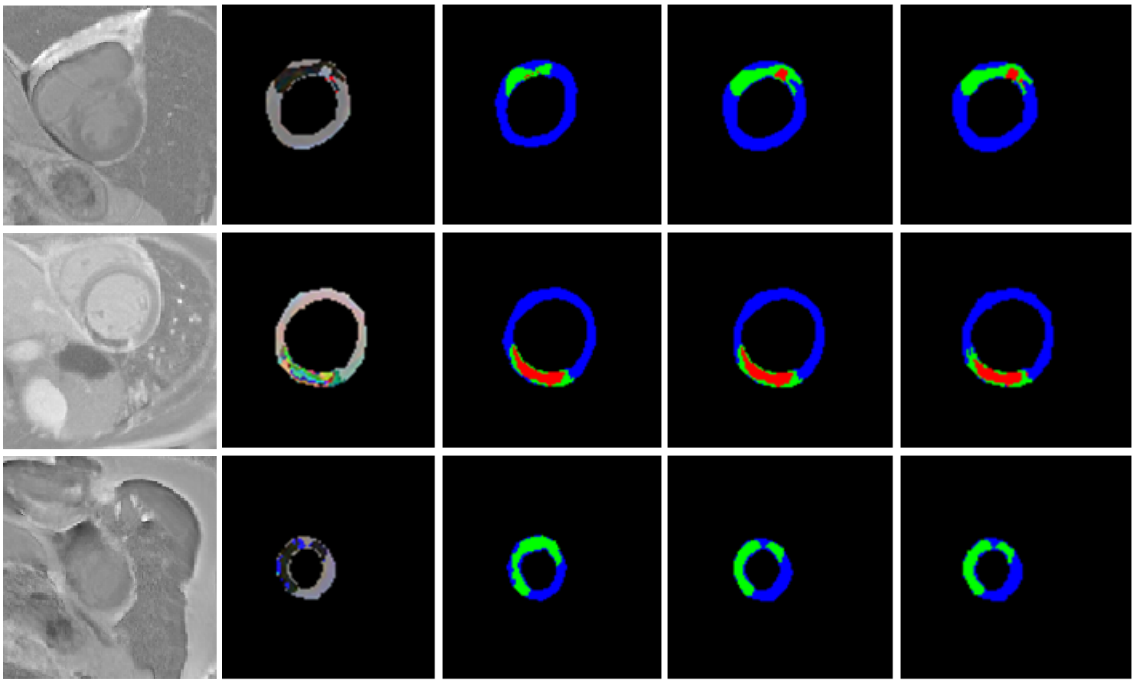

(a) (b) (c) (d) (e)

Figure 6.1: Representative three slices from three test input cases and relative masks. From left to right : (a) Original LGE-MRI , (b) 2.5D Input images, (c) First intra manual segmentation, (d) Second intra manual segmentation, and (e) 2.5D SegU-Net generated-result. (MYO (blue), MI (green), and MVO (red)).

Table 6.3: Results. Final SegU-Net values % Second intra-observer manual segmentation.

Local measures	BG	MYO	MI	MVO
IOU	0.99998	0.98874	0.91547	0.64371
Accuracy	0.99999	0.99873	0.96273	0.91972
DSC	0.99999	0.99434	0.95587	0.78324

Table 6.4 and Table 6.5 illustrate that SegU-Net network with focal-jaccard loss function combination achieved the best trade-off between considered evaluation metrics agreeing with manually segmented test data. Promising results performed through adding the Focal loss[102] function show the relevance of SegU-Net model in detecting diseased myocardial areas.

To analyse the impact of the loss function f summarized in Eq. 6.1, segmentation results obtained from training our SegU-Net with several α and β values were compared with the expert annotations by using precision, recall, F1-score, and IOU metrics. These values settle the degree of penalties for FNs and FPs, respectively. Table 6.6 reports the performance metrics (on the test data sets). For all considered test measures, the best results were achieved using the SegU-Net model trained with IOU loss function

Table 6.4: Results. SegU-Net values % Second intra-expert delineation (Loss Function = Categorical focal-jaccard Loss).

Local measures	BG	MYO	MI	MVO
IOU	0.99998	0.98704	0.91076	0.62415
Accuracy	0.99998	0.99898	0.95962	0.90499
DSC	0.99999	0.99348	0.95329	0.76858

Table 6.5: Results. SegU-Net values % Second intra-expert delineation (Loss Function = Categorical focal-dice loss.

Local measures	BG	MYO	MI	MVO
IOU	0.99996	0.97121	0.81029	0.37830
Accuracy	0.99996	0.99110	0.93513	0.86170
DSC	0.99998	0.98539	0.89520	0.54893

($\alpha = \beta = 1.0$) performing much better than the SegU-Net trained with the dice loss function corresponding to $\alpha = \beta = 0.5$ and other combinations of F-scores ($\alpha + \beta = 1.0$). We also show how adjusting the hyperparameters of IOU performs highly with imbalanced data.

$$f = \frac{TP + smooth}{TP + \alpha \times FN + \beta \times FP + smooth} \tag{6.1}$$

where smooth = 1e-5 and TP, FP, FN: were the abbreviations of True Positive, False Positive, and False Negative, respectively.

Table 6.6: Comparative study of the MYO on the test set conducted for several values of the hyperparameters α and β used in training the SegU-Net.

Average test	Precision	Recall	F1 score	IOU
$\alpha = \beta = 1.0$	**0.99987**	**0.99979**	**0.99982**	**0.95607**
$\alpha = \beta = 0.5$	0.99969	0.99955	0.99959	0.92662
$\alpha = 0.4$, $\beta = 0.6$	0.99935	0.99917	0.99921	0.94996
$\alpha = 0.3$, $\beta = 0.7$	0.98725	0.98806	0.98657	0.60654
$\alpha = 0.7$, $\beta = 0.3$	0.99124	0.99444	0.99252	0.89903
$\alpha = 0.6$, $\beta = 0.4$	0.98967	0.98868	0.98719	0.63285

Our algorithm predicted 52 out of 53 LGE-MRI slices presenting MVO areas when compared against the second expert reference annotation. However, as the disease might not cover the complete LGE-MRI slices, the decision at the infarcted subject diagnostic is determined based on one slice at least being predicted as MI. Representations slice-by-slice for each subject are shown in Figure 6.2. It can be seen that 33 of 33 have been predicted as infarcted patients with an accuracy of 100%, and 18 of 17 have been

predicted as MVO infected with an accuracy of 94,44%. TP = 17 and FP = 1 are the respective numbers of patients with MVO areas segmented correctly and of cases with only MI predicted as cases with MVO tissue.

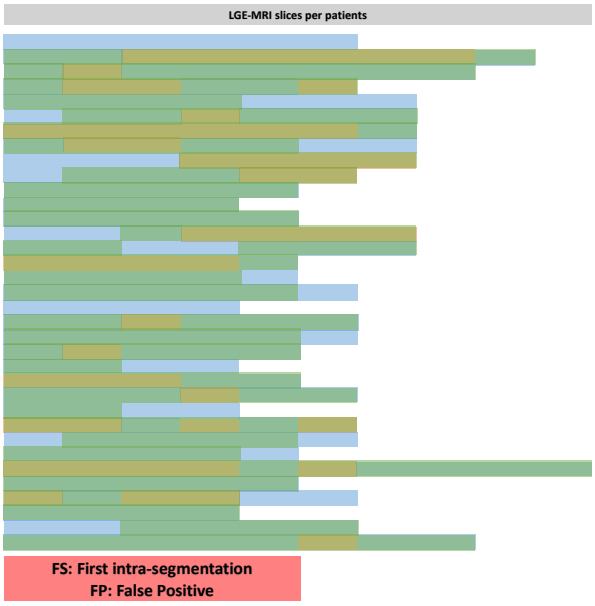

Patients	MVO slice count	Predicted as MVO	MI slice count	Predicted as MI
Patient1	0/0	False	0/0	False
Patient2	6/8	True	9/9	True
Patient3	1/1	True	8/8	True
Patient4	3/3	True	6/6	True
Patient5	0/0	False	4/4	True
Patient6	1/3	True	6/6	True
Patient7	6/6	True	7/7	True
Patient8	2/1(2/3(%FS))	True	5/5	True
Patient9	4/4	True	4/4	True
Patient10	2/0 (noise)	True (FP)	5/5	True
Patient11	0/0	False	5/5	True
Patient12	0/0	False	4/4	True
Patient13	0/0	False	5/5	True
Patient14	4/4	True	5/5	True
Patient15	0/0	False	5/5	True
Patient16	4/4	True	5/5	True
Patient17	0/0	False	4/4	True
Patient18	0/0	False	5/5	True
Patient19	0/0	False	0/0	False
Patient20	1/1	True	6/6	True
Patient21	0/0	False	5/5	True
Patient22	1/1	True	5/5	True
Patient23	0/0	False	2/2	True
Patient24	3/3	True	5/5	True
Patient25	1/1	True	6/6	True
Patient26	0/0	False	2/2	True
Patient27	4/3	True	6/6	True
Patient28	0/0	False	4/4	True
Patient29	0/0	False	4/4	True
Patient30	5/5	True	10/10	True
Patient31	0/0	False	5/5	True
Patient32	3/3	True	4/4	True
Patient33	0/0	False	4/4	True
Patient34	0/0	False	4/4	True
Patient35	1/2	True	8/8	True

Figure 6.2: A conductive report showing for each test patient the total number of slices presenting scar (green) and MVO (orange) regions compared to healthy MYO (blue). For each ratio, the numerator and the denominator represent the total number of slices with MI or MVO per case predicted by our proposed algorithm and manually segmented by an expert, respectively.

Figure 6.3 and Figure 6.4 provide a comparison of the automated method to manual delineation. The detailed boxplot results show that our method segmentation reached accurate similarity to expert ground truth using DSC and IOU evaluation metrics.

6.2.1.3/ Comparison Study with Related Work

We compared the proposed SegU-Net segmentation results with seven previous methods to assess its performance. Summary of the quantitative results presented in Table 6.7 demonstrates that our proposal performed better for all the three evaluation metrics: IOU, Accuracy, and DSC.

6.2.1.4/ Validation of the Performance of SegU-Net on A Benchmark Dataset

To further validate our approaches' performance under another clinical dataset, Table 6.8 shows its accuracy on the MS-CMRSeg dataset (see section 4.4.6), achieving a DSC

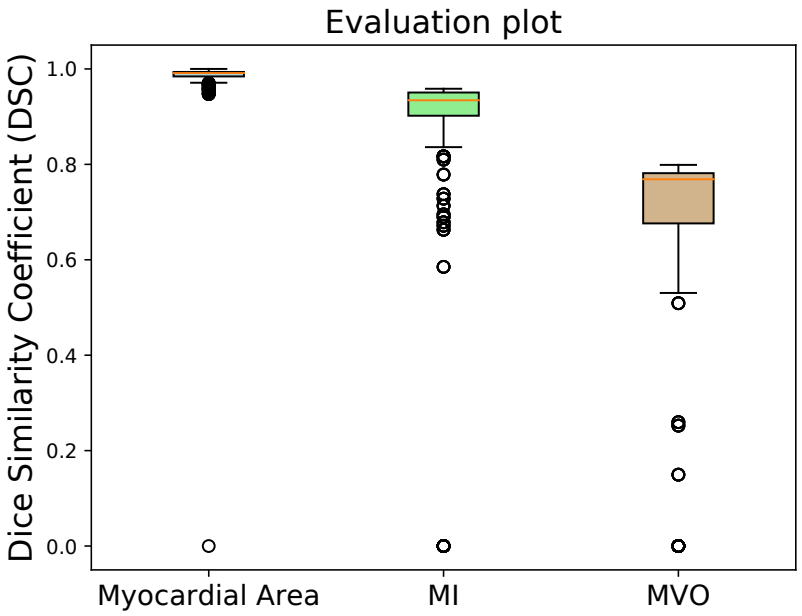

Figure 6.3: Boxplots of the evaluation of DSC for the final SegU-Net algorithm.

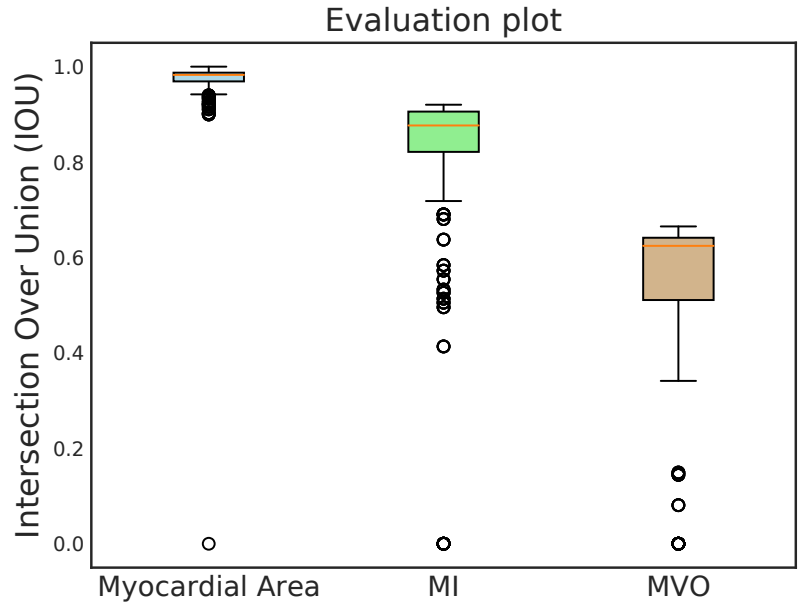

Figure 6.4: Boxplots of the evaluation of IOU for the final SegU-Net algorithm.

score of “0.8594” in MYO. In addition, the experiments demonstrated that the proposed automated model accurately segmented LV and RV regions.

Table 6.7: Quantitative evaluation for myocardial segmentation methods.

Methods	Metrics	Structures			
		BG	MYO	MI	MVO
SegU-Net	IOU	**0.99998**	**0.98874**	**0.91547**	**0.64371**
	Accuracy	**0.99999**	**0.99873**	**0.96273**	**0.91972**
	DSC	**0.99999**	**0.99434**	**0.95587**	**0.78324**
[96]	IOU	0.99984	0.95443	0.73963	0.31258
	Accuracy	0.99989	0.99467	0.85563	0.82690
	DSC	0.99992	0.97668	0.85033	0.47628
[64]	IOU	0.99737	0.74302	0.19792	0.00459
	Accuracy	0.99861	0.90564	0.41232	0.74867
	DSC	0.99868	0.85257	0.33044	0.00913
[135]	IOU	0.99257	0.80819	0.20069	0.0000
	Accuracy	0.99262	0.92750	0.91291	0.74762
	DSC	0.99627	0.89392	0.33429	0.0000
[157]	IOU	0.99761	0.82020	0.11265	0.0000
	Accuracy	0.99963	0.91314	0.33900	0.74762
	DSC	0.99881	0.90122	0.20249	0.0000
[72]	IOU	0.99980	0.80202	0.0000	0.0000
	Accuracy	0.99996	0.99254	0.21429	0.74762
	DSC	0.99990	0.89014	0.0000	0.0000
[81]	IOU	0.99956	0.77503	0.0000	0.0000
	Accuracy	0.99993	0.96345	0.21429	0.74762
	DSC	0.99978	0.87326	0.0000	0.0000
[153]	IOU	0.99030	0.27225	0.0000	0.0000
	Accuracy	0.99824	0.31130	0.21905	0.77619
	DSC	0.99513	0.42799	0.0000	0.0000

Table 6.8: Results. SegU-Net values on MS-CMRSeg dataset.

Local measures	MYO	LV	RV
IOU	0.75360	0.78380	0.94241
Accuracy	0.80848	0.95228	0.93370
DSC	0.85949	0.87880	0.97035

6.2.2/ Experiment Two - SPIU-Net Segmentation

6.2.2.1/ Segmentation Performance of SPIU-Net Methodology on EMIDEC Dataset

For SPIU-Net model evaluation, the whole 100 LGE-MRI with published ground truths was randomly split into 5 non-overlapping cross-validation folds. We aggregated the val-

idation sets from 5-fold cross-validation. Table 6.9 and Table 6.10 illustrate our segmentation results on validation sets experiment without using any auxiliary post-processing operations compared with the other two existing methods. The Averages (Avg) and Standard deviations (Std) of the evaluation metrics, presented in Table 6.9 demonstrate the efficiency of the proposed algorithm to segment anatomical structures and pathological tissues on LGE-MRI scans accurately. Quantitatively, the results show the performance of the SPIU-Net network despite the small number of training samples.

Table 6.9: Quantitative myocardial segmentation performance in 5-fold cross-validation.

Targets	Metrics	5-fold cross-validation						
		fold0	fold1	fold2	fold3	fold4	Avg	Std
MYO	DSC (%)	95.27	94.40	95.11	95.23	95.49	95.10	0.37
	AVD (mm^3)	256.81	343.50	247.88	252.19	231.69	266.41	39.46
	HD (mm)	4.41	5.29	4.36	4.06	3.89	4.40	0.48
MI	DSC (%)	74.93	77.85	76.37	76.52	75.02	76.14	1.08
	AVD (mm^3)	342.00	308.69	212.31	176.75	284.81	264.91	61.31
	AVDR (%)	6.82	6.87	4.09	2.99	5.84	5.32	1.54
MVO	DSC (%)	71.60	77.03	77.64	70.60	72.06	73.79	2.94
	AVD (mm^3)	41.06	34.50	60.00	76.31	63.56	55.09	15.28
	AVDR (%)	0.75	0.75	1.10	1.41	1.24	1.05	0.26

Summary of the quantitative results tabulated in Table 6.10 proves that our segmentation results achieved a better consensus with the manual references than the results of the competing networks. It can be observed that myocardial regions were consistently segmented with high DSC and HD.

Table 6.10: Performance comparison of various segmentation networks using 5-fold cross-validation. Bold result values are the best.

Targets	Metrics	Methods		
		[201]	[209]	SPIU-NET
MYO	DSC (%)	81.00	94.40	**95.10**
	AVD (mm^3)	13655.55	6474.38	**266.41**
	HD (mm)	16.72	17.21	**4.40**
MI	DSC (%)	36.08	72.08	**76.14**
	AVD (mm^3)	8980.5	4179.5	**264.91**
	AVDR (%)	7.07	**3.41**	5.32
MVO	DSC (%)	54.15	71.01	**73.79**
	AVD (mm^3)	1501.73	918.69	**55.09**
	AVDR (%)	1.08	**0.69**	1.05

We conducted extensive experiments for a comparative study of different methods based

on wIOU and mwIOU loss functions. The SPIU-Net algorithm is also compared with the baseline 3D U-Net architecture to demonstrate the significance of enforcing shape prior information in the final prediction. Figure 6.5 and Figure 6.6 illustrate plots of DSC, HD, and difference in volume between automated segmentation among all loss functions and expert annotation of the validation data set. Results show that incorporating shape prior in the resulting network made the best trade-off between evaluation metrics. Quantitatively, our approach yielded promising results, achieving an average DSC score of “0.9507”, “0.7656”, and “0.8377” for MYO, scar, and MVO, respectively. It can be seen that our SPIU-Net model outperformed the baseline 3D U-Net architecture (median HD of “3.16 mm” vs. “4.12 mm”).

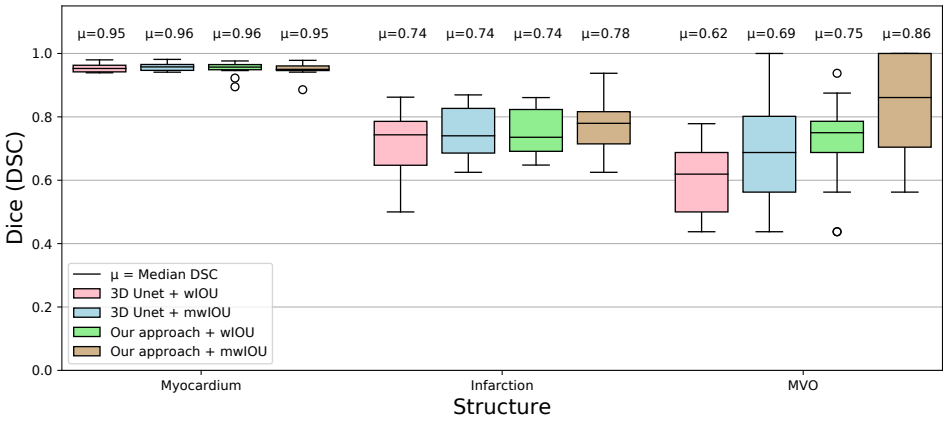

(a) DSC for the MYO, MI, and MVO regions.

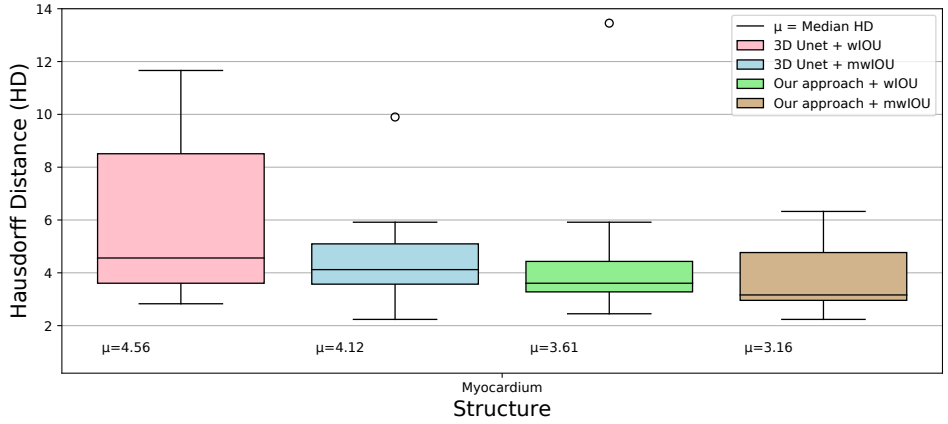

(b) HD (mm) for the diverse segmentation methods.

Figure 6.5: Comparison of the networks results. Our approach outperformed the 3D U-Net architecture in segmenting myocardial areas.

Figure 6.7 shows examples of expert myocardial delineation and corresponding segmentation results of 3D U-Net and the final proposed model in our own split testing set. Our

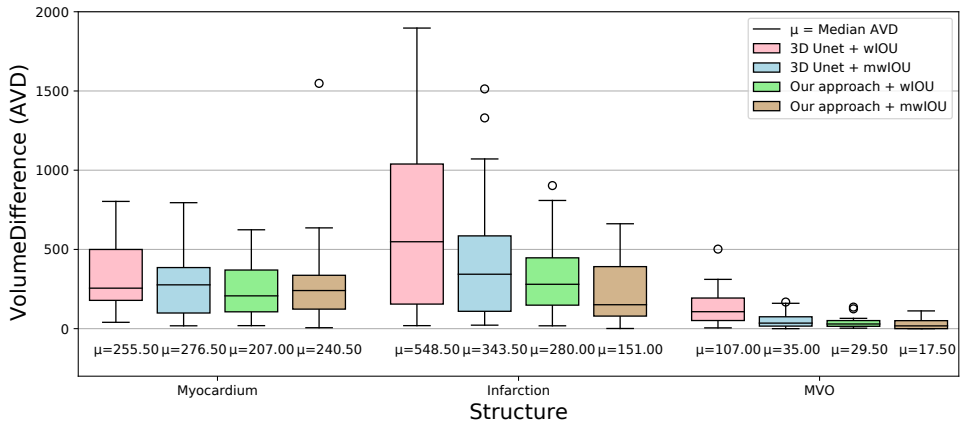

(a) AVD (mm^3) between methods and the expert target.

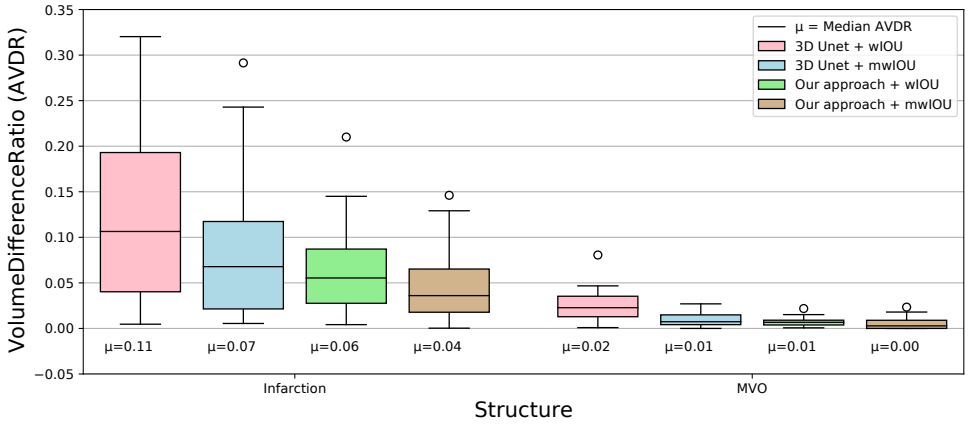

(b) AVDR (%) of MI and MVO in relation to the full myocardial volume.

Figure 6.6: Comparison of segmentation performance. The proposed SPIU-Net model achieves superior AVD and AVDR values on the MI, and MVO areas.

segmentation results appear to be in line with the ground truth. Two axial slice views and a 3D surface rendering with expert annotation are shown in the first row. Segmented images produced by our proposed algorithm and 3D U-Net architecture are illustrated in the corresponding row. Compared to ground truths, our approach correctly segmented myocardial regions yielding a good agreement with expert annotations. Qualitative results comparison demonstrate the efficiency of the SPIU-Net model to improve segmentation performance.

Table 6.11 demonstrates how the incorporation of the pathological network, which is responsible for detecting the diseased tissues, affects the segmentation performance of the MYO and LV cavity structures produced by the anatomical network. The table quantitatively shows the anatomical segmentation network's performances alone and after integrating the shape prior auxiliary model into it.

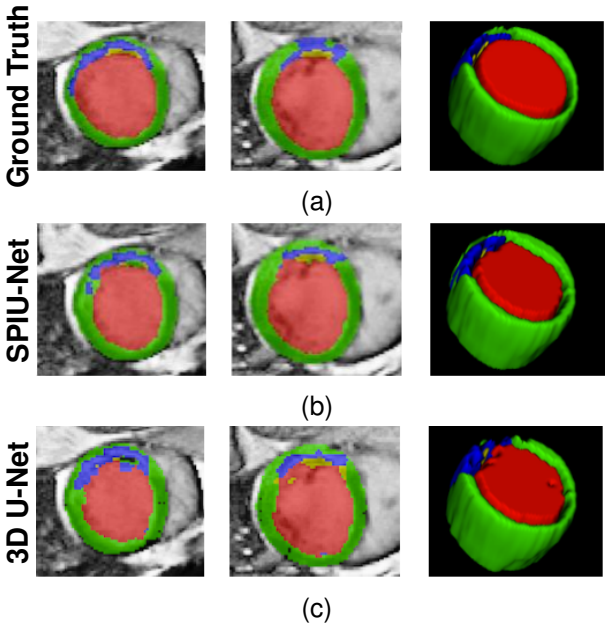

Figure 6.7: Visual exemplar segmentations for our SPIU-Net model and 3D U-Net applied for the same subject on our own split testing set. Each row displays a patient on two heart locations, followed by a 3D surface rendering. The rows from top to bottom are the expert delineation, our approach prediction, and 3D U-Net segmentation. LV cavity, MYO, scar, and MVO are labeled in red, green, blue, and yellow, respectively.

Table 6.11: Performance analysis and comparison between the proposed anatomical model and our final SPIU-NET network (anatomical + pathological) without and with using post-processing. An example is presented for one fold as 5 fold-cross validation is done.

Targets	Metrics	Methods		
		Anatomical model	Without post-processing	**SPIU-NET**
MYO	DSC (%)	91.18	95.27	95.07
	AVD (mm^3)	348.62	256.81	315.5
	HD (mm)	23.65	4.41	5.02
Infarction	DSC (%)	–	74.93	76.56
	AVD (mm^3)	–	342.00	234.12
	AVDR (%)	–	6.82	4.92
MVO	DSC (%)	–	71.60	83.77
	AVD (mm^3)	–	41.06	30.25
	AVDR (%)	–	0.75	0.60

6.2.2.2/ Validation of the Performance of the Proposed Anatomical Network on Benchmark Datasets

To further evaluate the performance of the proposed anatomical model, we tested the proposed anatomical model on other publicly available LGE-MRI datasets using the same op-

timized parameters setting chosen during training with the EMIDEC dataset. The data has been preprocessed based on the multivariate mixture method (MvMM) [155]. Table 6.12 and Table 6.13 illustrate the performance comparison of the proposed anatomical with state-of-the-art networks on MS-CMRSeg and MyoPS challenges, respectively. These tables show that our anatomical approach achieved excellent DSC scores as compared to previous methods. The experiments prove the efficiency of our proposed anatomical network on other clinical datasets.

Table 6.12: Performance analysis and comparison of myocardial results of the proposed anatomical network and existing DL-based networks on MS-CMRSeg database. (DSC (%) and HD (mm)). Best results are highlighted in bold font.

Methods	Dataset	DSC	HD
Proposed Anatomical model	BSSFP+ T1 for training LGE	**81.87**	**9.98**
[184]	Used different combination for training LGE	74.90	11.35
[158]	Used different combination for training LGE	68.00	12.00

Table 6.13: Performance analysis and comparison of myocardial results of the proposed anatomical network and existing DL-based networks on MyoPS database. Best results are highlighted in bold font.

Methods	DSC (%)	HD (mm)	AVD (ml)
Proposed anatomical model	**84.69**	**16.3190**	8.6275
[200]	82.17	17.9299	**7.3824**
[179]	80.05	23.2728	11.6204
[64]	0.7956	114.7892	26.3757

6.2.3/ Experiment Three - ICPIU-Net Segmentation

The trained ICPIU-Net model was used to predict myocardial segmentation for each of the test volumes. We compared the segmentation results of our approach to other existing networks reported in section 4.3.2.2. We also compared the ICPIU-Net prediction results to ground truths and [211], which only enforces a shape prior information for segmenting damaged myocardial tissues. Both qualitative and quantitative results are described below.

Figure 6.8 illustrates the MYO, scar, and MVO segmentation results of our proposed ICPIU-Net and [211] for three diverse slices, randomly selected from three different subjects of the testing dataset. Segmented 2D slices were stacked up to reconstruct a 3D rendering surface of myocardial tissues. Compared to [211], the ICPIU-Net model segmented infarct and MVO more accurately. Qualitative results show that the final segmen-

tation narrowly matched the expert annotation for all the labeled areas.

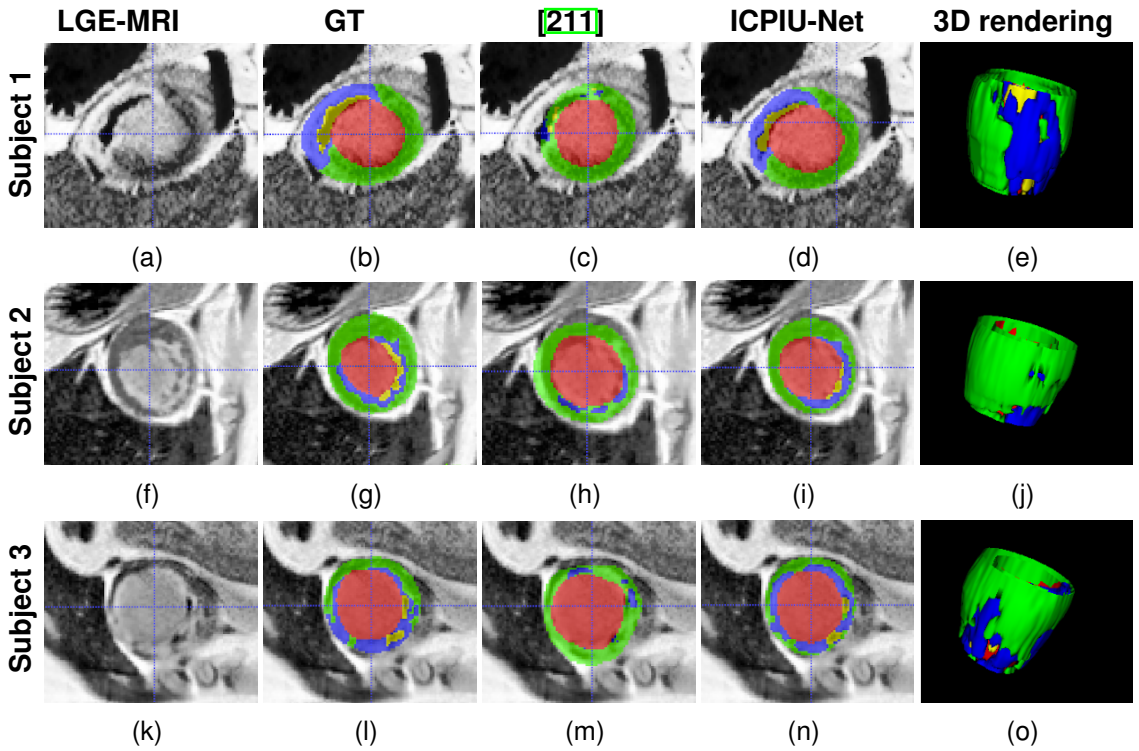

Figure 6.8: Qualitative segmentation results. In the first fourth columns, input LGE-MRI, manually segmented contours, and examples of the segmentation results on three various slices extracted from LGE-MRI of three testing subjects produced by [211] network and the proposed ICPIU-Net model are displayed. The fifth column illustrates the 3D view of the myocardial tissues of our proposed method prediction. Red: LV cavity, Green: MYO, Blue: Scar, and Yellow: MVO.

Figure 6.9 shows examples of the segmentation results of proposed model and expert delineations at basal, mid-ventricular, and apical slices. With the incorporation of the additional inclusion and classification constraints, the segmentation results reached a good consensus with the ground truths. Qualitative evaluations prove that our approach produced more robust segmentation results, especially at the middle slices. It can be observed that most segmentation errors appear at basal and apical slices.

Bland–Altman plots of the proposed ICPIU-Net model vs. expert manual LV volumes are provided in Figure 6.10. In these graphs, the dashed blue line and red dashed lines illustrate the mean value of the difference, the upper and lower limits of accordance, respectively. Compared to expert annotations, our model's mean bias in evaluating MYO, infarct, and MVO volumes was "4.9888 cm^3", "1.2266 cm^3", and "0.5112 cm^3", respectively. The proposed ICPIU-Net network lightly overvalued myocardial region volumes producing a mean absolute LV volume error of "8.12%". In addition, a case-by-case study of our approach's generated segmentation demonstrated that the MI area could be accurately detected in 32 out of 33 pathological patients from the test dataset. The results

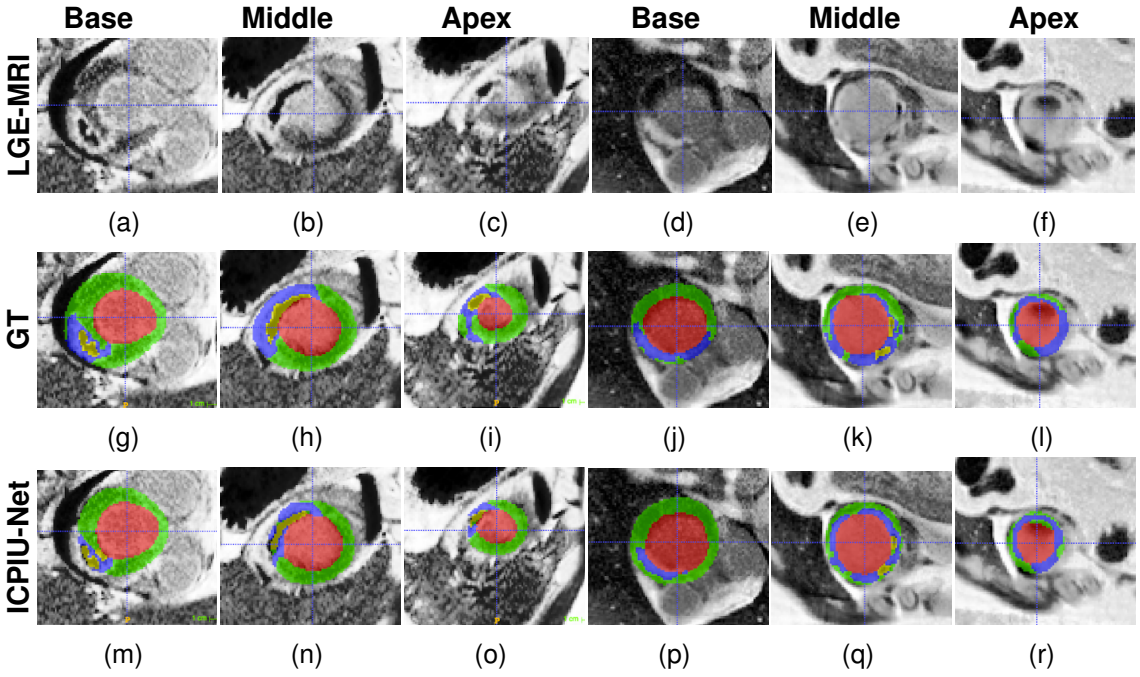

Figure 6.9: Examples of myocardial test segmentation compare results and the gold standard for three levels (base, middle, and apex) of two subject slices (columns 1-3 from subject 1 and columns 4-6 from subject 2). The proposed model is capable of segmenting the MYO while also identifying the small diseased areas. LV cavity is displayed in red, MYO in green, MI in blue, and MVO in Yellow.

prove the superiority of the ICPIU-Net network and the efficiency of each incorporated constraint information.

Table 6.14 outlines the quantitative results of our approach against state-of-the-art models on EMIDEC challenge for the testing dataset. Our proposed algorithm outperformed top-ranked frameworks achieving the best DSC, AVD, and AVDR results for diseased tissues segmentations. The second best DSC score was attained using [209] ("71.24%" for MI and "78.51%" for MVO). Our proposed model also yielded much better results in all metrics than several competing methods (DSC, AVD, and HD of "87.65%", "8863.41 mm^3", and "13.10 mm", respectively). The significant correlation between expert annotation and the proposed network demonstrated our approach's performance and clinical applicability for the automatic assessment of MI.

We conducted a comparative ablation study to assess the effect of adding prior constraint information to the segmentation loss. As can be seen from Table 6.15, the introducing of IC and CC regularization penalty terms into the baseline 3D U-Net improved the segmentation accuracy and thus provided more plausible segmentation close to the expert annotation. The experimental results revealed the pertinence of constraints modules to aid the myocardial segmentation.

The evaluation metrics (DSC, AVD, and AVDR) used for MVO segmentations may be in-

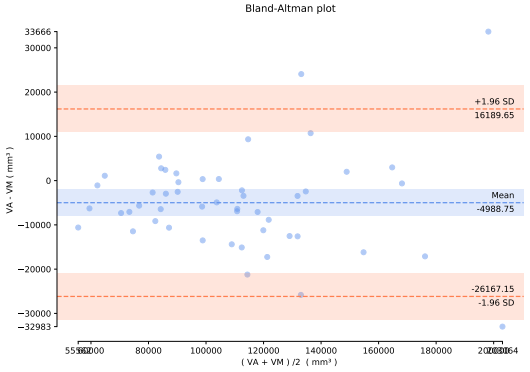

(a)

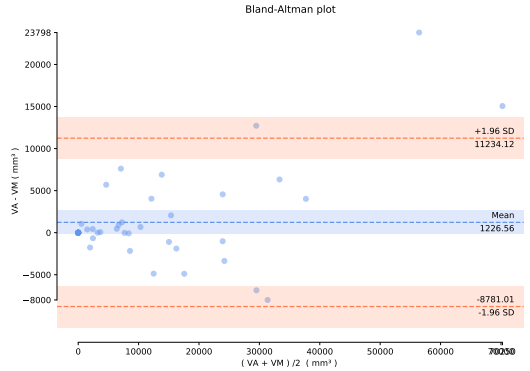

(b)

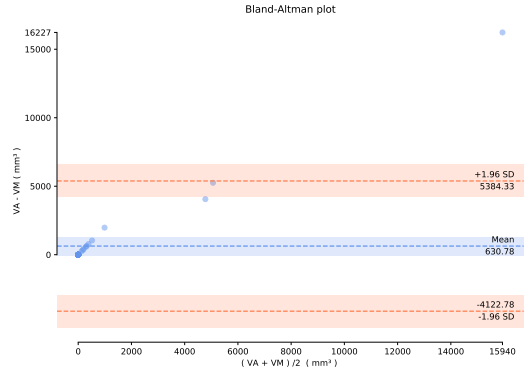

(c)

Figure 6.10: The graph shows the difference between the resulting network and ground truth volumes according to their average. (a), (b), and (c): Representative Bland-Altman plots of MYO, MI, and MVO volumes obtained from our ICPIU-Net model over testing examples, respectively.

consistent due to the small area of the MVO compared to the complete input LGE-MRI. MVO absence on all the data may apparently provide correct results with DSC and vol-

Table 6.14: Comparative study for EMIDEC segmentation results [215]. (DSC (%), HD (mm), AVD (mm^3), and AVDR (%)).Significant results are marked in bold font.

Methods	Structures								
	MYO			MI			MVO		
	DSC	AVD	HD	DSC	AVD	AVDR	DSC	AVD	AVDR
[198]	83.56	15187.48	33.77	54.68	3970.73	2.89	72.22	883.42	0.53
[201]	84.08	10874.47	18.3	37.87	6166.01	4.93	52.25	953.47	0.64
[208]	85.53	16539.52	13.23	62.79	5343.69	4.37	60.99	1851.52	1.69
[209]	**87.86**	9258.24	**13.01**	71.24	3117.88	2.38	78.51	634.69	0.38
[193]	75.74	17108.13	25.44	30.79	4868.56	3.64	60.52	867.86	0.52
[210]	82.46	13292.68	83.42	37.77	6104.99	4.71	51.98	879.99	0.54
[199]	80.26	11807.68	51.48	34.00	11521.71	8.58	78.00	891.13	0.51
[64]	85.82	11368.04	14.23	58.30	3380.43	2.57	74.97	626.33	0.38
[70]	87.77	9454.43	13.07	70.76	3214.65	2.48	78.90	540.95	0.34
ICPIU-NET	87.65	**8863.41**	13.10	**73.36**	**2693.84**	**1.95**	**81.31**	**511.25**	**0.32**

Table 6.15: Performance metrics for various values of training hyperparameters λ_{IC} and λ_{CC}. (DSC (%), HD (mm), AVD (mm^3), and AVDR (%)). Significant results are marked in bold font.

Hyperparameters	Structures								
	MYO			MI			MVO		
	DSC	AVD	HD	DSC	AVD	AVDR	DSC	AVD	AVDR
$\lambda_{IC} = \lambda_{CC} = 0$	**87.77**	9381.77	**13.07**	65.05	3096.54	2.39	78.82	553.56	0.34
$(\lambda_{IC} \neq 0) \wedge (\lambda_{CC} = 0)$	87.74	9201.04	13.09	71.71	2830.32	2.15	80.99	538.60	0.34
ICPIU-NET	87.65	**8863.41**	13.10	**73.36**	**2693.84**	**1.95**	**81.31**	**511.25**	**0.32**

umes metrics. Nevertheless, the accuracy highlights the efficiency of our approach to segmenting MVO tissues. Table 6.16 shows the additional metrics of MVO regions. Segmentation results demonstrate the effectiveness of inclusion and classification constraints in identifying MVO areas.

Table 6.16: Supplementary metrics for myocardial segmentation [215]. Best results are highlighted in bold font.

	Metrics	Methods							
		[198]	[201]	[208]	[209]	[193]	[210]	[199]	**ICPIU-NET**
MVO	Accuracy (case,%)	80.00	70.00	76.00	**84.00**	74.00	64.00	78.00	**84.00**
	Accuracy (slice,%)	90.78	85.75	81.56	**94.97**	84.36	86.87	89.66	**94.97**

6.3/ CONCLUSION

This chapter compares the segmentation results of three proposed networks, presented in chapter 5, against expert annotated delineation and some other methods on the 50 test sets. Experimental results on the EMIDEC dataset demonstrate that the proposed ICPIU-Net outperforms the state-of-the-art myocardial segmentation networks.

III

CONCLUSION

7

Conclusion and Future Work

"As a technologist, I see how AI and the fourth industrial revolution will impact every aspect of people's lives"

—Fei-Fei Li

7.1/ General Conclusion

Myocardial scar segmentation of CMR is a highly challenging area of research that can afford critical information to aid diagnosis and therapy planning. As the manual segmentation for LV infarct is a time-consuming and observer-biased task, automatic myocardial segmentation using DL techniques has been extensively explored in the last decades to grow the survival rate.

LGE-MRI has emerged as the gold standard for quantifying scar or MVO areas. It relies on the difference in signal intensity between normal myocardial area and infarcted tissue. Studies have proved the feasibility of LGE-MRI to evaluate the viability of the myocardial segment. Promising results were acquired through a gadolinium-based contrast agent, putting into evidence re-perfused areas within the MYO wall as a sign of MI.

In this context, the present dissertation has been realized to develop improved, robust, and fully automated DL-based segmentation networks to assess and quantify pathological tissues within the LV (MI, MVO), including healthy MYO on a set of contrast-enhanced acquisitions. To support this overall purpose, we evaluate their performances on EMIDEC datasets, comprising 100 training images and 50 test images from healthy and infarcted patients, to help cardiologists establish diagnosis and treatment pipelines faster. The methods' assessment and validation were achieved based on different evaluation metrics, including DSC, HD, and AVD. We demonstrated that the segmentation results were consistent with the manual contouring and that our proposed models compared favorably with methods recently developed for the EMIDEC challenge. Extensive experiments on

two other public datasets (MS-CMRSeg, MyoPS) show that our resulting architectures achieved a good performance.

The proposed process first used a pre-processing step on the complete LGE data. Next, the processed LGE-MR images are passed through proposed algorithms to segment normal MYO, infarct, and MVO regions. The framework results are finally post-processed to improve the segmentation accuracy. In the following, we summarize the principal contributions of this thesis.

- We first proposed a 2.5D SegU-Net network based on fusing two DL architectures (U-Net and Seg-Net) for automated LGE-MRI myocardial disease segmentation in a new multifield expert annotated dataset (EMIDEC before being publicly available). We used the combination of the Jaccard loss and the Focal Loss as the final optimization loss function. Compared to the intra-observer variability, the proposed framework perfectly segments diseased myocardial regions of infarcted patients. Our novel segmentation pipeline worked best in comparison with previous models.
- Secondly, we developed an SPIU-Net DL-based shape prior model for automatic MI segmentation from LGE-MRI. Furthermore, the proposed method aimed to detect MVO areas accurately. We first segmented the anatomical structures, i.e., the LV cavity and the MYO, to produce a preliminary segmentation. Then, we proposed to combine 3D U-Net architecture and 3D Autoencoder segmentation network to incorporate shape prior information on the framework pipeline to ensure plausible segmentation of myocardial tissues. Experiments results have demonstrated the algorithm's performance in identifying myocardial areas.
- Finally, an ICPIU-Net segmentation algorithm based on the inclusion and classification priors information was implemented to efficiently segment the normal MYO, scar, and MVO tissues. The proposed method first used nnU-Net architecture to segment the LV cavity and MYO. Then, our approach introduced the inclusion and classification information of the LGE-MRI to improve the resulting segmentation of the diseased tissues within the pre-segmented MYO. Compared to several DL-based models participating in the EMIDEC challenge for MI segmentation, our approach achieved a more significant agreement with the gold standard in segmenting myocardial diseases.

7.2/ FUTURE PERSPECTIVES

Our research on myocardial segmentation in LGE-MRI using prior constrained information opens several perspectives. The proposed networks are envisioned to foresee future

research lines. It would be interesting to extend these algorithms to other modalities and heart conditions or to develop new improvements to the proposed algorithms. Our segmentation methods can be fused with traditional cardiac segmentation techniques to bring an excellent diagnostic package with high reliability. Further works are also needed to impose clinical information, intensity, and transverse sections (basal, middle, and apical) prior knowledge into the segmentation process. An uncertainty rectifying block can be introduced to boost the network performance, where the uncertainty estimation can be generated with a bayesian method. A memory module propagating the initial segmentation over the whole volume can also be incorporated to guide the next slice to segment based on the current segmentation of each slice.

There is still much research work possible to improve MI segmentation. Despite the success of CNNs, the locality of convolution operations limits their ability to learn global context and long-range spatial dependencies. Recently, transformers, developed initially to solve natural language processing tasks, are considered the alternative methods to U-Nets. Nevertheless, they focus only on the global context but fail to extract detailed localization features. Transformers demonstrate outstanding performance in several DL tasks, including image recognition. Nowadays, few studies have used pure transformer and transformer-CNN (UNETR, vision transformer (ViT)) hybrid methods for medical image segmentation and classification. In the future, transformer-based architectures can be applied to EMIDEC dataset for improved segmentation of myocardial diseases.

BIBLIOGRAPHY

[1] YOUNG, I., BAILES, D., AND BYDDER, G. **Apparent changes of appearance of inversion-recovery images**. *Magnetic resonance in medicine 2*, 1 (1985), 81–85.

[2] SCHILLER, N. B., SHAH, P. M., CRAWFORD, M., DEMARIA, A., DEVEREUX, R., FEIGENBAUM, H., GUTGESELL, H., REICHEK, N., SAHN, D., SCHNITTGER, I., AND OTHERS. **Recommendations for quantitation of the left ventricle by two-dimensional echocardiography**. *Journal of the American Society of Echocardiography 2*, 5 (1989), 358–367.

[3] NOLL, D. C., NISHIMURA, D. G., AND MACOVSKI, A. **Homodyne detection in magnetic resonance imaging**. *IEEE transactions on medical imaging 10*, 2 (1991), 154–163.

[4] BELOHLAVEK, M., FOLEY, D. A., GERBER, T. C., KINTER, T. M., GREENLEAF, J. F., AND SEWARD, J. B. **Three-and four-dimensional cardiovascular ultrasound imaging: a new era for echocardiography**. In *Mayo Clinic Proceedings* (1993), vol. 68, Elsevier, pp. 221–240.

[5] ZUIDERVELD, K. **Contrast limited adaptive histogram equalization**. *Graphics gems* (1994), 474–485.

[6] HOCHREITER, S., AND SCHMIDHUBER, J. **Long short-term memory**. *Neural computation 9*, 8 (1997), 1735–1780.

[7] KIM, R. J., FIENO, D. S., PARRISH, T. B., HARRIS, K., CHEN, E.-L., SIMONETTI, O., BUNDY, J., FINN, J. P., KLOCKE, F. J., AND JUDD, R. M. **Relationship of mri delayed contrast enhancement to irreversible injury, infarct age, and contractile function**. *Circulation 100*, 19 (1999), 1992–2002.

[8] QIAN, N. **On the momentum term in gradient descent learning algorithms**. *Neural networks 12*, 1 (1999), 145–151.

[9] SAKUMA, H., TAKEDA, K., AND HIGGINS, C. B. **Fast magnetic resonance imaging of the heart**. *European journal of radiology 29*, 2 (1999), 101–113.

[10] FRANGI, A. F., NIESSEN, W. J., AND VIERGEVER, M. A. **Three-dimensional modeling for functional analysis of cardiac images, a review**. *IEEE transactions on medical imaging 20*, 1 (2001), 2–5.

[11] SIMONETTI, O. P., KIM, R. J., FIENO, D. S., HILLENBRAND, H. B., WU, E., BUNDY, J. M., FINN, J. P., AND JUDD, R. M. **An improved mr imaging technique for the visualization of myocardial infarction**. *Radiology 218*, 1 (2001), 215–223.

[12] JANARDHANAN, R., SWINBURN, J. M., GREAVES, K., AND SENIOR, R. **Usefulness of myocardial contrast echocardiography using low-power continuous imaging early after acute myocardial infarction to predict late functional left ventricular recovery**. *The American journal of cardiology 92*, 5 (2003), 493–497.

[13] MORIN, R. L., GERBER, T. C., AND MCCOLLOUGH, C. H. **Radiation dose in computed tomography of the heart**. *Circulation 107*, 6 (2003), 917–922.

[14] ROPERS, D., BAUM, U., POHLE, K., ANDERS, K., ULZHEIMER, S., OHNESORGE, B., SCHLUNDT, C., BAUTZ, W., DANIEL, W. G., AND ACHENBACH, S. **Detection of coronary artery stenoses with thin-slice multi-detector row spiral computed tomography and multiplanar reconstruction**. *Circulation 107*, 5 (2003), 664–666.

[15] ANDERSON, R. H., RAZAVI, R., AND TAYLOR, A. M. **Cardiac anatomy revisited**. *Journal of anatomy 205*, 3 (2004), 159–177.

[16] WARFIELD, S. K., ZOU, K. H., AND WELLS, W. M. **Simultaneous truth and performance level estimation (staple): an algorithm for the validation of image segmentation**. *IEEE transactions on medical imaging 23*, 7 (2004), 903–921.

[17] BUADES, A., COLL, B., AND MOREL, J.-M. **A non-local algorithm for image denoising**. In *2005 IEEE Computer Society Conference on Computer Vision and Pattern Recognition (CVPR'05)* (2005), vol. 2, IEEE, pp. 60–65.

[18] VOGEL-CLAUSSEN, J., ROCHITTE, C. E., WU, K. C., KAMEL, I. R., FOO, T. K., LIMA, J. A., AND BLUEMKE, D. A. **Delayed enhancement mr imaging: utility in myocardial assessment**. *Radiographics 26*, 3 (2006), 795–810.

[19] YAN, A., SHAYNE, A., BROWN, K., GUPTA, S., CHAN, C., LUU, T., CARLI, M., REYNOLDS, H., STEVENSON, W., AND KWONG, R. **Characterization of the peri-infarct zone by contrast-enhanced cardiac mri is a powerful predictor of post-myocardial infarction mortality**. *Circulation 114*, 1 (2006), 32–39.

[20] YU-QIAN, Z., WEI-HUA, G., ZHEN-CHENG, C., JING-TIAN, T., AND LING-YUN, L. **Medical images edge detection based on mathematical morphology**. In *2005 IEEE engineering in medicine and biology 27th annual conference* (2006), IEEE, pp. 6492–6495.

[21] DOI, K. **Computer-aided diagnosis in medical imaging: historical review, current status and future potential**. *Computerized medical imaging and graphics 31*, 4-5 (2007), 198–211.

[22] DWIVEDI, G., JANARDHANAN, R., HAYAT, S. A., SWINBURN, J. M., AND SENIOR, R. **Prognostic value of myocardial viability detected by myocardial contrast echocardiography early after acute myocardial infarction**. *Journal of the American College of Cardiology 50*, 4 (2007), 327–334.

[23] CIGLA, C., AND ALATAN, A. A. **Region-based image segmentation via graph cuts**. In *2008 15th IEEE International Conference on Image Processing* (2008), IEEE, pp. 2272–2275.

[24] GOLAND, S., CZER, L. S., LUTHRINGER, D., AND SIEGEL, R. J. **A case of arrhythmogenic right ventricular cardiomyopathy**. *Canadian Journal of Cardiology 24*, 1 (2008), 61–62.

[25] JAFFE, R., CHARRON, T., PULEY, G., DICK, A., AND STRAUSS, B. H. **Microvascular obstruction and the no-reflow phenomenon after percutaneous coronary intervention**. *Circulation 117*, 24 (2008), 3152–3156.

[26] POH, K. K., LEVINE, R. A., SOLIS, J., SHEN, L., FLAHERTY, M., KANG, Y.-J., GUERRERO, J. L., AND HUNG, J. **Assessing aortic valve area in aortic stenosis by continuity equation: a novel approach using real-time three-dimensional echocardiography**. *European heart journal 29*, 20 (2008), 2526–2535.

[27] SOMERS, V. K., WHITE, D. P., AMIN, R., ABRAHAM, W. T., COSTA, F., CULEBRAS, A., DANIELS, S., FLORAS, J. S., HUNT, C. E., OLSON, L. J., AND OTHERS. **Sleep apnea and cardiovascular disease: An american heart association/american college of cardiology foundation scientific statement from the american heart association council for high blood pressure research professional education committee, council on clinical cardiology, stroke council, and council on cardiovascular nursing in collaboration with the national heart, lung, and blood institute national center on sleep disorders research (national institutes of health)**. *Journal of the American College of Cardiology 52*, 8 (2008), 686–717.

[28] FUNARO, S., LA TORRE, G., MADONNA, M., GALIUTO, L., SCARA, A., LABBADIA, A., CANALI, E., MATTATELLI, A., FEDELE, F., ALESSANDRINI, F., AND OTHERS. **Incidence, determinants, and prognostic value of reverse left ventricular remodelling after primary percutaneous coronary intervention: results of the acute myocardial infarction contrast imaging (amici) multicenter study**. *European heart journal 30*, 5 (2009), 566–575.

[29] GIRI, S., CHUNG, Y.-C., MERCHANT, A., MIHAI, G., RAJAGOPALAN, S., RAMAN, S. V., AND SIMONETTI, O. P. **T2 quantification for improved detection of myocardial edema**. *Journal of cardiovascular magnetic resonance 11*, 1 (2009), 1–13.

[30] MIKAMI, Y., SAKUMA, H., NAGATA, M., ISHIDA, M., KURITA, T., KOMURO, I., AND ITO, M. **Relation between signal intensity on t2-weighted mr images and presence of microvascular obstruction in patients with acute myocardial infarction**. *American Journal of Roentgenology 193*, 4 (2009), W321–W326.

[31] RADAU, P., LU, Y., CONNELLY, K., PAUL, G., DICK, A., AND WRIGHT, G. **Evaluation framework for algorithms segmenting short axis cardiac mri**. *The MIDAS Journal-Cardiac MR Left Ventricle Segmentation Challenge 49* (2009).

[32] CELEBI, A. S., YALCIN, H., AND YALCIN, F. **Current cardiac imaging techniques for detection of left ventricular mass**. *Cardiovascular ultrasound 8*, 1 (2010), 1–11.

[33] GLOROT, X., AND BENGIO, Y. **Understanding the difficulty of training deep feedforward neural networks**. In *Proceedings of the thirteenth international conference on artificial intelligence and statistics* (2010), JMLR Workshop and Conference Proceedings, pp. 249–256.

[34] NACIF, M. S., OLIVEIRA JUNIOR, A. C. D., CARVALHO, A. C. P., AND ROCHITTE, C. E. **Cardiac magnetic resonance and its anatomical planes: how do i do it?** *Arquivos brasileiros de cardiologia 95* (2010), 756–763.

[35] XU, A., WANG, L., FENG, S., AND QU, Y. **Threshold-based level set method of image segmentation**. In *2010 Third International Conference on Intelligent Networks and Intelligent Systems* (2010), IEEE, pp. 703–706.

[36] DUCHI, J., HAZAN, E., AND SINGER, Y. **Adaptive subgradient methods for online learning and stochastic optimization.** *Journal of machine learning research 12*, 7 (2011).

[37] FONSECA, C. G., BACKHAUS, M., BLUEMKE, D. A., BRITTEN, R. D., CHUNG, J. D., COWAN, B. R., DINOV, I. D., FINN, J. P., HUNTER, P. J., KADISH, A. H., AND OTHERS. **The cardiac atlas project—an imaging database for computational modeling and statistical atlases of the heart**. *Bioinformatics 27*, 16 (2011), 2288–2295.

[38] PETITJEAN, C., AND DACHER, J.-N. **A review of segmentation methods in short axis cardiac mr images**. *Medical image analysis 15*, 2 (2011), 169–184.

[39] HENNEMUTH, A., FRIMAN, O., HUELLEBRAND, M., AND PEITGEN, H.-O. **Mixture-model-based segmentation of myocardial delayed enhancement mri**. In *International Workshop on Statistical Atlases and Computational Models of the Heart* (2012), Springer, pp. 87–96.

[40] HINTON, G. E., SRIVASTAVA, N., KRIZHEVSKY, A., SUTSKEVER, I., AND SALAKHUTDINOV, R. R. **Improving neural networks by preventing co-adaptation of feature detectors**. *arXiv preprint arXiv:1207.0580* (2012).

[41] ZEILER, M. D. **Adadelta: an adaptive learning rate method**. *arXiv preprint arXiv:1212.5701* (2012).

[42] MAZAHERI, S., SULAIMAN, P. S. B., WIRZA, R., KHALID, F., KADIMAN, S., DIMON, M. Z., AND TAYEBI, R. M. **Echocardiography image segmentation: A survey**. In *2013 International Conference on Advanced Computer Science Applications and Technologies* (2013), IEEE, pp. 327–332.

[43] NAVARRO, M. A., KIM, M., AND SALCEDO, E. E. **Real-time 3d echocardiography in percutaneous balloon mitral valvuloplasty**. *Hot Topics in Echocardiography* (2013), 101.

[44] PRASOON, A., PETERSEN, K., IGEL, C., LAUZE, F., DAM, E., AND NIELSEN, M. **Deep feature learning for knee cartilage segmentation using a triplanar convolutional neural network**. In *International conference on medical image computing and computer-assisted intervention* (2013), Springer, pp. 246–253.

[45] RUBENSTEIN, J. C., LEE, D. C., WU, E., KADISH, A. H., PASSMAN, R., BELLO, D., AND GOLDBERGER, J. J. **A comparison of cardiac magnetic resonance imaging peri-infarct border zone quantification strategies for the prediction of ventricular tachyarrhythmia inducibility**. *Cardiology journal 20*, 1 (2013), 68–77.

[46] GOODFELLOW, J. **Pouget-abadie, m**. *Mirza, B. Xu, D. Warde-Farley, S. Ozair, A. Courville, Y. Bengio, Generative Adversarial Networks* (2014).

[47] KINGMA, D. P., AND BA, J. **Adam: A method for stochastic optimization**. *arXiv preprint arXiv:1412.6980* (2014).

[48] KLEESIEK, J., BILLER, A., URBAN, G., KOTHE, U., BENDSZUS, M., AND HAMPRECHT, F. **Ilastik for multi-modal brain tumor segmentation**. *Proceedings MICCAI BraTS (brain tumor segmentation challenge)* (2014), 12–17.

[49] LITJENS, G., TOTH, R., VAN DE VEN, W., HOEKS, C., KERKSTRA, S., VAN GINNEKEN, B., VINCENT, G., GUILLARD, G., BIRBECK, N., ZHANG, J., AND OTHERS.

Evaluation of prostate segmentation algorithms for mri: the promise12 challenge. *Medical image analysis 18*, 2 (2014), 359–373.

[50] MENZE, B. H., JAKAB, A., BAUER, S., KALPATHY-CRAMER, J., FARAHANI, K., KIRBY, J., BURREN, Y., PORZ, N., SLOTBOOM, J., WIEST, R., AND OTHERS. **The multimodal brain tumor image segmentation benchmark (brats)**. *IEEE transactions on medical imaging 34*, 10 (2014), 1993–2024.

[51] NISHII, T., KONO, A. K., SHIGERU, M., TAKAMINE, S., FUJIWARA, S., KYOTANI, K., AOYAMA, N., AND SUGIMURA, K. **Cardiovascular magnetic resonance t2 mapping can detect myocardial edema in idiopathic dilated cardiomyopathy**. *The international journal of cardiovascular imaging 30*, 1 (2014), 65–72.

[52] QUEIRÓS, S., BARBOSA, D., HEYDE, B., MORAIS, P., VILAÇA, J. L., FRIBOULET, D., BERNARD, O., AND D'HOOGE, J. **Fast automatic myocardial segmentation in 4d cine cmr datasets**. *Medical image analysis 18*, 7 (2014), 1115–1131.

[53] SIMONYAN, K., AND ZISSERMAN, A. **Very deep convolutional networks for large-scale image recognition**. *arXiv preprint arXiv:1409.1556* (2014).

[54] SRIVASTAVA, N., HINTON, G., KRIZHEVSKY, A., SUTSKEVER, I., AND SALAKHUTDINOV, R. **Dropout: a simple way to prevent neural networks from overfitting**. *The journal of machine learning research 15*, 1 (2014), 1929–1958.

[55] SUINESIAPUTRA, A., COWAN, B. R., AL-AGAMY, A. O., ELATTAR, M. A., AYACHE, N., FAHMY, A. S., KHALIFA, A. M., MEDRANO-GRACIA, P., JOLLY, M.-P., KADISH, A. H., AND OTHERS. **A collaborative resource to build consensus for automated left ventricular segmentation of cardiac mr images**. *Medical image analysis 18*, 1 (2014), 50–62.

[56] BOULETI, C., MEWTON, N., AND GERMAIN, S. **The no-reflow phenomenon: state of the art**. *Archives of cardiovascular diseases 108*, 12 (2015), 661–674.

[57] HE, K., ZHANG, X., REN, S., AND SUN, J. **Delving deep into rectifiers: Surpassing human-level performance on imagenet classification**. In *Proceedings of the IEEE international conference on computer vision* (2015), pp. 1026–1034.

[58] IOFFE, S., AND SZEGEDY, C. **Batch normalization: Accelerating deep network training by reducing internal covariate shift**. In *International conference on machine learning* (2015), PMLR, pp. 448–456.

[59] LEE, C.-Y., XIE, S., GALLAGHER, P., ZHANG, Z., AND TU, Z. **Deeply-supervised nets**. In *Artificial intelligence and statistics* (2015), PMLR, pp. 562–570.

[60] LEONARD, S. L. **Pathophysiology of heart disease: A collaborative project of medical students and faculty, 6e**, 2015.

[61] LONG, J., SHELHAMER, E., AND DARRELL, T. **Fully convolutional networks for semantic segmentation**. In *Proceedings of the IEEE conference on computer vision and pattern recognition* (2015), pp. 3431–3440.

[62] MISHKIN, D., AND MATAS, J. **All you need is a good init**. *arXiv preprint arXiv:1511.06422* (2015).

[63] PFEIFFER, M. P., AND BIEDERMAN, R. W. **Cardiac mri: a general overview with emphasis on current use and indications**. *Medical Clinics 99*, 4 (2015), 849–861.

[64] RONNEBERGER, O., FISCHER, P., AND BROX, T. **U-net: Convolutional networks for biomedical image segmentation**. In *International Conference on Medical image computing and computer-assisted intervention* (2015), Springer, pp. 234–241.

[65] ROTH, H. R., LU, L., FARAG, A., SHIN, H.-C., LIU, J., TURKBEY, E. B., AND SUMMERS, R. M. **Deeporgan: Multi-level deep convolutional networks for automated pancreas segmentation**. In *International conference on medical image computing and computer-assisted intervention* (2015), Springer, pp. 556–564.

[66] SZEGEDY, C., LIU, W., JIA, Y., SERMANET, P., REED, S., ANGUELOV, D., ERHAN, D., VANHOUCKE, V., AND RABINOVICH, A. **Going deeper with convolutions**. In *Proceedings of the IEEE conference on computer vision and pattern recognition* (2015), pp. 1–9.

[67] YU, F., AND KOLTUN, V. **Multi-scale context aggregation by dilated convolutions**. *arXiv preprint arXiv:1511.07122* (2015).

[68] AVENDI, M., KHERADVAR, A., AND JAFARKHANI, H. **A combined deep-learning and deformable-model approach to fully automatic segmentation of the left ventricle in cardiac mri**. *Medical image analysis 30* (2016), 108–119.

[69] CARMINATI, M. C., BONIOTTI, C., FUSINI, L., ANDREINI, D., PONTONE, G., PEPI, M., AND CAIANI, E. G. **Comparison of image processing techniques for nonviable tissue quantification in late gadolinium enhancement cardiac magnetic resonance images**. *Journal of thoracic imaging 31*, 3 (2016), 168–176.

[70] ÇIÇEK, Ö., ABDULKADIR, A., LIENKAMP, S. S., BROX, T., AND RONNEBERGER, O. **3d u-net: learning dense volumetric segmentation from sparse annotation**. In *International conference on medical image computing and computer-assisted intervention* (2016), Springer, pp. 424–432.

[71] GOODFELLOW, I., BENGIO, Y., AND COURVILLE, A. **Deep learning**. MIT press, 2016.

[72] HE, K., ZHANG, X., REN, S., AND SUN, J. **Deep residual learning for image recognition**. In *Proceedings of the IEEE conference on computer vision and pattern recognition* (2016), pp. 770–778.

[73] HUTTIN, O., VOILLIOT, D., MANDRY, D., VENNER, C., JUILLIÈRE, Y., AND SELTON-SUTY, C. **All you need to know about the tricuspid valve: tricuspid valve imaging and tricuspid regurgitation analysis**. *Archives of cardiovascular diseases 109*, 1 (2016), 67–80.

[74] KALINOVSKY, A., AND KOVALEV, V. **Lung image ssgmentation using deep learning methods and convolutional neural networks**.

[75] KARIM, R., BHAGIRATH, P., CLAUS, P., HOUSDEN, R. J., CHEN, Z., KARIMAGHALOO, Z., SOHN, H.-M., RODRÍGUEZ, L. L., VERA, S., ALBÀ, X., AND OTHERS. **Evaluation of state-of-the-art segmentation algorithms for left ventricle infarct from late gadolinium enhancement mr images**. *Medical image analysis 30* (2016), 95–107.

[76] LI, J., ZHANG, R., SHI, L., AND WANG, D. **Automatic whole-heart segmentation in congenital heart disease using deeply-supervised 3d fcn**. In *Reconstruction, Segmentation, and Analysis of Medical Images*. Springer, 2016, pp. 111–118.

[77] LUC, P., COUPRIE, C., CHINTALA, S., AND VERBEEK, J. **Semantic segmentation using adversarial networks**. *arXiv preprint arXiv:1611.08408* (2016).

[78] MILLETARI, F., NAVAB, N., AND AHMADI, S.-A. **V-net: Fully convolutional neural networks for volumetric medical image segmentation**. In *2016 fourth international conference on 3D vision (3DV)* (2016), IEEE, pp. 565–571.

[79] MOESKOPS, P., WOLTERINK, J. M., VAN DER VELDEN, B. H., GILHUIJS, K. G., LEINER, T., VIERGEVER, M. A., AND IŠGUM, I. **Deep learning for multi-task medical image segmentation in multiple modalities**. In *International Conference on Medical Image Computing and Computer-Assisted Intervention* (2016), Springer, pp. 478–486.

[80] OKTAY, O., BAI, W., LEE, M., GUERRERO, R., KAMNITSAS, K., CABALLERO, J., DE MARVAO, A., COOK, S., O'REGAN, D., AND RUECKERT, D. **Multi-input cardiac image super-resolution using convolutional neural networks**. In *International conference on medical image computing and computer-assisted intervention* (2016), Springer, pp. 246–254.

[81] PASZKE, A., CHAURASIA, A., KIM, S., AND CULURCIELLO, E. **Enet: A deep neural network architecture for real-time semantic segmentation**. *arXiv preprint arXiv:1606.02147* (2016).

[82] PEREIRA, S., PINTO, A., ALVES, V., AND SILVA, C. A. **Brain tumor segmentation using convolutional neural networks in mri images**. *IEEE transactions on medical imaging 35*, 5 (2016), 1240–1251.

[83] POUDEL, R. P., LAMATA, P., AND MONTANA, G. **Recurrent fully convolutional neural networks for multi-slice mri cardiac segmentation**. In *Reconstruction, segmentation, and analysis of medical images*. Springer, 2016, pp. 83–94.

[84] SHI, B., BAI, X., AND YAO, C. **An end-to-end trainable neural network for image-based sequence recognition and its application to scene text recognition**. *IEEE transactions on pattern analysis and machine intelligence 39*, 11 (2016), 2298–2304.

[85] TAN, L. K., LIEW, Y. M., LIM, E., AND MCLAUGHLIN, R. A. **Cardiac left ventricle segmentation using convolutional neural network regression**. In *2016 IEEE EMBS Conference on Biomedical Engineering and Sciences (IECBES)* (2016), IEEE, pp. 490–493.

[86] TRAN, P. V. **A fully convolutional neural network for cardiac segmentation in short-axis mri**. *arXiv preprint arXiv:1604.00494* (2016).

[87] ULYANOV, D., VEDALDI, A., AND LEMPITSKY, V. **Instance normalization: The missing ingredient for fast stylization**. *arXiv preprint arXiv:1607.08022* (2016).

[88] WOLTERINK, J. M., LEINER, T., VIERGEVER, M. A., AND IŠGUM, I. **Dilated convolutional neural networks for cardiovascular mr segmentation in congenital heart disease**. In *Reconstruction, segmentation, and analysis of medical images*. Springer, 2016, pp. 95–102.

[89] ZHOU, X., ITO, T., TAKAYAMA, R., WANG, S., HARA, T., AND FUJITA, H. **Three-dimensional ct image segmentation by combining 2d fully convolutional network with 3d majority voting**. In *Deep Learning and Data Labeling for Medical Applications*. Springer, 2016, pp. 111–120.

[90] BADRINARAYANAN, V., KENDALL, A., AND CIPOLLA, R. **Segnet: A deep convolutional encoder-decoder architecture for image segmentation**. *IEEE transactions on pattern analysis and machine intelligence 39*, 12 (2017), 2481–2495.

[91] BAUMGARTNER, C. F., KOCH, L. M., POLLEFEYS, M., AND KONUKOGLU, E. **An exploration of 2d and 3d deep learning techniques for cardiac mr image seg-**

mentation. In *International Workshop on Statistical Atlases and Computational Models of the Heart* (2017), Springer, pp. 111–119.

[92] CHEN, L.-C., PAPANDREOU, G., SCHROFF, F., AND ADAM, H. **Rethinking atrous convolution for semantic image segmentation**. *arXiv preprint arXiv:1706.05587* (2017).

[93] GRINIAS, E., AND TZIRITAS, G. **Fast fully-automatic cardiac segmentation in mri using mrf model optimization, substructures tracking and b-spline smoothing**. In *International Workshop on Statistical Atlases and Computational Models of the Heart* (2017), Springer, pp. 91–100.

[94] HAVAEI, M., DAVY, A., WARDE-FARLEY, D., BIARD, A., COURVILLE, A., BENGIO, Y., PAL, C., JODOIN, P.-M., AND LAROCHELLE, H. **Brain tumor segmentation with deep neural networks**. *Medical image analysis 35* (2017), 18–31.

[95] HU, P., WU, F., PENG, J., BAO, Y., CHEN, F., AND KONG, D. **Automatic abdominal multi-organ segmentation using deep convolutional neural network and time-implicit level sets**. *International journal of computer assisted radiology and surgery 12*, 3 (2017), 399–411.

[96] HUANG, G., LIU, Z., VAN DER MAATEN, L., AND WEINBERGER, K. Q. **Densely connected convolutional networks**. In *Proceedings of the IEEE conference on computer vision and pattern recognition* (2017), pp. 4700–4708.

[97] ISENSEE, F., JAEGER, P. F., FULL, P. M., WOLF, I., ENGELHARDT, S., AND MAIER-HEIN, K. H. **Automatic cardiac disease assessment on cine-mri via time-series segmentation and domain specific features**. In *International workshop on statistical atlases and computational models of the heart* (2017), Springer, pp. 120–129.

[98] JANG, Y., HONG, Y., HA, S., KIM, S., AND CHANG, H.-J. **Automatic segmentation of lv and rv in cardiac mri**. In *International Workshop on Statistical Atlases and Computational Models of the Heart* (2017), Springer, pp. 161–169.

[99] KAMNITSAS, K., LEDIG, C., NEWCOMBE, V. F., SIMPSON, J. P., KANE, A. D., MENON, D. K., RUECKERT, D., AND GLOCKER, B. **Efficient multi-scale 3d cnn with fully connected crf for accurate brain lesion segmentation**. *Medical image analysis 36* (2017), 61–78.

[100] KIM, P. K., HONG, Y. J., IM, D. J., SUH, Y. J., PARK, C. H., KIM, J. Y., CHANG, S., LEE, H.-J., HUR, J., KIM, Y. J., AND OTHERS. **Myocardial t1 and t2 mapping: techniques and clinical applications**. *Korean journal of radiology 18*, 1 (2017), 113–131.

[101] LIAO, F., CHEN, X., HU, X., AND SONG, S. **Estimation of the volume of the left ventricle from mri images using deep neural networks**. *IEEE transactions on cybernetics 49*, 2 (2017), 495–504.

[102] LIN, T.-Y., GOYAL, P., GIRSHICK, R., HE, K., AND DOLLÁR, P. **Focal loss for dense object detection**. In *Proceedings of the IEEE international conference on computer vision* (2017), pp. 2980–2988.

[103] MALEKI, M., ALIZADEHASL, A., AND HAGHJOO, M. **Practical cardiology**.

[104] MAVROGENI, S., APOSTOLOU, D., ARGYRIOU, P., VELITSISTA, S., PAPA, L., EFENTAKIS, S., VERNARDOS, E., KANOUPAKI, M., KANOUPAKIS, G., AND MANGINAS, A. **T1 and t2 mapping in cardiology:"mapping the obscure object of desire"**. *Cardiology 138*, 4 (2017), 207–217.

[105] MILLETARI, F., AHMADI, S.-A., KROLL, C., PLATE, A., ROZANSKI, V., MAIOSTRE, J., LEVIN, J., DIETRICH, O., ERTL-WAGNER, B., BÖTZEL, K., AND OTHERS. **Hough-cnn: deep learning for segmentation of deep brain regions in mri and ultrasound**. *Computer Vision and Image Understanding 164* (2017), 92–102.

[106] NGO, T. A., LU, Z., AND CARNEIRO, G. **Combining deep learning and level set for the automated segmentation of the left ventricle of the heart from cardiac cine magnetic resonance**. *Medical image analysis 35* (2017), 159–171.

[107] OKTAY, O., FERRANTE, E., KAMNITSAS, K., HEINRICH, M., BAI, W., CABALLERO, J., COOK, S. A., DE MARVAO, A., DAWES, T., O'REGAN, D. P., AND OTHERS. **Anatomically constrained neural networks (acnns): application to cardiac image enhancement and segmentation**. *IEEE transactions on medical imaging 37*, 2 (2017), 384–395.

[108] PATRAVALI, J., JAIN, S., AND CHILAMKURTHY, S. **2d-3d fully convolutional neural networks for cardiac mr segmentation**. In *International Workshop on Statistical Atlases and Computational Models of the Heart* (2017), Springer, pp. 130–139.

[109] ROHÉ, M.-M. **Reduced representation of segmentation and tracking in cardiac images for group-wise longitudinal analysis**. PhD thesis, Université Côte d'Azur, 2017.

[110] ROHÉ, M.-M., SERMESANT, M., AND PENNEC, X. **Automatic multi-atlas segmentation of myocardium with svf-net**. In *International Workshop on Statistical Atlases and Computational Models of the Heart* (2017), Springer, pp. 170–177.

[111] TAN, L. K., LIEW, Y. M., LIM, E., AND MCLAUGHLIN, R. A. **Convolutional neural network regression for short-axis left ventricle segmentation in cardiac cine mr sequences**. *Medical image analysis 39* (2017), 78–86.

[112] TRULLO, R., PETITJEAN, C., NIE, D., SHEN, D., AND RUAN, S. **Joint segmentation of multiple thoracic organs in ct images with two collaborative deep architectures**. In *Deep Learning in Medical Image Analysis and Multimodal Learning for Clinical Decision Support*. Springer, 2017, pp. 21–29.

[113] VASWANI, A., SHAZEER, N., PARMAR, N., USZKOREIT, J., JONES, L., GOMEZ, A. N., KAISER, Ł., AND POLOSUKHIN, I. **Attention is all you need**. In *Advances in neural information processing systems* (2017), pp. 5998–6008.

[114] WANG, C., AND SMEDBY, Ö. **Automatic whole heart segmentation using deep learning and shape context**. In *International Workshop on Statistical Atlases and Computational Models of the Heart* (2017), Springer, pp. 242–249.

[115] WOLTERINK, J. M., LEINER, T., VIERGEVER, M. A., AND IŠGUM, I. **Automatic segmentation and disease classification using cardiac cine mr images**. In *International Workshop on Statistical Atlases and Computational Models of the Heart* (2017), Springer, pp. 101–110.

[116] YANG, G., ZHUANG, X., KHAN, H., HALDAR, S., NYKTARI, E., YE, X., SLABAUGH, G., WONG, T., MOHIADDIN, R., KEEGAN, J., AND OTHERS. **Segmenting atrial fibrosis from late gadolinium-enhanced cardiac mri by deep-learned features with stacked sparse auto-encoders**. In *Annual Conference on Medical Image Understanding and Analysis* (2017), Springer, pp. 195–206.

[117] YANG, X., BIAN, C., YU, L., NI, D., AND HENG, P.-A. **Class-balanced deep neural network for automatic ventricular structure segmentation**. In *International workshop on statistical atlases and computational models of the heart* (2017), Springer, pp. 152–160.

[118] YANG, X., BIAN, C., YU, L., NI, D., AND HENG, P.-A. **Hybrid loss guided convolutional networks for whole heart parsing**. In *International workshop on statistical atlases and computational models of the heart* (2017), Springer, pp. 215–223.

[119] YANG, X., YU, L., WU, L., WANG, Y., NI, D., QIN, J., AND HENG, P.-A. **Fine-grained recurrent neural networks for automatic prostate segmentation in ultrasound images**. In *Proceedings of the AAAI Conference on Artificial Intelligence* (2017), vol. 31.

[120] YU, L., CHENG, J.-Z., DOU, Q., YANG, X., CHEN, H., QIN, J., AND HENG, P.-A. **Automatic 3d cardiovascular mr segmentation with densely-connected volumetric convnets**. In *International conference on medical image computing and computer-assisted intervention* (2017), Springer, pp. 287–295.

[121] YU, L., YANG, X., CHEN, H., QIN, J., AND HENG, P. A. **Volumetric convnets with mixed residual connections for automated prostate segmentation from 3d mr images**. In *Thirty-first AAAI conference on artificial intelligence* (2017).

[122] YUAN, Y., CHAO, M., AND LO, Y.-C. **Automatic skin lesion segmentation using deep fully convolutional networks with jaccard distance**. *IEEE transactions on medical imaging 36*, 9 (2017), 1876–1886.

[123] ZHANG, H., CISSE, M., DAUPHIN, Y. N., AND LOPEZ-PAZ, D. **mixup: Beyond empirical risk minimization**. *arXiv preprint arXiv:1710.09412* (2017).

[124] ZHOU, X., TAKAYAMA, R., WANG, S., HARA, T., AND FUJITA, H. **Deep learning of the sectional appearances of 3d ct images for anatomical structure segmentation based on an fcn voting method**. *Medical physics 44*, 10 (2017), 5221–5233.

[125] ZOTTI, C., LUO, Z., HUMBERT, O., LALANDE, A., AND JODOIN, P.-M. **Gridnet with automatic shape prior registration for automatic mri cardiac segmentation**. In *International workshop on statistical atlases and computational models of the heart* (2017), Springer, pp. 73–81.

[126] BERNARD, O., LALANDE, A., ZOTTI, C., CERVENANSKY, F., YANG, X., HENG, P.-A., CETIN, I., LEKADIR, K., CAMARA, O., BALLESTER, M. A. G., AND OTHERS. **Deep learning techniques for automatic mri cardiac multi-structures segmentation and diagnosis: Is the problem solved?** *IEEE transactions on medical imaging 37*, 11 (2018), 2514–2525.

[127] CHEN, C., BAI, W., AND RUECKERT, D. **Multi-task learning for left atrial segmentation on ge-mri**. In *International workshop on statistical atlases and computational models of the heart* (2018), Springer, pp. 292–301.

[128] CHEN, J., YANG, G., GAO, Z., NI, H., ANGELINI, E., MOHIADDIN, R., WONG, T., ZHANG, Y., DU, X., ZHANG, H., AND OTHERS. **Multiview two-task recursive attention model for left atrium and atrial scars segmentation**. In *International Conference on Medical Image Computing and Computer-Assisted Intervention* (2018), Springer, pp. 455–463.

[129] CHEN, L.-C., ZHU, Y., PAPANDREOU, G., SCHROFF, F., AND ADAM, H. **Encoder-decoder with atrous separable convolution for semantic image segmentation**. In *Proceedings of the European conference on computer vision (ECCV)* (2018), pp. 801–818.

[130] CONG, C., AND ZHANG, H. **Invert-u-net dnn segmentation model for mri cardiac left ventricle segmentation**. *The Journal of Engineering 2018*, 16 (2018), 1463–1467.

[131] DANGI, S., YANIV, Z., AND LINTE, C. A. **Left ventricle segmentation and quantification from cardiac cine mr images via multi-task learning**. In *International Workshop on Statistical Atlases and Computational Models of the Heart* (2018), Springer, pp. 21–31.

[132] DUAN, J., SCHLEMPER, J., BAI, W., DAWES, T. J., BELLO, G., DOUMOU, G., DE MARVAO, A., O'REGAN, D. P., AND RUECKERT, D. **Deep nested level sets: Fully automated segmentation of cardiac mr images in patients with pulmonary hypertension**. In *International Conference on Medical Image Computing and Computer-Assisted Intervention* (2018), Springer, pp. 595–603.

[133] FAHMY, A. S., RAUSCH, J., NEISIUS, U., CHAN, R. H., MARON, M. S., APPELBAUM, E., MENZE, B., AND NEZAFAT, R. **Automated cardiac mr scar quantification in hypertrophic cardiomyopathy using deep convolutional neural networks**. *JACC: Cardiovascular Imaging 11*, 12 (2018), 1917–1918.

[134] FU, M., WU, W., HONG, X., LIU, Q., JIANG, J., OU, Y., ZHAO, Y., AND GONG, X. **Hierarchical combinatorial deep learning architecture for pancreas segmentation of medical computed tomography cancer images**. *BMC systems biology 12*, 4 (2018), 119–127.

[135] GAJARSKY, T., AND PURWINS, H. **An xception residual recurrent neural network for audio event detection and tagging**. In *15th International Sound & Music Computing Conference* (2018), Sound and Music Computing Network, pp. 210–216.

[136] GIBSON, E., GIGANTI, F., HU, Y., BONMATI, E., BANDULA, S., GURUSAMY, K., DAVIDSON, B., PEREIRA, S. P., CLARKSON, M. J., AND BARRATT, D. C. **Automatic multi-organ segmentation on abdominal ct with dense v-networks**. *IEEE transactions on medical imaging 37*, 8 (2018), 1822–1834.

[137] GORDIENKO, Y., GANG, P., HUI, J., ZENG, W., KOCHURA, Y., ALIENIN, O., ROKOVYI, O., AND STIRENKO, S. **Deep learning with lung segmentation and bone shadow exclusion techniques for chest x-ray analysis of lung cancer**. In *International Conference on Computer Science, Engineering and Education Applications* (2018), Springer, pp. 638–647.

[138] JIE, H., LI, S., GANG, S., AND OTHERS. **Squeeze-and-excitation networks**. In *Proceedings of the IEEE conference on computer vision and pattern recognition* (2018), vol. 5.

[139] LAU, F., HENDRIKS, T., LIEMAN-SIFRY, J., SALL, S., AND GOLDEN, D. **Scargan: chained generative adversarial networks to simulate pathological tissue on**

cardiovascular mr scans. In *Deep learning in medical image analysis and multimodal learning for clinical decision support*. Springer, 2018, pp. 343–350.

[140] QIN, C., BAI, W., SCHLEMPER, J., PETERSEN, S. E., PIECHNIK, S. K., NEUBAUER, S., AND RUECKERT, D. **Joint learning of motion estimation and segmentation for cardiac mr image sequences**. In *International Conference on Medical Image Computing and Computer-Assisted Intervention* (2018), Springer, pp. 472–480.

[141] SAVIOLI, N., VIEIRA, M. S., LAMATA, P., AND MONTANA, G. **A generative adversarial model for right ventricle segmentation**. *arXiv preprint arXiv:1810.03969* (2018).

[142] SCHLEMPER, J., OKTAY, O., BAI, W., CASTRO, D. C., DUAN, J., QIN, C., HAJNAL, J. V., AND RUECKERT, D. **Cardiac mr segmentation from undersampled k-space using deep latent representation learning**. In *International Conference on Medical Image Computing and Computer-Assisted Intervention* (2018), Springer, pp. 259–267.

[143] SHI, Z., ZENG, G., ZHANG, L., ZHUANG, X., LI, L., YANG, G., AND ZHENG, G. **Bayesian voxdrn: A probabilistic deep voxelwise dilated residual network for whole heart segmentation from 3d mr images**. In *International Conference on Medical Image Computing and Computer-Assisted Intervention* (2018), Springer, pp. 569–577.

[144] VIGNEAULT, D. M., XIE, W., HO, C. Y., BLUEMKE, D. A., AND NOBLE, J. A. **ω-net (omega-net): fully automatic, multi-view cardiac mr detection, orientation, and segmentation with deep neural networks**. *Medical image analysis 48* (2018), 95–106.

[145] WOO, S., PARK, J., LEE, J.-Y., AND SO KWEON, I. **Cbam: Convolutional block attention module**. In *Proceedings of the European conference on computer vision (ECCV)* (2018), pp. 3–19.

[146] XIA, Q., YAO, Y., HU, Z., AND HAO, A. **Automatic 3d atrial segmentation from ge-mris using volumetric fully convolutional networks**. In *International Workshop on Statistical Atlases and Computational Models of the Heart* (2018), Springer, pp. 211–220.

[147] XIONG, Z., FEDOROV, V. V., FU, X., CHENG, E., MACLEOD, R., AND ZHAO, J. **Fully automatic left atrium segmentation from late gadolinium enhanced magnetic resonance imaging using a dual fully convolutional neural network**. *IEEE transactions on medical imaging 38*, 2 (2018), 515–524.

[148] XU, C., XU, L., GAO, Z., ZHAO, S., ZHANG, H., ZHANG, Y., DU, X., ZHAO, S., GHISTA, D., LIU, H., AND OTHERS. **Direct delineation of myocardial infarction without contrast agents using a joint motion feature learning architecture**. *Medical image analysis 50* (2018), 82–94.

[149] YAN, W., WANG, Y., LI, Z., VAN DER GEEST, R. J., AND TAO, Q. **Left ventricle segmentation via optical-flow-net from short-axis cine mri: preserving the temporal coherence of cardiac motion**. In *International Conference on medical image computing and computer-assisted intervention* (2018), Springer, pp. 613–621.

[150] YANG, J., VEERARAGHAVAN, H., ARMATO III, S. G., FARAHANI, K., KIRBY, J. S., KALPATHY-KRAMER, J., VAN ELMPT, W., DEKKER, A., HAN, X., FENG, X., AND OTHERS. **Autosegmentation for thoracic radiation treatment planning: a grand challenge at aapm 2017**. *Medical physics 45*, 10 (2018), 4568–4581.

[151] ZABIHOLLAHY, F., WHITE, J. A., AND UKWATTA, E. **Myocardial scar segmentation from magnetic resonance images using convolutional neural network**. In *Medical Imaging 2018: Computer-Aided Diagnosis* (2018), vol. 10575, International Society for Optics and Photonics, p. 105752Z.

[152] ZHANG, L., KARANIKOLAS, G. V., AKÇAKAYA, M., AND GIANNAKIS, G. B. **Fully automatic segmentation of the right ventricle via multi-task deep neural networks**. In *2018 IEEE International Conference on Acoustics, Speech and Signal Processing (ICASSP)* (2018), IEEE, pp. 6677–6681.

[153] ZHAO, H., QI, X., SHEN, X., SHI, J., AND JIA, J. **Icnet for real-time semantic segmentation on high-resolution images**. In *Proceedings of the European conference on computer vision (ECCV)* (2018), pp. 405–420.

[154] ZHENG, Q., DELINGETTE, H., DUCHATEAU, N., AND AYACHE, N. **3-d consistent and robust segmentation of cardiac images by deep learning with spatial propagation**. *IEEE transactions on medical imaging 37*, 9 (2018), 2137–2148.

[155] ZHUANG, X. **Multivariate mixture model for myocardial segmentation combining multi-source images**. *IEEE transactions on pattern analysis and machine intelligence 41*, 12 (2018), 2933–2946.

[156] ZOTTI, C., LUO, Z., LALANDE, A., AND JODOIN, P.-M. **Convolutional neural network with shape prior applied to cardiac mri segmentation**. *IEEE journal of biomedical and health informatics 23*, 3 (2018), 1119–1128.

[157] AZAD, R., ASADI-AGHBOLAGHI, M., FATHY, M., AND ESCALERA, S. **Bi-directional convlstm u-net with densley connected convolutions**. In *Proceedings of the*

IEEE/CVF International Conference on Computer Vision Workshops (2019), pp. 0–0.

[158] CAMPELLO, V. M., MARTÍN-ISLA, C., IZQUIERDO, C., PETERSEN, S. E., BALLESTER, M. A. G., AND LEKADIR, K. **Combining multi-sequence and synthetic images for improved segmentation of late gadolinium enhancement cardiac mri**. In *International Workshop on Statistical Atlases and Computational Models of the Heart* (2019), Springer, pp. 290–299.

[159] CHEN, C., BIFFI, C., TARRONI, G., PETERSEN, S., BAI, W., AND RUECKERT, D. **Learning shape priors for robust cardiac mr segmentation from multi-view images**. In *International Conference on Medical Image Computing and Computer-Assisted Intervention* (2019), Springer, pp. 523–531.

[160] CHEN, M., FANG, L., AND LIU, H. **Fr-net: Focal loss constrained deep residual networks for segmentation of cardiac mri**. In *2019 IEEE 16th International Symposium on Biomedical Imaging (ISBI 2019)* (2019), IEEE, pp. 764–767.

[161] CHEN, S., MA, K., AND ZHENG, Y. **Med3d: Transfer learning for 3d medical image analysis**. *arXiv preprint arXiv:1904.00625* (2019).

[162] CLOUGH, J. R., OKSUZ, I., BYRNE, N., SCHNABEL, J. A., AND KING, A. P. **Explicit topological priors for deep-learning based image segmentation using persistent homology**. In *International Conference on Information Processing in Medical Imaging* (2019), Springer, pp. 16–28.

[163] DE LA ROSA, E., SIDIBÉ, D., DECOURSELLE, T., LECLERCQ, T., COCHET, A., AND LALANDE, A. **Myocardial infarction quantification from late gadolinium enhancement mri using top-hat transforms and neural networks**. *arXiv preprint arXiv:1901.02911* (2019).

[164] DU, X., YIN, S., TANG, R., ZHANG, Y., AND LI, S. **Cardiac-deepied: automatic pixel-level deep segmentation for cardiac bi-ventricle using improved end-to-end encoder-decoder network**. *IEEE journal of translational engineering in health and medicine 7* (2019), 1–10.

[165] FAHMY, A. S., EL-REWAIDY, H., NEZAFAT, M., NAKAMORI, S., AND NEZAFAT, R. **Automated analysis of cardiovascular magnetic resonance myocardial native t 1 mapping images using fully convolutional neural networks**. *Journal of Cardiovascular Magnetic Resonance 21*, 1 (2019), 1–12.

[166] GANAYE, P.-A., SDIKA, M., TRIGGS, B., AND BENOIT-CATTIN, H. **Removing segmentation inconsistencies with semi-supervised non-adjacency constraint**. *Medical image analysis 58* (2019), 101551.

[167] HUANG, Y., WANG, Q., JIA, W., AND HE, X. **See more than once–kernel-sharing atrous convolution for semantic segmentation**. *arXiv preprint arXiv:1908.09443* (2019).

[168] KERVADEC, H., BOUCHTIBA, J., DESROSIERS, C., GRANGER, E., DOLZ, J., AND AYED, I. B. **Boundary loss for highly unbalanced segmentation**. In *International conference on medical imaging with deep learning* (2019), PMLR, pp. 285–296.

[169] KHENED, M., KOLLERATHU, V. A., AND KRISHNAMURTHI, G. **Fully convolutional multi-scale residual densenets for cardiac segmentation and automated cardiac diagnosis using ensemble of classifiers**. *Medical image analysis 51* (2019), 21–45.

[170] KOPELOWITZ, E., AND ENGELHARD, G. **Lung nodules detection and segmentation using 3d mask-rcnn**. *arXiv preprint arXiv:1907.07676* (2019).

[171] KREGNES, A. **Myocardial segmentation in lge-cmr images using deep neural networks**. Master's thesis, University of Stavanger, Norway, 2019.

[172] LI, C., TONG, Q., LIAO, X., SI, W., CHEN, S., WANG, Q., AND YUAN, Z. **Apcp-net: aggregated parallel cross-scale pyramid network for cmr segmentation**. In *2019 IEEE 16th International Symposium on Biomedical Imaging (ISBI 2019)* (2019), IEEE, pp. 784–788.

[173] LI, J., YU, Z. L., GU, Z., LIU, H., AND LI, Y. **Dilated-inception net: multi-scale feature aggregation for cardiac right ventricle segmentation**. *IEEE Transactions on Biomedical Engineering 66*, 12 (2019), 3499–3508.

[174] LIU, S., WANG, Y., YANG, X., LEI, B., LIU, L., LI, S. X., NI, D., AND WANG, T. **Deep learning in medical ultrasound analysis: a review**. *Engineering 5*, 2 (2019), 261–275.

[175] LU, X., CHEN, X., LI, W., AND QIAO, Y. **Graph cut segmentation of the right ventricle in cardiac mri using multi-scale feature learning**. In *Proceedings of the 3rd International Conference on Cryptography, Security and Privacy* (2019), pp. 231–235.

[176] MEDLEY, D. O., SANTIAGO, C., AND NASCIMENTO, J. C. **Segmenting the left ventricle in cardiac in cardiac mri: From handcrafted to deep region based descriptors**. In *2019 IEEE 16th International Symposium on Biomedical Imaging (ISBI 2019)* (2019), IEEE, pp. 644–648.

[177] MOCCIA, S., BANALI, R., MARTINI, C., MUSCOGIURI, G., PONTONE, G., PEPI, M., AND CAIANI, E. G. **Development and testing of a deep learning-based strategy**

for scar segmentation on cmr-lge images. *Magnetic Resonance Materials in Physics, Biology and Medicine 32*, 2 (2019), 187–195.

[178] PAINCHAUD, N., SKANDARANI, Y., JUDGE, T., BERNARD, O., LALANDE, A., AND JODOIN, P.-M. **Cardiac mri segmentation with strong anatomical guarantees**. In *International Conference on Medical Image Computing and Computer-Assisted Intervention* (2019), Springer, pp. 632–640.

[179] QI, K., YANG, H., LI, C., LIU, Z., WANG, M., LIU, Q., AND WANG, S. **X-net: Brain stroke lesion segmentation based on depthwise separable convolution and long-range dependencies**. In *International Conference on Medical Image Computing and Computer-Assisted Intervention* (2019), Springer, pp. 247–255.

[180] QI, L., ZHANG, H., TAN, W., QI, S., XU, L., YAO, Y., AND QIAN, W. **Cascaded conditional generative adversarial networks with multi-scale attention fusion for automated bi-ventricle segmentation in cardiac mri**. *IEEE Access 7* (2019), 172305–172320.

[181] SANDER, J., DE VOS, B. D., WOLTERINK, J. M., AND IŠGUM, I. **Towards increased trustworthiness of deep learning segmentation methods on cardiac mri**. In *Medical Imaging 2019: Image Processing* (2019), vol. 10949, International Society for Optics and Photonics, p. 1094919.

[182] TAO, Q., YAN, W., WANG, Y., PAIMAN, E. H., SHAMONIN, D. P., GARG, P., PLEIN, S., HUANG, L., XIA, L., SRAMKO, M., AND OTHERS. **Deep learning–based method for fully automatic quantification of left ventricle function from cine mr images: a multivendor, multicenter study**. *Radiology 290*, 1 (2019), 81–88.

[183] VAN ZON, M., VETA, M., AND LI, S. **Automatic cardiac landmark localization by a recurrent neural network**. In *Medical Imaging 2019: Image Processing* (2019), vol. 10949, International Society for Optics and Photonics, p. 1094916.

[184] VESAL, S., RAVIKUMAR, N., AND MAIER, A. **Automated multi-sequence cardiac mri segmentation using supervised domain adaptation**. In *International Workshop on Statistical Atlases and Computational Models of the Heart* (2019), Springer, pp. 300–308.

[185] YE, C., WANG, W., ZHANG, S., AND WANG, K. **Multi-depth fusion network for whole-heart ct image segmentation**. *IEEE Access 7* (2019), 23421–23429.

[186] YUE, Q., LUO, X., YE, Q., XU, L., AND ZHUANG, X. **Cardiac segmentation from lge mri using deep neural network incorporating shape and spatial priors**. In *International Conference on Medical Image Computing and Computer-Assisted Intervention* (2019), Springer, pp. 559–567.

[187] ZHANG, J., DU, J., LIU, H., HOU, X., ZHAO, Y., AND DING, M. **Lu-net: an improved u-net for ventricular segmentation**. *IEEE Access 7* (2019), 92539–92546.

[188] ZHANG, L., WANG, X., YANG, D., SANFORD, T., HARMON, S., TURKBEY, B., ROTH, H., MYRONENKO, A., XU, D., AND XU, Z. **When unseen domain generalization is unnecessary? rethinking data augmentation**. *arXiv preprint arXiv:1906.03347* (2019).

[189] ZHENG, Q. **Deep learning for robust segmentation and explainable analysis of 3d and dynamic cardiac images**. PhD thesis, COMUE Université Côte d'Azur (2015-2019), 2019.

[190] ZHOU, X.-Y., AND YANG, G.-Z. **Normalization in training u-net for 2-d biomedical semantic segmentation**. *IEEE Robotics and Automation Letters 4*, 2 (2019), 1792–1799.

[191] BRAHIM, K., QAYYUM, A., LALANDE, A., BOUCHER, A., SAKLY, A., AND MERIAUDEAU, F. **A 3d deep learning approach based on shape prior for automatic segmentation of myocardial diseases**. In *2020 Tenth International Conference on Image Processing Theory, Tools and Applications (IPTA)* (2020), IEEE, pp. 1–6.

[192] BRAHIM, K., QAYYUM, A., LALANDE, A., BOUCHER, A., SAKLY, A., AND MERIAUDEAU, F. **Efficient 3d deep learning for myocardial diseases segmentation**. In *International Workshop on Statistical Atlases and Computational Models of the Heart* (2020), Springer, pp. 359–368.

[193] CAMARASA, R., FAURE, A., CROZIER, T., BOS, D., AND DE BRUIJNE, M. **Uncertainty-based segmentation of myocardial infarction areas on cardiac mr images**. In *International Workshop on Statistical Atlases and Computational Models of the Heart* (2020), Springer, pp. 385–391.

[194] CHEN, C., BAI, W., DAVIES, R. H., BHUVA, A. N., MANISTY, C. H., AUGUSTO, J. B., MOON, J. C., AUNG, N., LEE, A. M., SANGHVI, M. M., AND OTHERS. **Improving the generalizability of convolutional neural network-based segmentation on cmr images**. *Frontiers in cardiovascular medicine 7* (2020), 105.

[195] CHEN, C., QIN, C., QIU, H., TARRONI, G., DUAN, J., BAI, W., AND RUECKERT, D. **Deep learning for cardiac image segmentation: a review**. *Frontiers in Cardiovascular Medicine 7* (2020), 25.

[196] DOU, Q., CHEN, H., QIN, J., AND HENG, P.-A. **Automatic lesion detection with three-dimensional convolutional neural networks**. In *BioMedical information technology*. Elsevier, 2020, pp. 265–293.

[197] FAHMY, A. S., NEISIUS, U., CHAN, R. H., ROWIN, E. J., MANNING, W. J., MARON, M. S., AND NEZAFAT, R. **Three-dimensional deep convolutional neural networks for automated myocardial scar quantification in hypertrophic cardiomyopathy: a multicenter multivendor study**. *Radiology 294*, 1 (2020), 52–60.

[198] FENG, X., KRAMER, C. M., SALERNO, M., AND MEYER, C. H. **Automatic scar segmentation from de-mri using 2d dilated unet with rotation-based augmentation**. In *International Workshop on Statistical Atlases and Computational Models of the Heart* (2020), Springer, pp. 400–405.

[199] GIRUM, K. B., SKANDARANI, Y., HUSSAIN, R., GRAYELI, A. B., CRÉHANGE, G., AND LALANDE, A. **Automatic myocardial infarction evaluation from delayed-enhancement cardiac mri using deep convolutional networks**. In *International Workshop on Statistical Atlases and Computational Models of the Heart* (2020), Springer, pp. 378–384.

[200] HASAN, M. K., DAHAL, L., SAMARAKOON, P. N., TUSHAR, F. I., AND MARTÍ, R. **Dsnet: Automatic dermoscopic skin lesion segmentation**. *Computers in Biology and Medicine* (2020), 103738.

[201] HUELLEBRAND, M., IVANTSITS, M., ZHANG, H., KOHLMANN, P., KUHNIGK, J.-M., KUEHNE, T., SCHÖNBERG, S., AND HENNEMUTH, A. **Comparison of a hybrid mixture model and a cnn for the segmentation of myocardial pathologies in delayed enhancement mri**. In *International Workshop on Statistical Atlases and Computational Models of the Heart* (2020), Springer, pp. 319–327.

[202] LALANDE, A., CHEN, Z., DECOURSELLE, T., QAYYUM, A., POMMIER, T., LORGIS, L., DE LA ROSA, E., COCHET, A., COTTIN, Y., GINHAC, D., AND OTHERS. **Emidec: a database usable for the automatic evaluation of myocardial infarction from delayed-enhancement cardiac mri**. *Data 5*, 4 (2020), 89.

[203] QAYYUM, A., LALANDE, A., AND MERIAUDEAU, F. **Automatic segmentation of tumors and affected organs in the abdomen using a 3d hybrid model for computed tomography imaging**. *Computers in Biology and Medicine 127* (2020), 104097.

[204] REHMAN, R., YELAMANCHILI, V. S., AND MAKARYUS, A. N. **Cardiac imaging**. *StatPearls [Internet]* (2020).

[205] VESAL, S., MAIER, A., AND RAVIKUMAR, N. **Fully automated 3d cardiac mri localisation and segmentation using deep neural networks**. *Journal of Imaging 6*, 7 (2020), 65.

[206] XIE, W.-Q., ZHANG, X.-P., YANG, X.-M., LIU, Q.-S., TANG, S.-H., AND TU, X.-B. **3d size and shape characterization of natural sand particles using 2d image analysis**. *Engineering Geology* (2020), 105915.

[207] XUE, Y., FARHAT, F. G., BOUKRINA, O., BARRETT, A., BINDER, J. R., ROSHAN, U. W., AND GRAVES, W. W. **A multi-path 2.5 dimensional convolutional neural network system for segmenting stroke lesions in brain mri images**. *NeuroImage: Clinical 25* (2020), 102118.

[208] YANG, S., AND WANG, X. **A hybrid network for automatic myocardial infarction segmentation in delayed enhancement-mri**. In *International Workshop on Statistical Atlases and Computational Models of the Heart* (2020), Springer, pp. 351–358.

[209] ZHANG, Y. **Cascaded convolutional neural network for automatic myocardial infarction segmentation from delayed-enhancement cardiac mri**. In *International Workshop on Statistical Atlases and Computational Models of the Heart* (2020), Springer, pp. 328–333.

[210] ZHOU, Y., ZHANG, K., LUO, X., WANG, S., AND ZHUANG, X. **Anatomy prior based u-net for pathology segmentation with attention**. In *International Workshop on Statistical Atlases and Computational Models of the Heart* (2020), Springer, pp. 392–399.

[211] BRAHIM, K., QAYYUM, A., LALANDE, A., BOUCHER, A., SAKLY, A., AND MERIAUDEAU, F. **A 3d network based shape prior for automatic myocardial disease segmentation in delayed-enhancement mri**. *IRBM* (2021).

[212] BRAHIM, K., QAYYUM, A., LALANDE, A., BOUCHER, A., SAKLY, A., AND MERIAUDEAU, F. **A deep learning approach for the segmentation of myocardial diseases**. In *2020 25th International Conference on Pattern Recognition (ICPR)* (2021), IEEE, pp. 4544–4551.

[213] FARRAG, N. A., LOCHBIHLER, A., WHITE, J. A., AND UKWATTA, E. **Evaluation of fully automated myocardial segmentation techniques in native and contrast-enhanced t1-mapping cardiovascular magnetic resonance images using fully convolutional neural networks**. *Medical Physics 48*, 1 (2021), 215–226.

[214] ISENSEE, F., JAEGER, P. F., KOHL, S. A., PETERSEN, J., AND MAIER-HEIN, K. H. **nnu-net: a self-configuring method for deep learning-based biomedical image segmentation**. *Nature methods 18*, 2 (2021), 203–211.

[215] LALANDE, A., CHEN, Z., POMMIER, T., DECOURSELLE, T., QAYYUM, A., SALOMON, M., GINHAC, D., SKANDARANI, Y., BOUCHER, A., BRAHIM, K.,

AND OTHERS. **Deep learning methods for automatic evaluation of delayed enhancement-mri. the results of the emidec challenge**. *arXiv preprint arXiv:2108.04016* (2021).

[216] MA, J. **Cutting-edge 3d medical image segmentation methods in 2020: Are happy families all alike?** *arXiv preprint arXiv:2101.00232* (2021).

[217] WU, H., LU, X., LEI, B., AND WEN, Z. **Automated left ventricular segmentation from cardiac magnetic resonance images via adversarial learning with multi-stage pose estimation network and co-discriminator**. *Medical Image Analysis 68* (2021), 101891.

[218] VESAL, S., MAIER, A., AND RAVIKUMAR, N. **A multi-stage fully convolutional network for cardiac mri segmentation**.

List of Figures

List of Tables

Document generated with LaTeX and:
the LaTeX style for PhD Thesis created by S. Galland — http://www.multiagent.fr/ThesisStyle
the tex-upmethodology package suite — http://www.arakhne.org/tex-upmethodology/

école doctorale **sciences pour l'ingénieur et microtechniques**

Title: Deep learning architectures for automatic detection of viable myocardiac segments

Keywords: Myocardial segmentation, LGE-MRI, Deep learning, Prior shape, Myocardium, Topological constraints, Pathological tissues.

Abstract:

Accurate myocardial segmentation in LGE-MRI is an important purpose for diagnosis assistance of infarcted patients. Nevertheless, manual delineation of target volumes is time-consuming and depends on intra- and inter-observer variability. This thesis aims at developing efficient deep learning-based methods for automatically segmenting myocardial tissues (healthy myocardium, myocardial infarction, and microvascular obstruction) on LGE-MRI. In this regard, we first proposed a 2.5D SegU-Net model based on a fusion framework (U-Net and SegNet) to learn different feature representations adaptively. Then, we extended to new 3D architectures to benefit from additional depth cues. In a second step, we proposed to segment the anatomical structures using inception residual block and convolutional block attention module and diseased regions using 3D Auto-encoder to perfect myocardial shape. To this end, a prior shape penalty term is added to 3D U-Net architecture. Finally, we proposed first segment the left ventricular cavity and the myocardium based on the no-new-U-Net and second use a priori inclusion and classification networks to maintain the topological constraints of pathological tissues within the pre-segmented myocardium. We have introduced a post-processing decision phase to reduce the uncertainty of the model. The state-of-the-art performance of the proposed methods is validated on the EMIDEC dataset, comprising 100 training images and 50 test images from healthy and infarcted patients. Comprehensive empirical evaluations show that all of our algorithms have promising results.

Titre : Architectures d'apprentissage profond pour la détection automatique de segments myocardiques viables

Mots-clés : Segmentation myocardique, LGE-IRM, Apprentissage profond, Forme antérieure, Myocarde, Contraintes topologiques, Tissus pathologiques.

Résumé :

La segmentation précise du myocarde en LGE-IRM est un objectif important pour l'aide au diagnostic des patients infarctus. Néanmoins, la délimitation manuelle des volumes cibles prend du temps et dépend de la variabilité intra- et inter-observateur. Cette thèse vise à développer des méthodes efficaces basées sur l'apprentissage profond pour segmenter automatiquement les tissus myocardiques (myocarde sain, infarctus du myocarde et obstruction microvasculaire) sur LGE-IRM. À cet égard, nous avons d'abord proposé un modèle 2.5D SegU-Net basé sur un cadre de fusion (U-Net et SegNet) pour apprendre différentes représentations de caractéristiques de manière adaptative. Ensuite, nous avons étendu à de nouvelles architectures 3D pour bénéficier d'indices de profondeur supplémentaires. Dans un deuxième temps, nous avons proposé de segmenter les structures anatomiques à l'aide du module d'attention du bloc résiduel initial et du bloc convolutif et des régions malades à l'aide de l'auto-encodeur 3D pour perfectionner la forme du myocarde. A cet effet, un terme de pénalité de forme préalable est ajouté à l'architecture 3D U-Net. Enfin, nous avons proposé dans un premier temps de segmenter la cavité ventriculaire gauche et le myocarde sur la base du no-new-U-Net et dans un second temps d'utiliser des réseaux d'inclusion et de classification a priori pour maintenir les contraintes topologiques des tissus pathologiques au sein du myocarde pré-segmenté. Nous avons introduit une phase de décision post-traitement pour réduire l'incertitude du modèle. Les performances de pointe des méthodes proposées sont validées sur l'ensemble de données EMIDEC, comprenant 100 images d'entraînement et 50 images de test de patients sains et infarctus. Des évaluations empiriques complètes montrent que tous nos algorithmes ont des résultats prometteurs.

UBFC UNIVERSITÉ BOURGOGNE FRANCHE-COMTÉ

Université Bourgogne Franche-Comté
32, avenue de l'Observatoire
25000 Besançon, France